CHARACTERIZATION OF A CONCEPTUAL MODIFIED SYNTHETIC JET DESIGN IN A CONFINED SPACE

A THESIS SUBMITTED TO
THE GRADUATE SCHOOL OF NATURAL AND APPLIED SCIENCES
OF
MIDDLE EAST TECHNICAL UNIVERSITY

BY

ABDURRAHMAN ATEŞ

IN PARTIAL FULFILLMENT OF THE REQUIREMENTS
FOR
THE DEGREE OF MASTER OF SCIENCE
IN
MECHANICAL ENGINEERING

AUGUST 2022

Approval of the thesis:

CHARACTERIZATION OF A CONCEPTUAL MODIFIED SYNTHETIC JET DESIGN IN A CONFINED SPACE

submitted by **ABDURRAHMAN ATEŞ** in partial fulfillment of the requirements for the degree of **Master of Science in Mechanical Engineering Department, Middle East Technical University** by,

Prof. Dr. Halil Kalıpçılar
Dean, Graduate School of **Natural and Applied Sciences** _____

Prof. Dr. Mehmet Ali Sahir Arıkan
Head of Department, **Mechanical Engineering** _____

Assoc. Prof. Dr. Özgür Bayer
Supervisor, **Mechanical Engineering, METU** _____

Examining Committee Members:

Prof. Dr. İlker Tarı
Mechanical Engineering, METU _____

Assoc. Prof. Dr. Özgür Bayer
Mechanical Engineering, METU _____

Prof. Dr. M. Metin Yavuz
Mechanical Engineering, METU _____

Assoc. Prof. Dr. Özgür Ekici
Mechanical Engineering, Hacettepe University _____

Assist. Prof. Dr. Ali Karakuş
Mechanical Engineering, METU _____

Date:

I hereby declare that all information in this document has been obtained and presented in accordance with academic rules and ethical conduct. I also declare that, as required by these rules and conduct, I have fully cited and referenced all material and results that are not original to this work.

Name, Surname: Abdurrahman Ateş

Signature :

ABSTRACT

CHARACTERIZATION OF A CONCEPTUAL MODIFIED SYNTHETIC JET DESIGN IN A CONFINED SPACE

Ateş, Abdurrahman
M.S., Department of Mechanical Engineering
Supervisor: Assoc. Prof. Dr. Özgür Bayer

August 2022, 95 pages

Cooling relatively small and powerful electronic components is a serious challenge. As the conventional methods to cool electronics became insufficient in terms of size, effectiveness, and cost; the need for smaller, quieter and cheaper systems with high cooling capacity and lower power usage resulted in the development of synthetics jets (zero net mass flux jets) that exempt the cooling system from dependency on an external fluid supply. In this study, a conceptual configuration based on the hybrid synthetic jets is discussed. The motion of the diaphragm in the proposed design is given with a sinusoidal piston movement and the time dependent simulations are conducted with two-dimensional domain. The URANS equation with transient SST k-w turbulence model is selected to solve the governing equations of the fluid dynamics and energy conservation. The effect of the proposed design is investigated in a confined channel, numerically. Up to 15% improvement on the peak local heat transfer flux is found. 26% decrease in the work input by the moving diaphragm is obtained with a 2% loss in the total heat transfer rate. The investigation shows that the suggested design satisfies the thermal requirements with remarkably less work input than the synthetic jets. A parametric study is conducted to observe the effect of different

blowing ratios. Results shows the inferiority of the proposed design under the high blowing ratios compared to the conventional synthetic jets as the impinging effect of the proposed design becomes trivial.

Keywords: Hybrid synthetic jet, impingement, heat and mass transfer, CFD

ÖZ

SINIRLI ALANDA DEĞİŞTİRİLMİŞ SENTETİK JETİN KAVRAMSAL TASARIMININ KARAKTERİZASYONU

Ateş, Abdurrahman
Yüksek Lisans, Makina Mühendisliği Bölümü
Tez Yöneticisi: Doç. Dr. Özgür Bayer

Ağustos 2022, 95 sayfa

Giderek küçülen ve daha güçlenen elektronik parçaları soğutmak ciddi bir zorluk haline gelmiştir. Elektronikleri soğutmak için kullanılan geleneksel yöntemler, boyut, verimlilik ve maliyet açısından yetersiz kaldıkça, yüksek soğutma kapasitesine ve düşük enerji tüketime sahip daha küçük, daha sessiz ve daha ucuz sistemlere ihtiyaç duyulmaya başlanmıştır. Bu durum dışardan sıvı kaynağına ihtiyacı olmayan soğutma sistemi olan sentetik jetlerin (sıfır net kütle akı jetlerin) geliştirilmesine neden oldu. Bu tez çalışmasında hibrit sentetik jetleri temel alan kavramsal bir konfigürasyon tartışılmaktadır. Önerilen tasarımın diyafram hareketi sinüzoidal bir piston hareketi ile verilmiş, simülasyonlar zamana bağlı iki boyutlu domen ile gerçekleştirilmiştir. Transient SST k-w türbülans modeline sahip URANS denklemi, akışkanlar mekaniğinin ve enerjinin korunum denklemlerini çözmek için seçilmiştir. Önerilen tasarımın etkisi dar bir kanalda sayısal olarak incelenmiştir. Bölgesel en yüksek ısı aktarım akısında %15'e kadar iyileşme olduğu gözlenmiştir. Toplam ısı transferinde %2 kayıp ile hareketli diyaframın iş girdisinde %26 azalma elde edilmiştir. Araştırma, önerilen tasarımın, sentetik jetlere göre önemli ölçüde daha az iş girdisi ile termal gereksi-

nimleri karşıladığını göstermektedir. Farklı üfleme oranlarının etkisini gözlemlemek için parametrik bir çalışma yapılmıştır. Sonuçlar, önerilen tasarımın, yüksek üfleme oranları altında, konveksyonel sentetik jetlere göre yetersiz olduğunu göstermektedir çünkü bu durumlarda önerilen tasarımın çarpma etkisi gözlenmemiştir.

Anahtar Kelimeler: Hibrit sentetik jet, çarpma, ısı ve kütle transferi, HAD

To my family and my friends

ACKNOWLEDGMENTS

I would like to thank Assoc. Prof. Dr. Özgür Bayer for his continuous support. I would like to express my gratitude to my friends from Dr. Bayer's Research Group for their support, assistance, and friendship. I am indebted to my friends İpek Ercan, Onat Aşık, Mehmet Koçak, Seyedmohsen Baghaei Oskouei, and Firdevs Ersoy for their most needed mental support throughout this journey. I would like to show my most significant appreciation towards my family for their constant support throughout my academic life.

TABLE OF CONTENTS

APPENDICES

LIST OF TABLES

TABLES

LIST OF FIGURES

FIGURES

LIST OF SYMBOLS

Greeks

γ	Intermittency
μ	Dynamic viscosity
ρ	Density
Γ	Strength of the vortex
ε	Ratio of the orifice exit radius of curvature to the orifice width
κ	Ratio of the vortex core radius to distance between the two vortexes
ω	Specific dissipation rate
ϕ	Phase angle in rad/s

Roman

A	Diaphragm displacement
D	Width of the channel
f	Actuation frequency in Hz
h	Height
d	Width
k	Thermal conductivity, turbulent kinetic energy
L	Non-dimensional Stroke length
Nu	Nusselt number
Re	Reynolds number
S	Stokes number
t	Time
T	Time period
x	Transverse direction
y	Axial direction
H	Height of the channel
Sr	Strouhal number
v	Axial velocity
u	Transverse velocity
c	Ratio of the amplitudes of the spatial-averaged and centerline velocities
p	Constant for the effect of exit curvature on the flow separation
K	Jet formation constant
w	Actuation frequency in rad/s
dt	Time step
Co	Courant number
U	Cross flow velocity
s	Displacement

Subscripts

cl Centerline

c Cavity

avg Average

t Turbulence

x Transverse direction

y Axial direction

∞ Free stream

h Heater

Superscripts

$*$ Dimensionless

Overs

$\dot{X}$ Rate of change of a variable in time domain

X' Variable per unit depth

$\overline{X}$ Averaged variable in time domain

X'' Flux of variable

Operators

dX Derivative of X

∂X Partial derivative of X

DX Material derivative of X

∇X Gradient of X

$\nabla \cdot X$ Divergance of X

$\nabla \times X$ Curl of X

Abbrevations

3D Three-dimensional

2D Two-dimensional

CJs Continuous Jets

SJs Synthetic Jets

ZNMF Zero Net Mass Flux

AVBP Active Valve-Based Piezoelectric

VLP Valveless Piezoelectric

HSJs Hybrid Synthetic Jets

MEMS Micro Electronic Mechanical Systems

URANS Unsteady Reynolds-Averaged Navier-Stokes

SST Shear Stress Transport

UDF User Defined Function

PISO Pressure Implicit with Splitting of Operators

PZT Piezoelectric Transducer

BM Base Model

MBM Modified Base Model

PM Porposed Model

SIMPLE Semi-Implicit Method for Pressure Linked Equations

SIMPLEC Semi-Implicit Method for Pressure Linked Equations - Consistent

CHAPTER 1

INTRODUCTION

The global need for fast and powerful electronic devices has fomented the trouble of removing the excess heat from the systems. One of the leading causes of failure in most applications that utilize electronics with high power consumption is thermal-related [1]. The prior electronics were larger, and in most occasions, a simple heat sink was sufficient to prevent them from overheating. In contrast, even simple household goods nowadays require complex and compact designs. Therefore, the heat removal process has been a trendy topic for engineers. The most conventional methods, extended surfaces, passive coolers, etc., have been thoroughly studied and nearly reached their limits with the current production techniques.

Further needs pushed the researchers to utilize a combination of the active cooling techniques; jet flows, multi-phase flows, multi-layer channel flow, etc., with the passive cooling techniques, heat sink design, and optimization, or promoting the turbulence on the flow. Active methods involve an external device or actuator to drive fluid and reduce the thermal resistance by changing the characteristic of the boundary layer. Passive enhancement methods require no external power, i.e., the techniques usually rely on the improvements to the existing heat sink design. Some passive enhancement techniques implement turbulence promoters, optimize the heat sink design, or benefit from the multi-phase coolant characteristics. However, these enhancements usually demand high initial costs and result in a considerable increase in pressure drops. Furthermore, the passive enhancements could face trouble dealing with local hot zones and adapting to the changing thermal needs. In comparison, active techniques accommodate both challenges while coping with modern demands in thermal engineering. However, these methods rely on high energy consumption and regular maintenance;

moreover, dependency on forced convection requires big and bulky fans which takes a lot of space.

The incapability of cooling the high heat flux electronics has become a bottleneck in Micro-electromechanical systems. Developments in the last decade call for a heat flux rate up to $1kW/cm^2$ [2]. Moore's law states that the number of transistors will double itself in almost two years. As the density increases, unstable and non-uniform temperature profiles and local temperature jumps will create particular challenges [3].

This chapter covers the evolution of jet flows and development of the hybrid synthetic jet concept and gives background information about implementation of the jet flows in heat transfer applications. The first section explains the continuous jets (CJs), basis for both synthetic jets and the hybrid jets. The second section describes the integration of the micro scaled actuators which resulted in the development of micro-scale active coolers, the synthetic jets (SJs). The following section outlines the micro pumps since the advancements in the piezoelectric micro pumps lead to more effective designs of the SJs, the hybrid synthetic jets. The last section illustrates the hybrid synthetic jets with a brief literature review.

1.1 Continuous Impinging Jets

Jet cooling is considered as one of the most effective heat transfer enhancement method. Unlike the other cooling methods such as using extended surfaces and conventional forced convection approaches, the cooling effect is local. The primary enhancement is due to the flow stagnation phenomena [4]. The efficiency of impinging heat transfer is further increased by manipulating the geometric and operational parameters. In the literature some parameters are modified for jets to suit different applications. This section summarizes the working principal and the advances in the continuous jets.

A jet flow occurs when a fluid momentum goes through an orifice (or a nozzle). Figure 1.1 shows a typical impinging jet flow, and its flow regions. The diameter of the

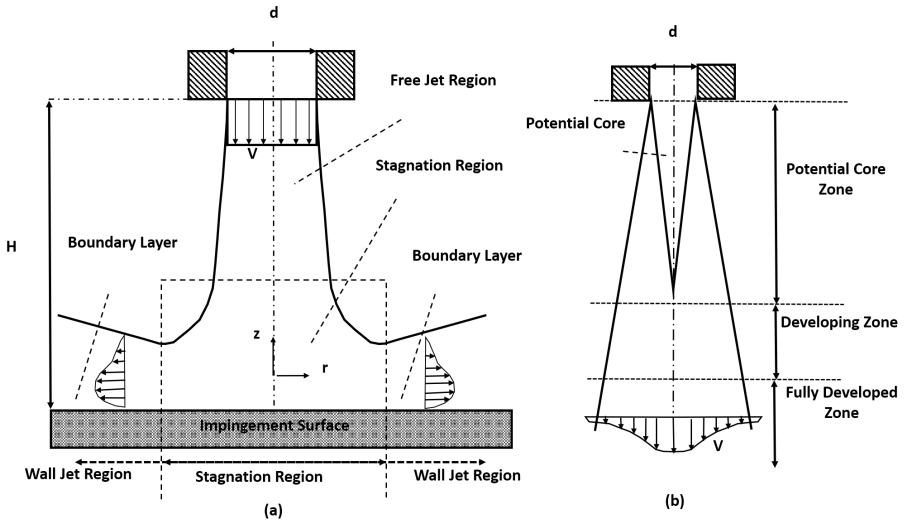

Figure 1.1: Illustration of the flow regimes and the zones for a jet impinging on a flat surface, adapted from [7]

orifice is labeled as d and the distance between the orifice and the impingement surface as H. A comprehensive investigation on the formation and the applications of the jet flow is available in the literature. The key elements influencing the performance of CJs are shearing, turbulence and stagnation effect. The fluid leaving the orifice experiences shearing with the surrounding ambient fluid. The shearing changes the temperature as the turbulent kinetic energy changes, expanding the free jet region. The velocity profile stays almost the same in the potential core region, of which its length is almost six to seven times the diameter of the orifice [5]. The shearing effect dominates the jet around the developing zone, where velocity starts to diminish rapidly. This phenomenon eventuates in turbulence. Afterward, the flow reaches the stagnation region. In that region, the secondary jet, i.e., the wall jet, develops, and stagnation occurs. Stagnation is a critical phenomenon for local cooling due to the impinging behavior that disturbs the thermal boundary layer. Another unique feature of the impinging jets is the counter-rotating vortex pair, created after the wall jets turn around, as shown in Figure 1.2. Furthermore, the vortex rings help the incoming potential core by feeding it. Several parameters affecting the heat transfer rate in CJs are; Reynolds number (Re), Prandtl number, and the nondimensional geometric parameters, such as the nondimensional orifice to plate spacing (H/d), the nondimensional distance from the stagnation point and the orifice geometry [6].

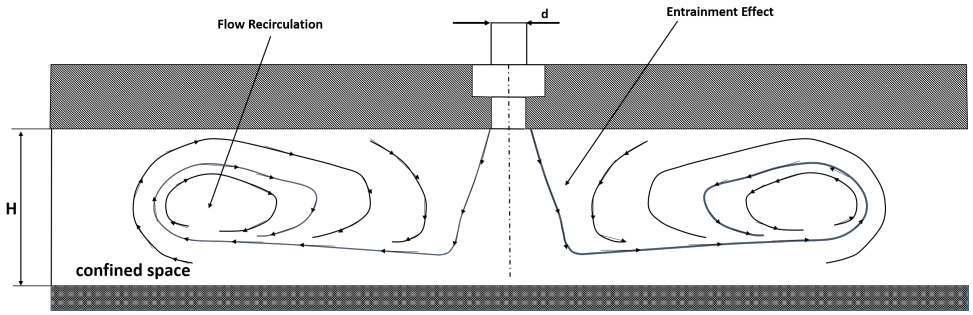

Figure 1.2: Visualization of the flow recirculation of a single impinging jet in confined space, adapted from [8]

1.1.1 The Effect of Various Parameters on Impinging Jets

Effects of the aforementioned parameters are investigated with experimental and numerical methods. Lytle and Webb [4] set an experiment to find the relation of several parameters with the Nusselt number (Nu). It was reported that the nondimensional distance (H/d) is linearly dependent on the square root of the Re. The local Nu variation with respect to the H/d was found linearly dependent on $(H/d)^{-0.288}$ having a peak in the stagnation point. Furthermore, distinct local maximums of the Nu were found to exist due to the increase in the turbulence related to the flow acceleration in the radial direction (r direction in the Figure 1.1). Goldstein and Behbahani [9] showed that in small H/d values, the peak heat transfer rate increases, whereas, in relatively larger distances, the heat transfer rate reduces. In the presence of a cross flow, which is a flow in perpendicular direction, the peak heat transfer rate shifts toward the cross flow direction.

A parametric experimental study was conducted by Sparrow et al. [10] to observe the effect of the jet-to-cross flow blowing ratio on the nondimensional distance between the orifice and the stagnation point. The H/d value varied between 3-12, whereas the blowing ratio varied between 4-12. The optimum value in terms of the heat transfer on the stagnation was found to be about 5 for H/d, for higher blowing ratios.

The effect of the contouring was studied by Colucci and Viskanta [11]. The results showed that contouring is only effective when H/d is lower than 1. The effect was limited to a change in the location of the secondary local maxima of the Nu. It was found that the effect depends on the Re, and the orifice geometry. The contouring

is done by increasing the orifice size in the flow direction, as shown in the Figure 1.3. Furthermore, Brignoni and Garimella [12] introduced contouring in the opposite direction (similar to a converging nozzle) and stated an increase in the ratio of average heat transfer coefficient to the pressure-drop obtained using the narrow design with respect to other designs, given in the Figure 1.4.

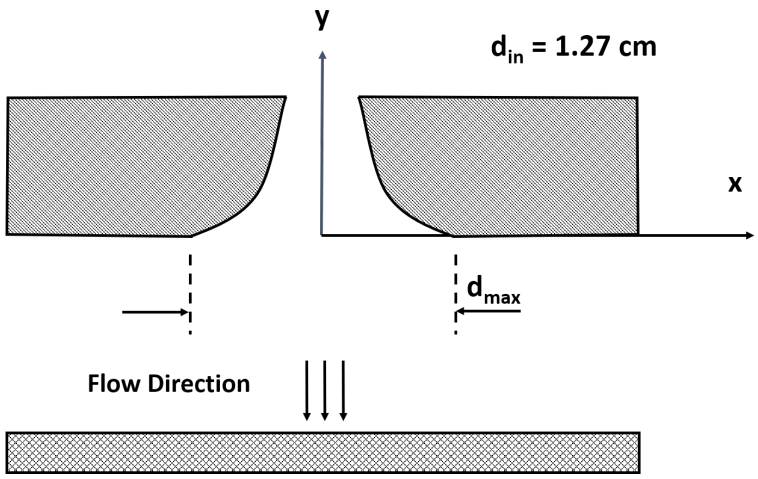

Figure 1.3: Representation of diverging contouring of the nozzle, adapted from [11]

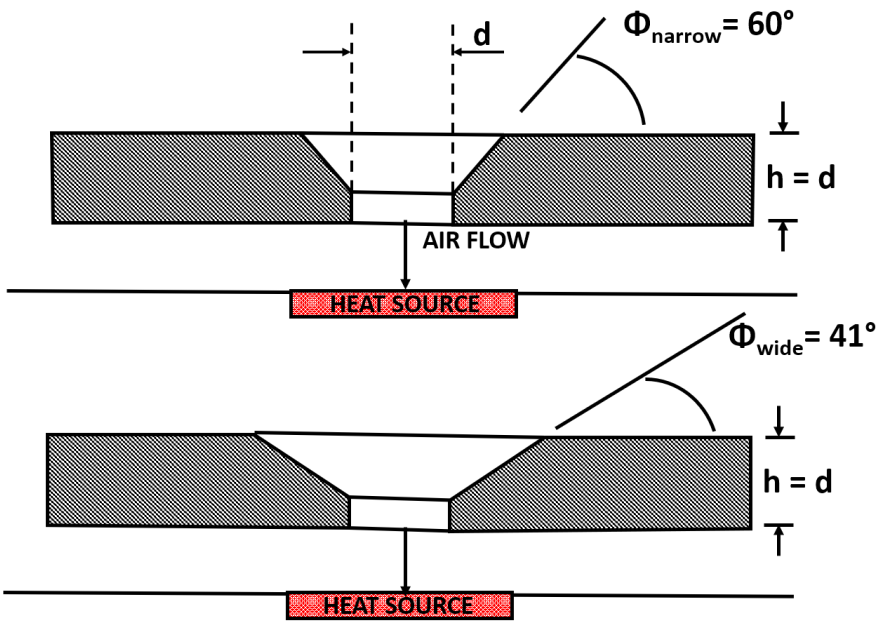

Figure 1.4: Representation of the nozzle inlet chamfering, adapted from [12]

The parametric study involving the variation of orifice aspect ratio between 0.25 to 12 were conducted by Garimella and Nenaydykh [13]. Re and H/d were also manip-

ulated to observe their role. The orifice aspect ratio was reported to be optimal when lower than 1 for all the cases.

The impinging jet flow can be formed with various actuators, such as the piezoelectric mechanism. Piezoelectric actuators are commonly used in micro-scaled applications. The following section discuses the piezoelectric driven synthetic jets.

1.2 Synthetic Jets

Synthetic Jets (SJs) enhance heat transfer with similar features to the conventional continuous impinging jets [14, 15]. Furthermore, as stated by Greco et al. [16], high Re and low Strouhal number (Sr) make them even more similar. Re and Sr are defined in section 2.2.

Some of the distinct features of the synthetic jets are

• a cyclic behavior,

• applicability in small-sized devices,

• and operating without the bulky flow actuators, such as fans.

Actuator of SJ is a Helmholtz resonator [17] with three fundamental components: a cavity, a diaphragm, and an orifice. The cavity is a bounded space with only one opening: the orifice. A voltage-driven piezoelectric actuator controls the size of the cavity. The piezoelectric membrane, i.e., the diaphragm, moves in a cyclic motion allowing the cavity to shrink its size during ejection while enlarging it in the suction phase.

Orderly vortex rings are created in each cycle, imparting momentum in the flow direction without net mass flux. The rings create radial instabilities and ultimately cause a transition to turbulent flow [18].

The applications of the SJs vary from active flow controllers to heat and mass transfer devices [19, 20, 21, 22].

Figure 1.5 depicts the generic representation of a typical synthetic jet with dimen-

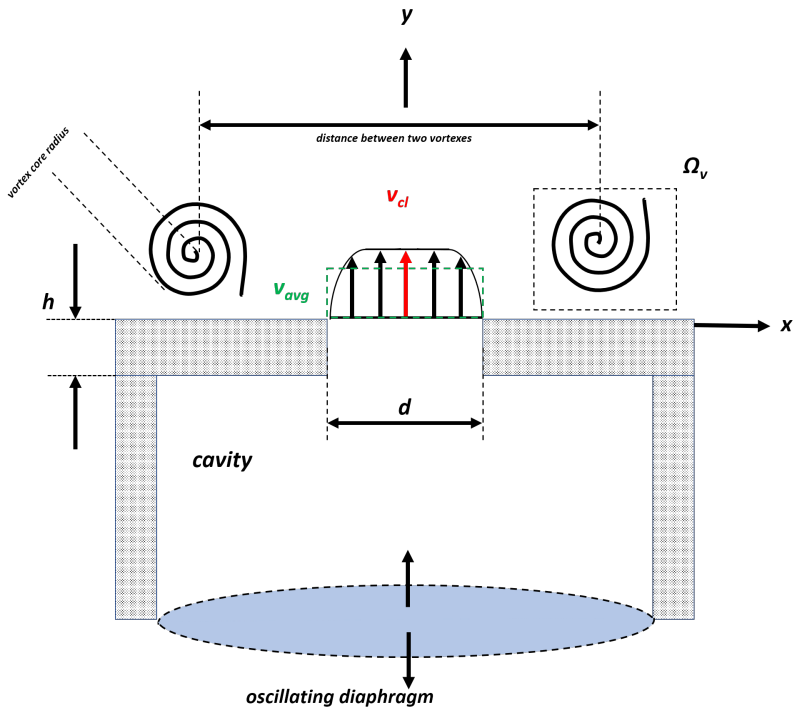

Figure 1.5: The visual representation of a typical synthetic jet

sional labels which are consistent across the study. Many parameters have been shown to affect the performance of the SJs which are explained in the following subsection.

1.2.1 The Effect of Various Parameters on Synthetic Jet

This section introduces the thermal enhancement due to SJs and some of the parameters that affect their cooling performance and flow characteristics. The distance between the heated surface and the orifice, Re which is based on the time-averaged centerline velocity and the orifice width, dimensionless stroke length which represents the ratio of the length of the liquid particle pushed out of the orifice during the ejection phase (l) to the orifice width (d), excitation frequency (f), Stokes number (S) the ratio of the response time of the particle to the flow-field time scale and geometrical parameters are the main investigated parameters in the literature.

Re controls many characteristics of the vortex rings but does not affect their formation and advection [23]. Re determines if the SJ would be laminar, transitional, or turbulent [15]. The circulation (Γ), i.e., the strength of the vortex, is governed by Re

and Sr [24]. Silva-Llanca et al. [25] related the enhancement of the Nu to the strength of the vortex. Gillespie et al. [26] stated that the maximum Re results in maximum cooling performance depending on the Stokes number.

The size of the orifice has more effect on the flow field than the cavity size, according to a numerical study by Jain et al. [27]. In contrast to the finding by Jain et al., Feero et al. [28] experimentally showed the effect of the cavity size on the performance of the SJ is not negligible.

In their research, Kercher et al. [29] discovered that the SJs are ideal for hot spot cooling, providing the optimum cooling results for a surface-orifice spacing ratio (H/d) with a value between 6.3 and 8.4. Greco et al. [30, 31] agreed with Kercher et al. [29] by performing a Stokes number based study and showed that the maximum heat transfer from a heated surface via SJ impingement takes place of $H/d = 6$. Gillespie et al. [26] explained why the optimum space exists; SJ creates hypothetically three regions; near, intermediate, and far field. The optimum value was found in the intermediate field since the near field does not allow the mixing of colder ambient fluid, and the far field is under the effect of the highest momentum diffusion.

Strouhal number, depending on Re and S, is an important criterion of jet formation and described in the 1.2.2.

1.2.2 Jet Formation Criterion for Synthetic Jets

The criteria for two-dimensional jet formation are directly related to vortex formation. The suction phase should not ingest the vortex created during the expulsion period of the cycle; otherwise, jet does not form. Previous studies from Smith and Swift [32] and Rampunggoon [33] suggested a criterion for the formation of jet, individually. Smith and Swift points out that the threshold stroke length is an essential parameter for jet formation, whereas, Rampunggoon et al. stated the Re/S ratio defines whether a jet would form with an order of magnitude analysis. The criterion is related to geometric parameters, such as the orifice diameter (or slot width), the orifice height, and the radius of curvature of the orifice edge and operational parameters such as the oscillation frequency, resonance frequency, and displacement of the diaphragm. The

compressibility factor of working fluid is an important parameter while determining the criterion, which is labeled as κ. Buckingham–Pi theorem reduces the parameters that need to be controlled. The criterion finally becomes;

$$\frac{1}{Sr} = \frac{Re}{S^2} > \frac{32c^2(1+\varepsilon)^p}{\kappa\pi^2} = K \tag{1.1}$$

where, Sr is the Strouhal number, c is the ratio of the amplitude of the spatial-averaged velocity U_{avg} to the maximum centerline velocity U_{cl}, p takes accounts for the effect of exit curvature on the flow separation, ε is equal to the ratio of the orifice exit radius of curvature to the orifice radius and κ is related to the ratio of the vortex core radius to distance between the two vortexes. The jet formation constant is defined as K. Holman R. et al. [34] states that K is roughly 0.16 and 1 for axisymmetric and two-dimensional SJs, respectively.

1.3 Pros and Cons of the Synthetic Jets

Comparative researches are conducted to observe the SJs' inferiority and superiority to CJs. Arik et al. [35] stated that SJs are more effective in terms of heat transfer than CJs in similar conditions due to the inherent features of SJs such as vortex dipoles which increase the mixing and the turbulence intensity. Whereas He et al. [36] showed the limitation of this superiority in specific applications. When the orifice wall distance is relatively smaller, CJ outperforms the SJ since the jet flow would not develop. Bhapkar et al. [37], suggested to manipulate the cavity shape to overcome the deficiency in the near-field. It is shown that proper cavity shape could reduce the confinement effect by allowing the hot air escape without entering the cavity, as shown in the Figure 1.6.

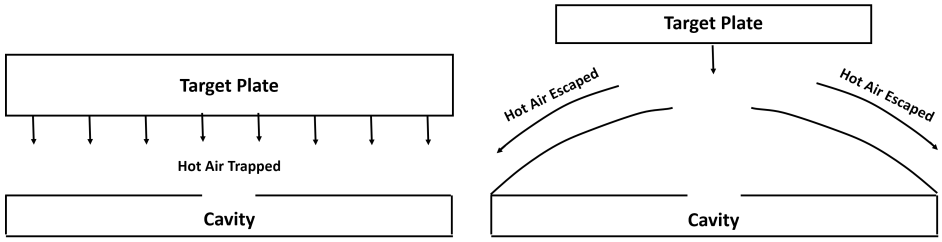

Figure 1.6: Schematic of the flow of air along the conventional and proposed cavity, adapted from [37]

1.4 Piezoelectric Pumps

Piezoelectric pumps are essentially micro pumps with piezoelectric actuators. Piezoelectric pumps have been significant in microfluid transfer applications that need high accuracy. This section explains the piezoelectric pumps in three main sections. Firstly, the configuration of the piezoelectric pumps is categorized in two aspects: valveless and valve-based designs. Secondly, some application examples are given. Lastly, the advantages and disadvantages of piezoelectric pumps are listed.

Munas et al. [38] offered a valveless piezoelectric (VLP) design with a resistance difference method. The method involves creating resistances in order to have a unidirectional flow throughout the system without any physical valves. During the pumping stroke, the cavity behaves like a conventional synthetic jet as the fluid is directly expelled out through the outlet since inlets are perpendicular to the outlet. In contrast, during the suction stroke, due to forward momentum and fluid resistance at the inlets and outlets, most of the fluid goes thorough the inlet rather than the outlet. Figure 1.7 explains the related parts and working principle [38].

Valve-based piezoelectric pumps utilize one-way valves in opposite directions which are placed at the inlet and the outlets to achieve the unidirectional flow by continuously closing and opening the valves. The valves could allow the fluid to pass in one direction with passive and active designs. Feng et al. [39] showed a passive approach to create such flows. The authors utilized parylene valves, as shown in the Figure 1.8. The parylene valves take advantage of their shape and allow the fluid to go through them while they deform. He et al. [40] utilized a passive umbrella valve,

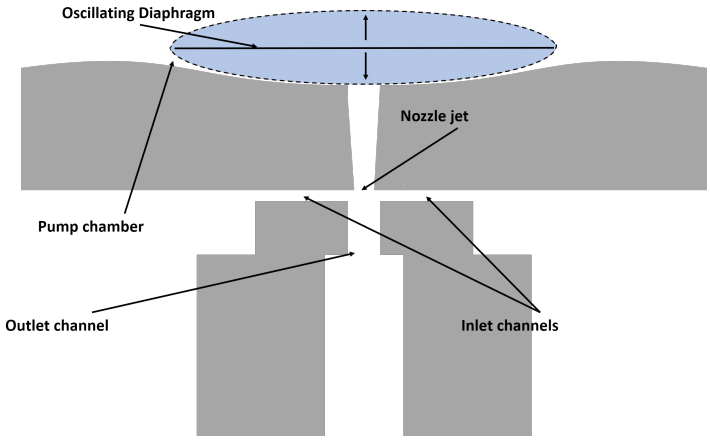

(a) A typical valveless micropump, adapted from [38]

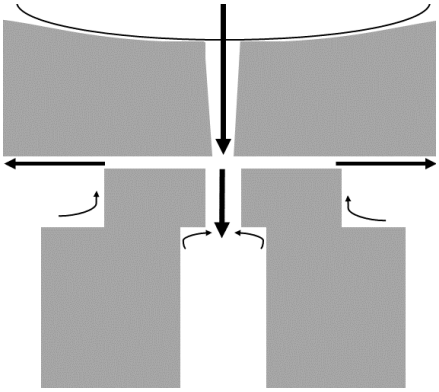

(b) The direction of fluid during compression

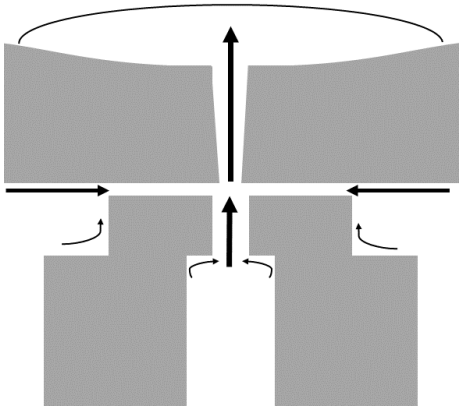

(c) The direction of fluid during suction

Figure 1.7: The working principle of the VLP: the flow directions, adapted from [38]

and proposed a novel idea for measuring the flow rate by the sound pressure level. The passive valves control the fluid flow direction with the help of pressure gradients. Therefore, passive-valve-based designs do not require any extra controllers.

Various type of passive valves, i.e. ball, cantilever, bridge valves etc., have been studied in the literature [41, 42, 43, 44, 45, 46, 47]. Results show that ball and cantilever valves are prone to leakage and fatigue. Umbrella valves proved to be more durable, whereas the design creates more phase lag as the frequencies increases [46].

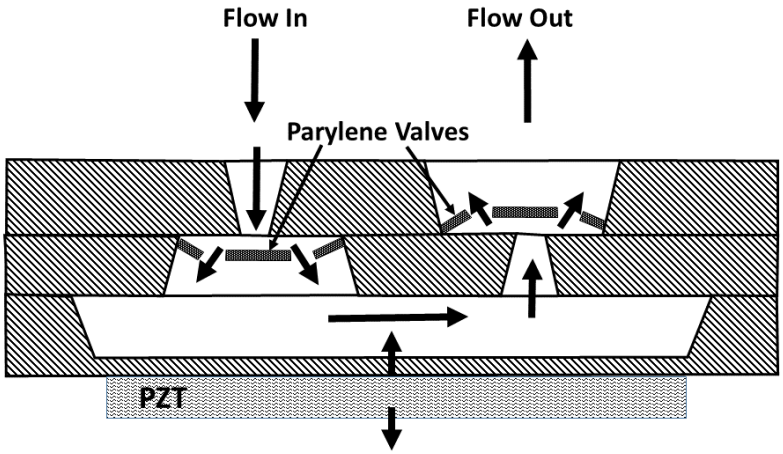

(a) A parylene valve design as a passive-valve-based piezoelectric pump

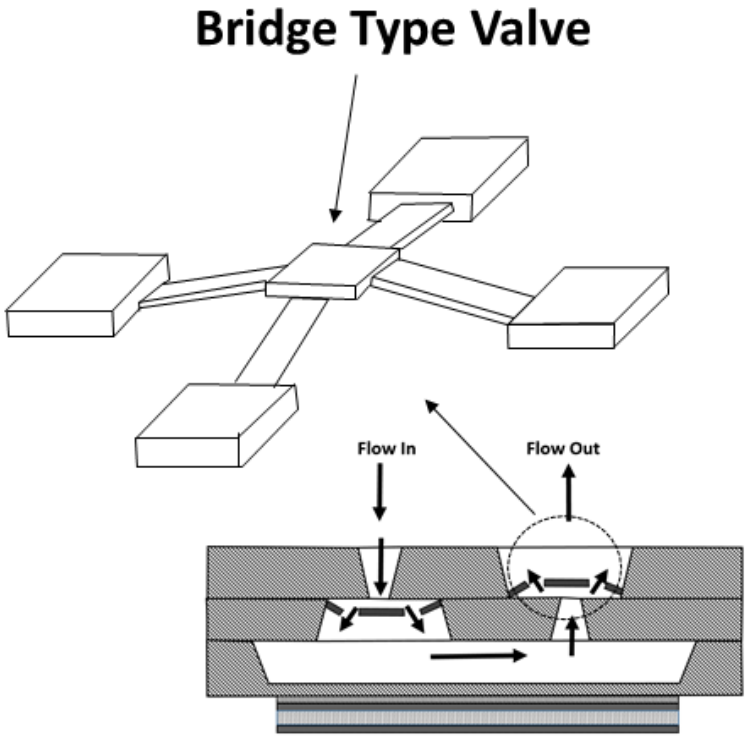

(b) Detailed visualization of the bridge type valve

Figure 1.8: Schematic for the bridge type parylene valves and the visualization of the fluid directions, adapted from [39].

On the contrary, active-valve-based piezoelectric (AVBP) designs require additional components to control the state of the valves. The most common control method is the piezoelectric vibrators [48]. Lee et al. [49] designed AVBP that could go up to

the pressure and flowrate values of $8.3MPa$ and $204mL/min$ at $1000Hz$; Lemke et al. [50] designed an AVBP with the pressure and flowrate values of $50.5kPa$ and $4.36mL/min$ at $45V$. The results show that the AVBPs perform better than the passive-valve-based piezoelectric pumps. The main advantage of the VLPs is their durability against fatigue and wear at high frequencies while their disadvantage is the performance limitation due to the liquid backflow and low volumetric efficiency which is the ratio of the net output fluid volume ejected from the orifice during the ejection phase to the total fluid volume exchanged through the same orifice over the whole period.

1.5 Hybrid Synthetic Jets

The principal drawback of the impingement SJ is the recirculation of the heated air in confined spaces, especially when the nozzle-to-surface spacing is small. The hybrid SJ integrates fluidic diodes into a conventional synthetic jet, and offers a potential solution. With fresh air from the cold surroundings, the jet flow enters the heat exchange zone with lower temperatures and similar characteristics to the synthetic jets. The net output fluid volume ejected from the orifice during the ejection phase stays the same; in contrast, the total exchanged fluid volume through the same orifice over the whole period changes. Their ratio, volumetric efficiency, describes the rectification performance of the actuators of hybrid SJs [51]. Trávníček et al. [52] developed a hybrid synthetic jet actuator with a pair of fluidic diodes that showed a volumetric efficiency of 13%. The efficiency further improved by 19% [53] and 70% by Kordík and Trávníček [54]. In another study, Trávníček et al. [55] reported 26% larger flow rate than Trávńiček et al.[52], leading 18% increase in the heat transfer rate compared to conventional SJ. Hsu et al. [53] experimentally showed that a double-acting hybrid synthetic jet offers enhanced vorticity magnitude compared to the synthetic jets. Following studies achieved volumetric efficiencies up to 79% [56]. The volumetric efficiency of impingement hybrid synthetic jets theoretically can be up to 100% like classical reciprocating pumps [57].

Qinghua, et al.[57] performed a parametric numerical study to compare the effect of the orifice geometry, and showed the D2 case in Figure 1.9 is the optimum in

terms of Nu and temperature of the heater under constant heat flux. The geometry was designed to take advantage of the forward momentum to deny the incoming flow from the confined space without affecting the potential core which exits during the ejection. Nu is enhanced by 54.7% comparing to the conventional SJ and the heated wall temperature dropped from 95.7 °C to 70.8 °C.

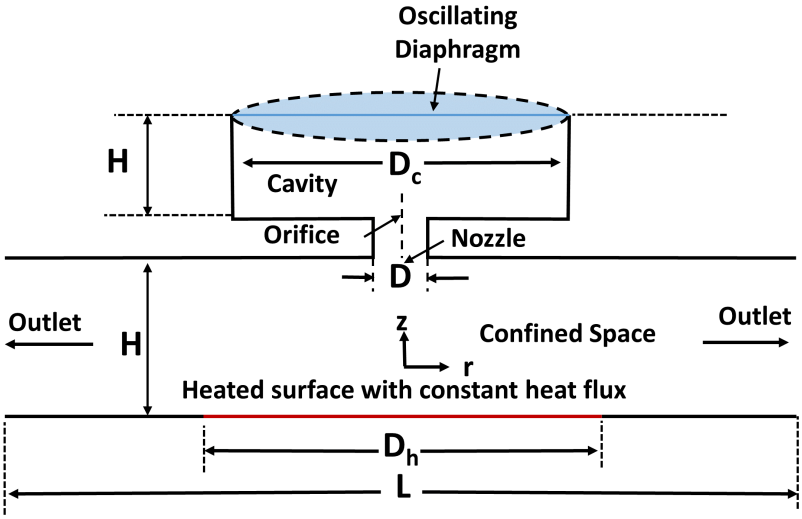

(a) An impingement synthetic jet actuator in a confined space

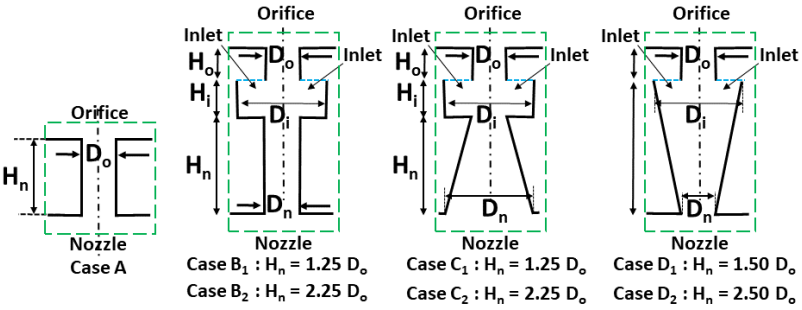

(b) Various cases of nozzle geometry design for hybrid synthetic jet actuators with fluid diodes

Figure 1.9: Schematic of (a) a confined space synthetic jet with a heater surface and (b) multiple cases of orifice geometry in hybrid synthetic jet with fluid diodes, adapted from [57].

1.6 Motivation and Scope of the Thesis

In this study, a modified hybrid synthetic jet design is proposed. The design could be integrated in multi-layered microchannel heat sinks, to observe the improvement with respect to the conventional designs such as single layered, double layered and SJ integrated microchannels.

The unsteady turbulent flow is solved with a commercial solver, ANSYS Fluent, which utilizes the finite volume method for the domain discretization. Reynolds-averaged Navier–Stokes equations (RANS equations) with Transient SST $k-\omega$ model is selected to account for the turbulence terms.

The objective of this study is to compare the effect of the proposed design in given applications with the former designs of synthetic jets, and to provide prior work for it's integration in the complex heat sink designs. The proposed design aims to prevent recirculation of the fluid and reduce the power consumption with the help of flow direction controllers.

This thesis is organized as follows. In Chapter 2, the methodology is presented. Mathematical descriptions of the governing equations with the assumptions are explained. The verification and the case study results are given in Chapter 3. In Chapter 4, the conclusion and future works are presented.

CHAPTER 2

METHODOLOGY

The conservation equations are used to characterize the flow in the domain. These equations include the continuity, momentum and energy transport equations. The equations are simplified based on the physics of the problems and discretized by Finite Volume Method with a commercial software.

2.1 Generic Numerical Domain: Boundary Conditions & Basic Parameters

The literature includes investigations in 2D planar and 2D axisymmetric domains for SJs. In the presence of a cross flow, Jagannatha et al. [58] state that 2D planar is suitable. Therefore, the numerical domain for the base model (BM) presented in this study is selected as a typical SJ studied by Jagannatha et al. [58] in a 2D planar assumption. The domain consists of orifice width of $d = 1$ mm, moving wall amplitude of $A = 1$ mm, frequency $f = 500$ Hz, confined space width $D = 27d$, heater width $L_h = 9d$, height of the confined space $H = 10d$, cavity width $d_c = 9d$, the aspect ratio of the cavity $d_c/h_c = 1.5$ and orifice height $h = 1$ mm as depicted in Figure 2.1. The model is constructed with a commercial Computational Fluid Dynamics (CFD) solver, FLUENT, in two dimensions. A structured mesh is generated by ANSYS Meshing. Elements near the walls are refined so that the y+ and y* values are close to one. Refinements with the standard methods such as adding bias or inflation near the moving wall resulted in impairment within the mesh. This is related to the moving mesh simulations of the diaphragm movement. Therefore, more comprehensive refinement is done manually instead of using the aforementioned methods. The regions near the walls are split, and individual mesh sizing is utilized. After manipulating

the first element height near the walls so that the y+ and y* are near one, at least ten layers of mesh were used with that height as suggested by the Fluent User Manual. The utilized mesh for the verification study is given in Figure 2.2.

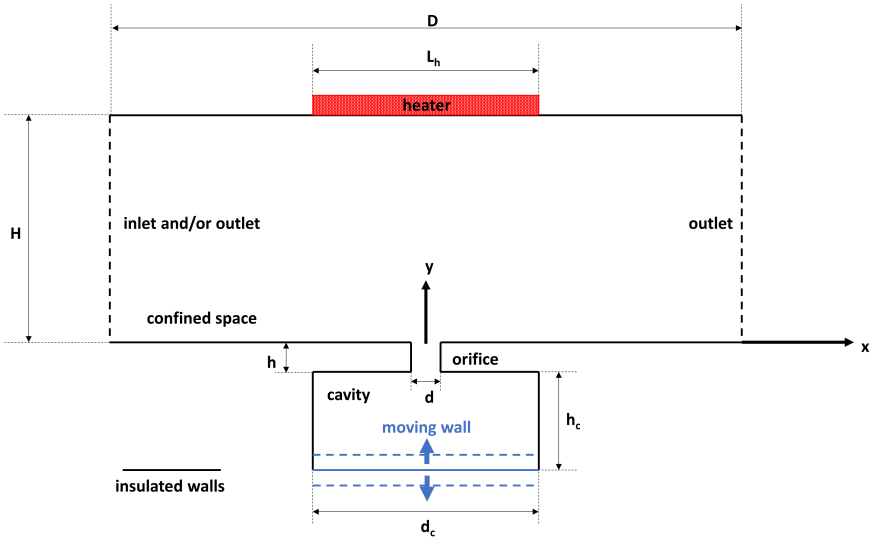

Figure 2.1: The schematic of the Base Model

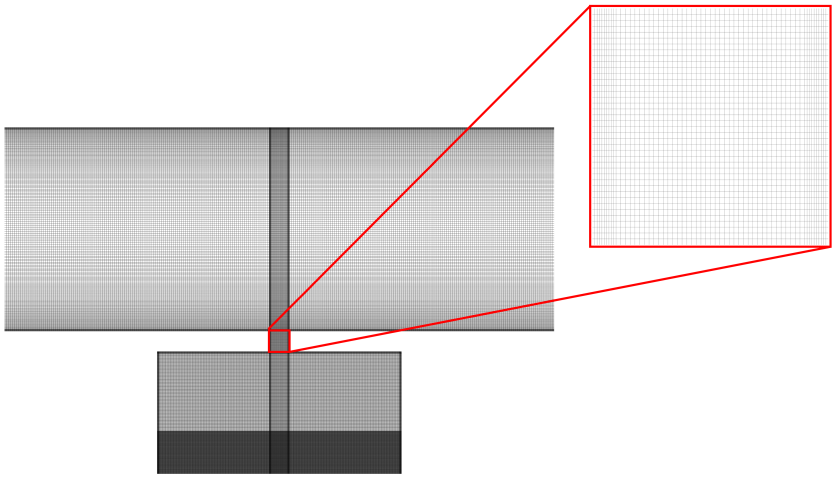

Figure 2.2: Meshing of the base model

The numerical domain for the base model presented in this study is verified with the benchmark study by Jagannatha et al. [58] and results are given in section 3.1. The assumptions are based on the flow characteristics. The incompressible model is selected, since the flow does not go under shock. Furthermore, the compressiblity effects are observed to be negligible as they are compared with a study that assumed the

air as ideal gas. The properties of the working fluid is taken as constant since the temperature does not change drastically. The viscous heating is assumed to be negligible due to the low viscosity of air and the low Mach number of the flow. The turbulence intensity is the ratio of the square root of the mean average of the fluctuating velocity components to the Reynolds averaged mean velocity. It is taken as 3% at the pressure inlet and the outlets, since the geometry is in small-length scale. Even though, in the literature, it is proven that the motion of the piezoelectric diaphragm can be modeled more realistically with a logarithmic function, the logarithmic function comes with several challenges when modeling. The logarithmic function allows the meshes on it to move with different velocity but requires complex triangular meshes in the adjacent zone. During the motion, the meshes deform non-uniformly; therefore, remeshing and smoothing should be utilized to avoid large skewness and negative volumes. Furthermore, the nonorthogonality between the meshes results in much longer computational time. Therefore, it is assumed that the diaphragm is driven by the rigid piston motion with a sinusoidal position function instead. Lastly, radiation is neglected since the domain does not have major temperature gradients.

The transient pressure-based solver is selected. The implicit time discretization is applied for time marching, second-order discritization scheme is used for the momentum, pressure, turbulence kinetic energy, specific dissipation rate and energy in the segregated solution method. The Pressure Implicit with Splitting of Operators (PISO) scheme is used for the coupling of pressure and velocity as suggested by Jagannatha et al. [58]. The thermal boundary conditions for the cavity and the confined space walls, except the heater, are adiabatic. The heater is kept at a constant temperature of 360 K. The confined space openings are considered as pressure outlets. The back flow is allowed with a temperature of 300 K to simulate the unrestricted surrounding air. The boundary condition for walls, as well as the diaphragm, are treated as no-slip. The motion of the diaphragm is controlled by the user defined function (UDF), given in the appendix A. The motion is described as a sinusoidal piston-cylinder movement with a position function, $y = Asin(wt + \phi)$, to have a compliance with the work of Jagannatha et al. [58]. The UDF is constructed with a macro defined in FLUENT software. The macro, DEFINE_CG_MOTION, updates the velocity of the cells of the moving wall at each time step. The dynamic meshing

is utilized to simulate the motion of the moving mesh, the selected dynamic meshing technique is layering. This technique splits or merges meshes depending on predefined criteria. Height based layering with 0.1 split and collapse factors is selected as the criteria to ensure that the y+ values does not exceed the required value of one. Split and collapse factors determine when to split or merge the moving boundary meshes, respectively. If the moving boundary mesh height increases more than 10%, the mesh is split in two, whereas, if the mesh shrinks to its one tenth, the layering technique merges the mesh with the neighbor mesh in the direction of the motion. The solution is initialized with zero velocity and gage pressure, and uniform 300K temperature in the fluid domain. Each cycle is discretized in 1080 time step where maximum 100 iterations are allowed for each. The criteria that are set to limit the number of iterations are the residuals. The iterations are carried out until either the continuity, x-velocity, y-velocity, k, w, γ and $\widetilde{Re_{\theta t}}$ residuals are below 10^{-3}, and energy residual is below 10^{-6} or 100 iterations are carried out. The discretization performs properly with the given mesh and operation conditions since the convergence is met in seven iteration at most. Solution data is saved for each 30 time steps per cycle to have adequate number of results to represents the flow characteristics. Even though the temperature periodic state is reached after about 20 cycles, the velocity and the pressure contours showed negligible variation after a couple of cycles. It is worth noting that similar conditions to BM are chosen for the other designs.

2.2 Data Reduction

In this section, aforementioned parameters defining the characteristics of the synthetic jets are listed. Furthermore, the power consumption of the moving wall and overall heat transfer from the heater is presented, as they are the parameters that are investigated throughout the study. Brief physical descriptions of some are already given in subsection 1.2.1.

The temporal and spatial parameters are converted to nondimensional forms as followed:

$$t^* = \frac{t}{T} \tag{2.1}$$

$$x^* = \frac{x}{d} \tag{2.2}$$

$$y^* = \frac{y}{H} \tag{2.3}$$

The ejected mass flow rate from the orifice is calculated with the help of the incompressible assumptions:

$$\dot{m} = \rho \frac{d_{mw}}{d} \dot{s} \tag{2.4}$$

Equation (2.1) is a manipulated conservation of mass equation; ρ is the density of the fluid, $\dot{s}$ is the velocity of the moving wall which is given in equation (2.5) and d_{mw} is the width of the moving wall.

$$\dot{s} = Awcos(wt + \phi)dt \tag{2.5}$$

where dt is the time step, A, w, and ϕ is the amplitude, frequency and phase of the moving wall, . The nondimensional stroke length is defined as:

$$L = \frac{l}{d} \tag{2.6}$$

where l is the stroke length and d is the width of the orifice. The stroke length is calculated over the ejection phase as:

$$l = \int_0^{\frac{T}{2}} v_{cl}(t)dt \tag{2.7}$$

where the $v_{cl}(t)$ is the centerline axial velocity at the exit of the orifice. The average centerline velocity over a cycle is defined as:

$$\bar{v}_{cl} = \frac{l}{T} \tag{2.8}$$

where the period of moving wall is $T = \frac{1}{f}$. The Reynolds number based on the average centerline velocity is defined as:

$$Re = \frac{\bar{v}_{cl} d}{\upsilon} \tag{2.9}$$

The Stokes number (the ratio of the response time of the particle to the flow-field time scale) is defined as:

$$S = \sqrt{w \frac{d^2}{\upsilon}} \tag{2.10}$$

If the Stokes number is high, $S >> 1$, the jet passes through the fluid with low deflection in its initial trajectory. For low Stokes number, the jet flow is tightly coupled with the fluid.

The jet formation criteria, inverse of the Strouhal number, is defined as:

$$\frac{1}{Sr} = \frac{Re}{S^2} \tag{2.11}$$

The power consumption per unit depth, normal to the page, by the piezoelectric actuator is calculated by:

$$W' = \int_0^T F' dx_{mw} \tag{2.12}$$

where dx_{mw} is the rate of change in the position of the moving wall. The force per unit depth, normal to the page, is calculated as the line integral of the normal pressure at the moving wall:

$$F' = \int_{-\frac{d_c}{2}}^{\frac{d_c}{2}} P dx \tag{2.13}$$

The equation becomes:

$$W' = \int_0^T \left(\int_{-\frac{d_c}{2}}^{\frac{d_c}{2}} P dx \right) A w cos(wt + \phi) dt \tag{2.14}$$

The blowing ratio is defined as:

$$C_b = \frac{\bar{v}_{cl}}{U_\infty} \tag{2.15}$$

The local Nusselt number (Nu_x) and time averaged Nusselt number ($\overline{Nu}$) at the heater based on the orifice width is defined as;

$$Nu_x|_{y^*=1} = \frac{dT}{dy}\frac{d}{\Delta T} \tag{2.16}$$

$$\overline{Nu} = \frac{1}{L}\frac{1}{T}\left[\int_0^T \left(\int_{-\frac{L}{2}}^{\frac{L}{2}} Nu_x|_{y^*=1} dx \right) dt \right] \tag{2.17}$$

where the ΔT is the difference between the heater surface temperature and area averaged temperature of the confined space domain. The local heat flux, $q''_x(W/m^2)$, is defined as:

$$q''_x = -k\frac{dT}{dy} \tag{2.18}$$

where the L is the width of the heater. The total heat transfer from the heater per unit length for each cycle is:

$$Q' = \int_0^T \left(\int_{-\frac{L}{2}}^{\frac{L}{2}} q''_x dx \right) dt \tag{2.19}$$

2.3 Numerical Domains of the Modified Base and Proposed Models

The SJs offer an enhancement in the heat transfer with the help of the characteristics of the impinging jet flow. The main drawback in the SJs is the recirculation of the

heated air back to the heat source, the hybrid synthetic jets offer a solution; however, the alterations in the designs are quite limited. The proposed model introduces new components to control the direction of the flow. It utilizes the SJs' cooling effect and further improves it by removing the unwanted effect of the recirculation. It combines the active valve based micropump concept with the standard SJs. Many parameters are changed when creating the first proposed model (PM-I). The Modified Base Models (MBMs) are created to elucidate each modifications leading PM-I. Finally, PM-II is studied to examine the effect of the cavity aspect ratio, which is the only parameter that cannot be kept constant, on the proposed model. The detailed explanation with the numerical results is provided in section 3.3.

Unlike the BM, the proposed models utilize two orifices with a one-way valve for each. The proposed model I (PM-I) dimensions are the same as the base model (BM). The width of the top and bottom orifice are $d = 1$ mm. The other dimensions are; $D = 27d$, $L_h = 9d$, $H = 10d$, $h_c = 6d$, $d_c = 9d$, and $h = 1$ mm. The moving walls are shown in Figure 2.3. The valve modeling is utilized as explained in subsection 2.3.1. The boundary conditions are; pressure outlets for the openings of the confined space and cavity. The heater wall is kept at a constant temperature of 360 K. The remaining boundaries are treated as no-slip adiabatic walls.

Although MBMs and PM-II are designed with the same working principle of BM and PM-I, respectively, they have different dimensions and operating conditions. Table 2.1 shows which walls are selected as the moving wall and gives altered dimensions. Some dimensions and operation conditions are kept same for each models. These are; $d = 1$ mm, $D/d = 27$, $L/d = 9$, $H/d = 10$, $h_c/d = 6$, and $f = 500$ Hz. The side walls are selected as moving wall for MBM-III, PM-I and PM-II whereas the bottom wall is selected as moving wall for the rest. The following subsection 2.3.1 explains the valve modeling used in the proposed models.

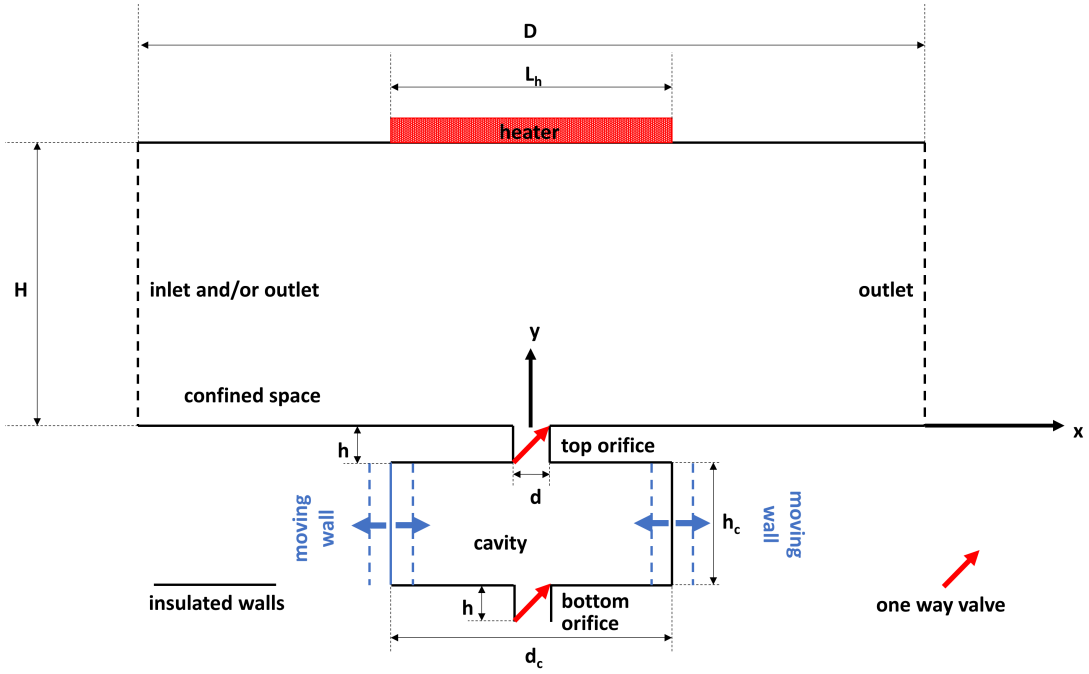

Figure 2.3: The schematic of the proposed model

Table 2.1: The dimensional and geometric parameters of the models

Case	d_c/d	moving wall
BM	9	bottom wall
PM-I	9	side walls
MBM-I	12	bottom wall
MBM-II	10.67	bottom wall
MBM-III	12	side walls
PM-II	12	side walls

2.3.1 Valve Modeling

Check valves are used in the proposed design as shown in Figure 2.3. The check valves allow the flow to pass in only the positive y-direction with the purpose of mixing the quiescent ambient fluid, air, with the fluid in the confined space domain. A code is written to close the top orifice during the suction phase and to open it during the ejection phase. The code models the bottom valve to behave in an opposite manner of the top valve. The valves are modeled with the help of the execute commands

available in FLUENT. The valves are modeled as simple as possible to avoid the additional computational cost, and the effects of the valve's presence on the fluid flow characteristics is not in the scope of this study. The code, given in Appendix B, takes the physical time from the solver and checks whether the criteria provided above are met. For example, if the cycle is in the ejection phase, i.e., the top orifice is ejecting the fluid while the bottom orifice stays closed, the code feeds the information back to the solver, and commands it to open the top valve, whereas the bottom valve is closed. The condition is mathematically given as;

$$cos(w(t - 5dt) + \phi) \tag{2.20}$$

where w is the frequency, t is the physical time, dt is the time step, and ϕ is the phase angle between the top and bottom valves in rad. This condition determines the sign of the velocity of the moving walls. Positive velocity means that the cycle is in the ejection phase and negative value indicates the suction phase. The time step is taken as 1.851852×10^{-6}; therefore, a cycle takes 1080 time steps. The execute command sets the solver to manipulate the scheme file at every 540 time steps so that the solver is only interrupted at each half cycle to avoid unnecessary increase in the computation time, since the boundary condition needs to be checked only once during a cycle.

2.4 Governing Equations

The governing equations of fluid domain consist of continuity, momentum, and energy equations. 2D incompressible continuity and unsteady momentum equations are given as follows:

$$\frac{\partial}{\partial x_i}(u_i) = 0 \tag{2.21}$$

$$\frac{\partial}{\partial t}(u_i) + u_j \frac{\partial}{\partial x_j}(u_i) = -\frac{1}{\rho}\frac{\partial p}{\partial x_i} + v\frac{\partial^2}{\partial x_j x_j}(u_i) \tag{2.22}$$

where x_1 is the x-direction and u_1 is the transverse velocity (u_x) while x_2 is y-

direction and u_2 is the axial direction (u_y) in cartesian coordinates. v, ρ and p are the kinematic viscosity, density and pressure term, respectively. The velocity and pressure variables are manipulated with the time-averaged variables to model the turbulence flow as given:

$$u_i = U_i + u_i' \tag{2.23}$$

$$p = P + p' \tag{2.24}$$

where the capitalized letters represent the time-averaged flow variables and apostrophized represents their fluctuation terms.

Putting equations (2.23) and (2.24) into (2.22) with some mathematical modifications results in Unsteady Reynolds-averaged Navier–Stokes (URANS) equations;

$$\frac{\partial\left(\rho U_i\right)}{\partial t} + \frac{\partial}{\partial x_j}\left(\rho U_i U_j\right) = -\frac{\partial P}{\partial x_i} + \frac{\partial}{\partial x_j}\left[\mu\left(\frac{\partial U_i}{\partial x_j} + \frac{\partial U_j}{\partial x_i}\right) - \rho\overline{u_i' u_j'}\right] \tag{2.25}$$

The last term on the right-hand side of the equation (2.25) is the Reynolds stress tensor that contains 9 unknowns. It is simplified with the Boussinesq approximation (2.26). The Boussinesq approximation for the Reynolds stress for both normal and shear stresses with the help of Kronecker Delta symbol δ_{ij} (2.27) represented as:

$$-\rho\overline{u_i' u_j'} = 2\mu_t\left(S_{ij} - \frac{1}{3}\frac{\partial U_k}{\partial x_k}\delta_{ij}\right) - \frac{2}{3}\rho k\delta_{ij} \tag{2.26}$$

Kronecker Delta symbol δ_{ij}:

$$\delta_{ij} = \begin{cases} 1 & i = j \\ 0 & i \neq j \end{cases} \tag{2.27}$$

The mean rate of strain rate tensor S_{ij}:

$$S_{ij} = \frac{1}{2}\left(\frac{\partial U_i}{\partial x_j} + \frac{\partial U_j}{\partial x_i}\right) \tag{2.28}$$

The energy equation without the viscous dissipation term is:

$$\frac{\partial}{\partial t}(\rho h) + u_i \frac{\partial}{\partial x_i}(\rho h) = \frac{\partial}{\partial x_i}\left(k_{\text{eff}} \frac{\partial}{\partial x_i} T\right) \tag{2.29}$$

where the k_{eff} is the effective conductivity consisting of the turbulent thermal conductivity (k_t) and the thermal conductivity of the fluid (k). The right-hand side accounts for conductive heat transfer and the volumetric energy sources, respectively.

The enthalpy term (h) is given as:

$$h = \sum_j Y_j h_j + \frac{p}{\rho} \tag{2.30}$$

The first term on the right-hand side combines different species' enthalpy values. The domain in the current work contains only one species; therefore, this term is redundant and sensible enthalpy reduces to:

$$h = \int_{T_{ref}}^{T} c_p dT + \frac{p}{\rho} \tag{2.31}$$

The final form of the energy equation without the viscous dissapation and volumetric energy sources for incompressible flows is reduced to:

$$\rho c_p \frac{\partial T}{\partial t} + \rho c_p u_i \frac{\partial T}{\partial x_i} = \frac{\partial}{\partial x_i}\left(k_{\text{eff}} \frac{\partial T}{\partial x_i}\right) \tag{2.32}$$

The Boussinesq assumption (2.26) reduces the number of independent unknowns of the Reynolds stress tensor to two: the turbulent viscosity (μ_t) and the turbulent kinetic energy (k). Additional equation(s) are proposed in the literature to determine the two unknowns by modeling the turbulence regime.

The most common turbulence models available in the literature are $k - \varepsilon$ and $k - \omega$ turbulence models for jet flows. For the selection of the turbulence model, Kotapati et al. [59] suggest the turbulence models that can take account for transition between laminar and turbulent flows. Kotapati et al. [59] stated that turbulent fluctuations

mostly take place outside the orifice exit during the blowing period and they are centered around the phase when the local phase-averaged velocity is at its highest. The fluid accelerates toward the orifice during the intake phase of the cycle, which helps stabilize the stream. As a result, there are not many fluctuations while the cycle is in this stage. On the other hand, the velocity fluctuations within the orifice and the cavity are not stabilized. The transition mostly occurs within the cycle's acceleration stage when the bulk velocity rises from its lower limit to its maximum.

Standard $k-\omega$ and $k-\varepsilon$ models are not capable of solving problems including transition between laminar to turbulence. Whereas GEKO, BSL and Menter's Shear-Stress Transport (SST) $k-\omega$ methods provide two option for the transition regime. The $k-\omega$ SST model includes the turbulence shear stress transport equations for the turbulent viscosity. Aforementioned characteristics make this model more accurate and reliable for various flows (for example, adverse pressure gradient flows, aerofoils, and transonic shock waves) compared to the standard $k-\omega$ and the BSL -models. Therefore, in the literature, $k-\omega$ SST turbulence model is stated as the superior turbulence model compared to aforementioned models for the jet flows [60]. Furthermore, a correlation-based transition model was proposed by Menter et al. [61], to model the transition regime with correlation-based approach. The transition SST $k-\omega$ turbulence model solves four equation (two more equation than the aforementioned models) and provides more accurate solution by including numerous transition-regime-related effects such as freestream turbulent length scale, streamline curvature and cross-flow transition. The transition SST $k-\omega$ model also includes transport equation for the turbulent kinetic energy, k, and specific dissipation rate, ω. Only three terms are manipulated to account for the transition regime with respect to SST $k-\omega$. Two of which are the production and dissipation terms in the kinetic energy equation and the last one is the blending function (responsible for switching between ω, specific dissipation rate equation, and ε, dissipation rate equation) in the specific dissipation equation. For details of the Merter's SST $k-\omega$ turbulence model, two-equation eddy-viscosity turbulence models for engineering applications from Menter et al. [62] is available. In the following subsection, Menter's SST method and the modifications to include the transition regime are elaborately discussed.

2.4.1 The Turbulence Models

The synthetic jet flow is shown to have transition regime between laminar and turbulent in the literature. Therefore, transition SST $k-\omega$ method is selected for the turbulence modeling. The transition model is developed from the original Menter's SST turbulence model. The following subsection explains the original method and the transition SST model.

2.4.1.1 The Original Menter's SST Model

The Menter's SST model utilizes the turbulent kinetic energy (k), and the specific dissipation rate (ω) to solve for two unknowns in the Boussinesq assumption (2.26). Transport equations are solved for both k (in equation (2.33)) and ω (in equation (2.43)). The transport equation expresses the characteristics of the transportation of a scalar quantity in a domain. In general, the transport equation shows that the time-dependent variation of the quantity inside the control volume and the summation of the quantity entering and exiting the control volume equals to a source of the quantity. Commonly, the quantity entering and exiting the control volume is further divided into two parts: convection and diffusion terms. The convective term is related to the transported quantity through the boundaries of the control volume due to the flow, and the diffusion term describes the diffusion of the quantity due to its gradient.

The transport equation for the turbulence kinetic energy is given as:

$$\frac{\partial}{\partial t}(\rho k)+\frac{\partial}{\partial x_i}\left(\rho k u_i\right)=\frac{\partial}{\partial x_j}\left(\Gamma_k \frac{\partial k}{\partial x_j}\right)+\widetilde{G}_k-Y_k \tag{2.33}$$

where:

$$\widetilde{G}_k = min(G_k, 10\rho\beta^* k\omega) \tag{2.34}$$

$$G_k = -\rho\overline{u_i' u_j'}\frac{\partial u_j}{\partial u_i} \tag{2.35}$$

$$\beta^* = \beta_i^* \left[1 + \zeta^* F\left(\mathrm{M}_t\right)\right] \tag{2.36}$$

$$\beta_i^* = \beta_\infty^* \left(\frac{4/15 + \left(\mathrm{Re}_t / R_\beta\right)^4}{1 + \left(\mathrm{Re}_t / R_\beta\right)^4} \right) \tag{2.37}$$

$$Re_t = \frac{\rho k}{\mu \omega} \tag{2.38}$$

Constants in equations (2.37) and (2.36) are $\zeta^* = 1.5$, $R_\beta = 8$, $\beta_\infty^* = 0.09$.

The effective diffusivity for k is $\Gamma_k = \mu \frac{\mu_t}{\sigma_k}$. σ_k and two blending functions are given as:

$$\sigma_k = \frac{1}{F_1/(1.176) + (1 - F_1)} \tag{2.39}$$

The first blending function (F_1) is responsible for invoking $k - w$ model near the wall with a value of one. Whereas, it invokes $k - \varepsilon$ model in the free stream by having a value of zero.

$$F_1 = \tanh\left(\Phi_1^4\right) \tag{2.40}$$

$$\Phi_1 = \min\left[\max\left(\frac{\sqrt{k}}{0.09\omega y}, \frac{500\mu}{\rho y^2 \omega}\right), \frac{4\rho k}{\sigma_{\omega,2} D_\omega^+ y^2}\right]$$

D_ω^+ represents the cross diffusion term's positive portion.

$$D_\omega^+ = \max\left[2\rho \frac{1}{\sigma_{\omega,2}} \frac{1}{\omega} \frac{\partial k}{\partial x_j} \frac{\partial \omega}{\partial x_j}, 10^{-10}\right]$$

$$F_2 = \tanh\left(\Phi_2^2\right) \tag{2.41}$$

$$\Phi_2 = \max\left[2\frac{\sqrt{k}}{0.09\omega y}, \frac{500\mu}{\rho y^2 \omega}\right]$$

$$Y_k = \rho\beta^* k\omega \tag{2.42}$$

The first term on the left-hand side of the transport equation of the turbulence kinetic energy (2.33) is the time-dependent variation of the turbulent kinetic energy inside the control volume, the second term is the convection of the turbulent kinetic energy associated with the motion of the flow. The first term on the right-hand side is the diffusion term and the remaining terms are the production and destruction of the turbulent kinetic energy, as the source terms of the equation. The rest of the transport equations have a similar layout; therefore, only distinct terms are explained in the related sections.

The transport equation for the turbulence specific dissipation rate is given as:

$$\frac{\partial}{\partial t}(\rho\omega) + \frac{\partial}{\partial x_i}(\rho\omega u_i) = \frac{\partial}{\partial x_j}\left(\Gamma_\omega \frac{\partial \omega}{\partial x_j}\right) + G_\omega - Y_\omega + D_\omega \tag{2.43}$$

where the effective diffusivity for ω is $\Gamma_\omega = \mu\frac{\mu_t}{\sigma_w}$, σ_ω is given as:

$$\sigma_\omega = \frac{1}{F_1/2 + (1 - F_1)/(1.168)} \tag{2.44}$$

$$Y_\omega = \rho\beta\omega^2 \tag{2.45}$$

$$\beta = \beta_i\left[1 + \frac{\beta_i^*}{\beta_i}\zeta^* F\left(\mathrm{M}_t\right)\right] \tag{2.46}$$

$$\beta_i = 0.075F_1 + 0.0828(1 - F_1)$$

$F\left(\mathrm{M}_t\right)$, in (2.36) and (2.46), is the compressiblity correction factor, for incompressible flow it is zero.

$R_k = 6$, $R_\omega = 2.95$, and $\alpha_0^* = 0.024$ are the constants of the model. The remaining model constants are given by Menter et al. [62].

The cross-diffusion term, D_ω, is controlled by the blending function given equation (2.47).

$$D_\omega = 2(1.168)(1 - F_1)\rho\frac{1}{w}\frac{\partial k}{\partial x_j}\frac{\partial w}{\partial x_j} \tag{2.47}$$

2.4.1.2 The Transition SST Model

The transition SST $k - \omega$ model includes transport equation for turbulent kinetic energy (k), and specific dissipation rate (ω). Only three terms are manipulated to account for transition regime with respect to SST $k - \omega$ method. Two of the terms are the production and the dissipation terms in the kinetic energy equation and the last one is the first blending function, responsible for switching between specific dissipation rate equation and dissipation rate equation, in the specific dissipation equation.

The production term is multiplied by an effective turbulence intermittency called γ_{eff}. The turbulence intermittency represents the time that the turbulent fluctuations are present in the boundary layer. The γ_{eff} takes values between zero and one. For laminar boundary layer, it removes the production term. For the turbulent boundary layer, it converts the production term back to the original value as presented in the equation (2.49).

$$\frac{\partial}{\partial t}(\rho k) + \frac{\partial}{\partial x_i}(\rho k u_i) = \frac{\partial}{\partial x_j}\left(\Gamma_k \frac{\partial k}{\partial x_j}\right) + \widetilde{P}_k - \widetilde{D}_k \tag{2.48}$$

where

$$\widetilde{P}_k = \gamma_{eff}\tilde{G}_k \tag{2.49}$$

$$\gamma_{\text{eff}} = \max(\gamma, \gamma_{sep}) \tag{2.50}$$

in which, γ is the turbulent intermittency and the γ_{sep} takes into account the separation based transition.

$$\gamma_{\text{sep}} = \min\left(2\max\left[\left(\frac{Re_v}{3.235Re_{\theta c}}\right) - 1, 0\right] F_{\text{reattch}}, 2\right) F_{\theta t}$$

where the vorticity Reynolds number, F_{reattch} and Re_t are given as;

$$Re_v = \frac{\rho y^2}{\mu}\frac{\partial u}{\partial y}$$

$$F_{\text{reattch}} = e^{-\left(\frac{Re_t}{20}\right)^4}$$

$$Re_t = \frac{\rho k}{\mu\omega}$$

The dissipation term is replaced by the multiplication of itself with a limiter, resulting in a definition given in equation (2.51).

$$\widetilde{D}_k = \min\left(\max\left(\gamma_{eff}, 0.1\right), 1.0\right) Y_k \tag{2.51}$$

In the transition SST $k-\omega$ model, it is observed that the blending function at the center of the laminar boundary layer has a tendency to take a value of zero (switching the model to $k-\varepsilon$) near the wall where it is expected to take a value one (making the model $k-\omega$) as explained by Menter et al. [61]. In order to avoid this inconvenience, a new blending function is introduced in the equation (2.52). Thus, the first blending function changes from F_1 to $F_{1,new}$.

$$F_{1,new} = max(F_1, F_3) \tag{2.52}$$

The F_1 is the same blending function in equation (2.40). $F_3 = e^{-(R_y/120)^3}$ and $R_y = \frac{\rho y\sqrt{k}}{\mu}$.

The turbulence intermittency, γ, introduces a new transport equation to the solver:

$$\frac{\partial(\rho\gamma)}{\partial t} + \frac{\partial\left(\rho U_j \gamma\right)}{\partial x_j} = P_{\gamma 1} - E_{\gamma 1} + P_{\gamma 2} - E_{\gamma 2} + \frac{\partial}{\partial x_j}\left[\left(\mu + \frac{\mu_t}{\sigma_\gamma}\right)\frac{\partial \gamma}{\partial x_j}\right] \quad (2.53)$$

On the left-hand side of equation (2.53), rate of change of the intermittency respect to time and standard convective term, which takes account for the intermittency transported through the boundaries due to the flow are presented. On the right-hand side, the source term of the transport equation is given. The source term is the combination of the production rate, the dissipation rate, destruction source and relaminarization source, respectively. The source terms depend on the local state of the regime. The last term on the right-hand side is the diffusion term, transportation of the intermittency due to the gradient. Transitional production and the dissipation rate terms are:

$$P_{\gamma 1} = 2F_{length}\rho S[\gamma F_{onset}]^{0.5}$$

$$E_{\gamma 1} = P_{\gamma 1}\gamma$$

$$F_{\text{onset 1}} = \frac{Re_v}{2193 Re_{\theta c}}$$

$$F_{\text{onset 2}} = \min\left(\max\left(F_{\text{onset 1}}, (F_{\text{onset 1}})^4\right), 2.0\right)$$

$$F_{\text{onset 3}} = \max\left(1 - \left(\frac{Re_T}{25}\right)^3, 0\right)$$

$$F_{\text{onset}} = \max\left(F_{\text{onset 2}} - F_{\text{onset 3}}, 0\right)$$

where F_{onset} switches on the production intermittency, F_{length} controls the strength of productions (stronger production means shorter transition length). S is the strain rate magnitude.

The F_{length} and $Re_{\theta c}$ are function of the transition Reynolds number of the upstream, $\widetilde{Re_{\theta t}}$ [63].

The third and the fourth terms are the destruction/relaminarization sources.

$$P_{\gamma 2} = 0.06\rho\Omega\gamma e^{-(\frac{R_T}{4})^4}$$

$$E_{\gamma 2} = 50 P_{\gamma 2}\gamma$$

The transport equation for the transition Reynolds number of the upstream, $\widetilde{Re_{\theta t}}$, given as:

$$\frac{\partial\left(\rho\widetilde{Re_{\theta t}}\right)}{\partial t} + \frac{\partial\left(\rho U_j\widetilde{Re_{\theta t}}\right)}{\partial x_j} = P_{\theta t} + \frac{\partial}{\partial x_j}\left[2\left(\mu+\mu_t\right)\frac{\partial\widetilde{Re_{\theta t}}}{\partial x_j}\right] \tag{2.54}$$

$$P_{\theta t} = 0.03\frac{\rho}{t}\left(Re_{\theta t} - \widetilde{Re_{\theta t}}\right)(1.0 - F_{\theta t})$$

$$t = \frac{500\mu}{\rho U^2}$$

$$F_{\theta t} = \min\left(\max\left(e^{-(\frac{Re_\omega}{1e+5})^2}e^{\left(-\frac{y}{\delta}\right)^4}, 1.0 - \left(\frac{\gamma - 1/50}{1.0 - 1/50}\right)^2\right), 1.0\right)$$

$$Re_\omega = \frac{\rho\omega y^2}{\mu}$$

$$\delta = \frac{50\Omega y}{U}\frac{15}{2}\frac{\widetilde{Re_{\theta t}}\mu}{\rho U}$$

The turbulent viscosity μ_t, S representing the the strain rate magnitude, is:

$$\mu_t = \frac{\rho k}{\omega}\frac{1}{max[\frac{1}{\alpha^*}, \frac{SF_2}{\alpha_1}]} \tag{2.55}$$

where α and α^*, the dampers of the turbulent viscosity for the low Reynolds number, are given in the following equations:

$$\alpha^* = \alpha^*_\infty(\frac{\alpha^*_0 + Re_t/R_k}{1 + Re_t/R_k})$$

$$Re_t = \frac{\rho k}{\mu\omega}$$

The remaining model constants are given in the Menter et al. [61].

Widely used solvers for the governing equations are pressure-based and density-based. The density-based solvers are intended for the high Mach number flows; therefore, it is advantageous in flows with strong dependency between density, momentum and energy. The pressure-based solvers are derived for incompressible and mildly compressible flows. The following subsection explains the pressure-based pressure-velocity couplings to solve the governing equations.

2.4.2 Pressure-Velocity Couplings

The pressure-based solvers utilize sequential and coupled algorithms. The segregated algorithm takes almost half as much memory space as the coupled algorithm. The selected solver is pressure-based segregated PISO scheme since the fluid is assumed to be incompressible and the memory is an important restriction. The segregated algorithm starts with solving for momentum predictor (at this step the velocity field does not satisfy the continuity equation) then the results of the momentum predictor is used for solving the pressure field. The velocity field is updated with a reformatted continuity equation. Even though, the continuity equation is inherently satisfied at the previous state, the pressure field is no longer satisfied. The dilemma is resolved by using the pressure-velocity couplings.

Semi-Implicit Method for Pressure Linked Equations (SIMPLE) solves the momentum predictor equation again and loop each step described in the previous paragraph until the residuals converges. One of the alternative for the SIMPLE algorithms is SIMPLEC which is developed for faster convergence for basic problems such as laminar flows. The Pressure-Implicit with Splitting of Operators (PISO) present useful

solution for unsteady and low Courant number flows. The selected pressure-velocity coupling is discussed in subsection 2.4.2.1.

2.4.2.1 The PISO Scheme

One of the fundamental differences between the SIMPLE and the PISO algorithms is that the former was intended for steady-state flows. It has under-relaxation terms to artificially increase the diagonal dominance in the matrix while solving the momentum equation. Whereas the unsteady flows are inherently diagonal dominant since the time derivative terms are on the diagonal of the related matrix, providing stability to the equation. If the time step is low enough, the Courant number (Co) is lower than one; under-relaxation would not be required in the PISO scheme. Therefore, the PISO scheme is utilized to solve the governing equations. The PISO scheme requires non-orthogonal correctors when the meshes are non-orthogonal. In the present study, meshes are deliberately constructed with relatively small non-orthogonality to avoid the extra computational cost.

CHAPTER 3

VERIFICATION AND RESULTS OF THE CASE STUDIES

In this chapter, a verification study is carried out using a numerical study in the literature as a benchmark. Different cases are built to illustrate each innovations leading to the modified hybrid synthetic jet. Furthermore, proposed design is set to operate under a cross flow.

3.1 Base Model Verification Results

Four verification parameters are selected: Base model's the axial and the transverse velocity profiles at the exit of the orifice, the mass-weighted average axial velocity at the exit of the orifice and the local Nusselt number distribution on the heater. They are compared with the numerical study done by Jagannatha et al. [58] for t*=1. Numerical domain is constructed as explained in section 2.1. Figures 3.1, 3.2 and 3.3 show similar velocity behaviors verifying the current numerical study. The selected turbulence model requires y+ and y* values of one; therefore, local refinements for the element size near the wall are employed, as explained in section 2.1. As a result, the velocities may overshoot near the wall region, resulting in undershoot in the middle. The vorticity and the pressure contours matches with the reference study by Jagannatha et al. [58]. The Reynolds number is 685 in the study by Jagannatha et al. [58], whereas the current numerical study resulted in Reynolds number of 692, as given in Table 3.2. The error between the Re is less then 1%. Maximum error in the mass weighted averages is 9%, which could be due the grid density difference and the selection of the turbulence model.

Local Nusselt number is compared at two different nondimensional times. The crucial

nondimensional times are $t^* = 0.61$, since the impingement occurs at that time and $t^* = 0.81$ at which the stagnation effect reduces and the wall jets dominate the heat transfer. Figure 3.4a shows that the current model captures the impinging effect of the jet around the stagnation region, since the stagnation point should have the highest local Nu, which is repeatedly mentioned in the literature [4]. Figure 3.4b shows the local Nu after the impinging phenomenon; therefore, the peak Nu is moved away from the center. The peaks are created by the wall jets, while the vortex rings widen the plots. The models are matching at $x/d = 0$; however, the inadequate density of the grid in the transverse direction and the selected turbulence model (SST $k - \omega$) might cause a rapid decay in the Nu for Jagannatha et al. [58]. Based on verification results, it can be concluded that the current numerical model is reliable and can be used for further investigations.

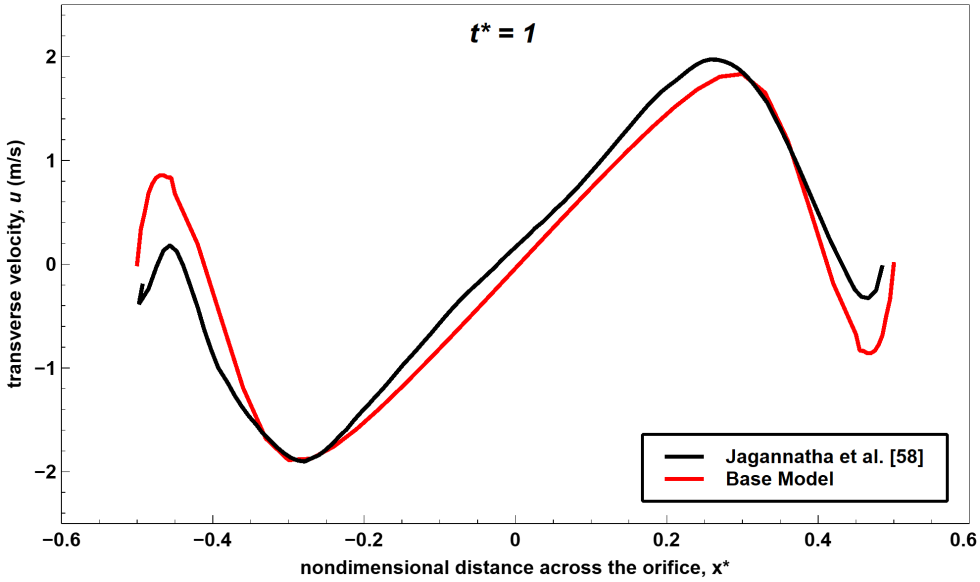

Figure 3.1: Transverse velocity profile at the exit of the orifice for t*=1

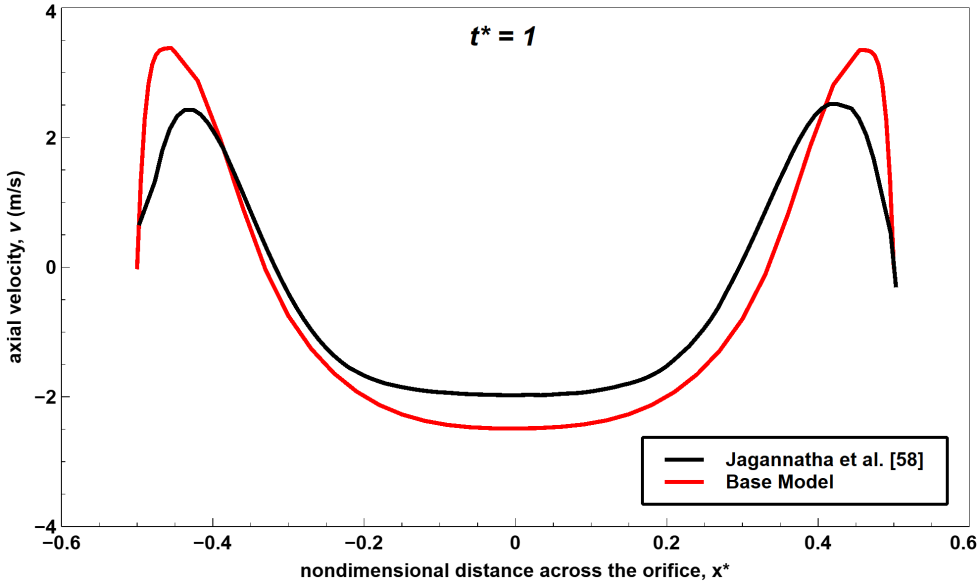

Figure 3.2: Axial velocity profile at the exit of the orifice for t*=1

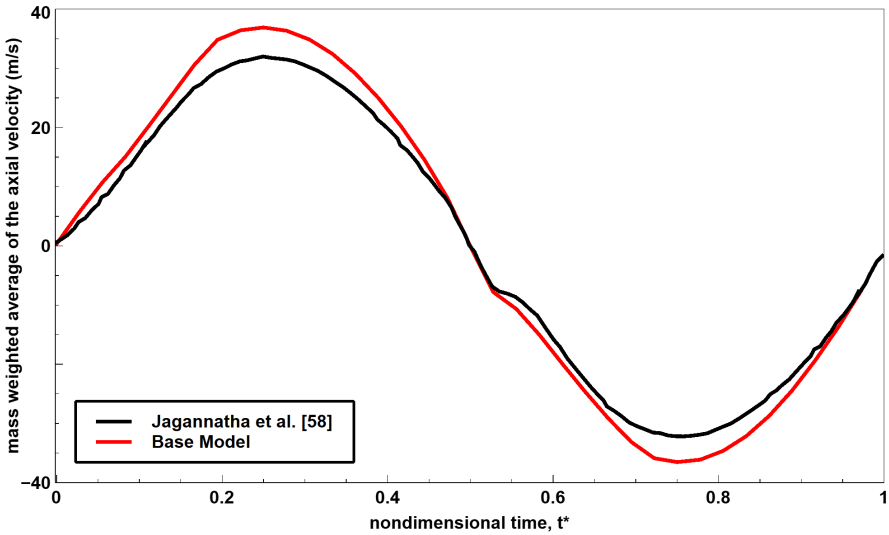

Figure 3.3: Mass weighted average axial velocity in the orifice domain

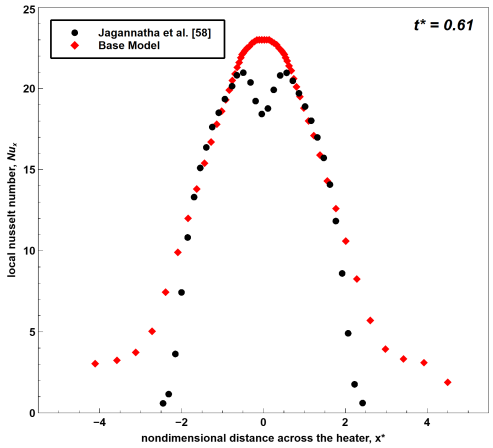

(a) Local Nu distribution at the heater at $t^* = 0.61$

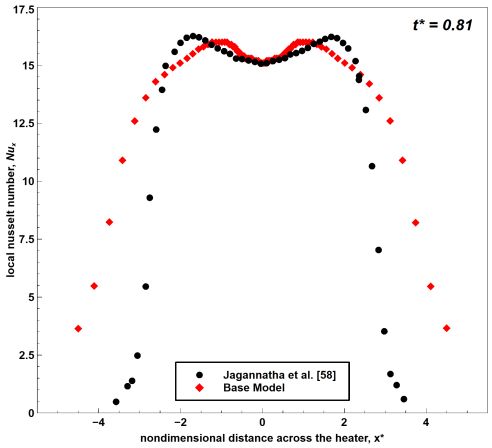

(b) Local Nu distribution at the heater at $t^* = 0.81$

Figure 3.4: Local Nu profile at the heater for selected nondimensional times

3.2 Proposed Model Mesh Independence Analysis

The proposed model is designed with the same cavity, confined space and heater size as Jagannatha et al. [58] while the boundary conditions are kept the same when applicable. Two valves are implemented, one for each orifice, to achieve unidirectional flow. The mesh independence study compares three different mesh resolutions, and the results of the area-weighted average temperature of the confined space and the mass-weighted average of the exit axial velocity of the top orifice ensure that mesh independence is achieved. Table 3.1 provides information on the cell count and mesh refinements of the orifice used in three distinct meshes. The proposed model I (PM-I) is selected for the refinement study. The area weighted average temperature of the confined space and the mass weighted average of the exit axial velocity of the top orifice are chosen as the selection criteria for the mesh selection. The results are given in the Figures 3.5 and 3.6. The selected turbulence model required y+ and y* values to be close to one. Therefore, the methodology presented in section 2.1 is followed for each refinement study.

Table 3.1: Meshes for the domain and the orifice

	Number of cells in flow domain	Number of cells in the orifice
Coarse	60804	1302
Moderate	135590	2240
Fine	266614	8118

Figures 3.5, 3.6 and 3.7 show that the moderate grid satisfies the mesh independence since the difference between the area weighted average confined space temperature of moderate and fine grids is less than 1%. Mass weighted average axial velocity in the orifice is nearly same for each configuration. Furthermore, at $t^* = 0.61$ (at which highest temperature gradient occurs on the heater) heat fluxes are investigated and shown maximum 6.5% difference between the fine and moderate mesh, and the behavior is close enough to select moderate mesh grid as shown in Figure 3.8.

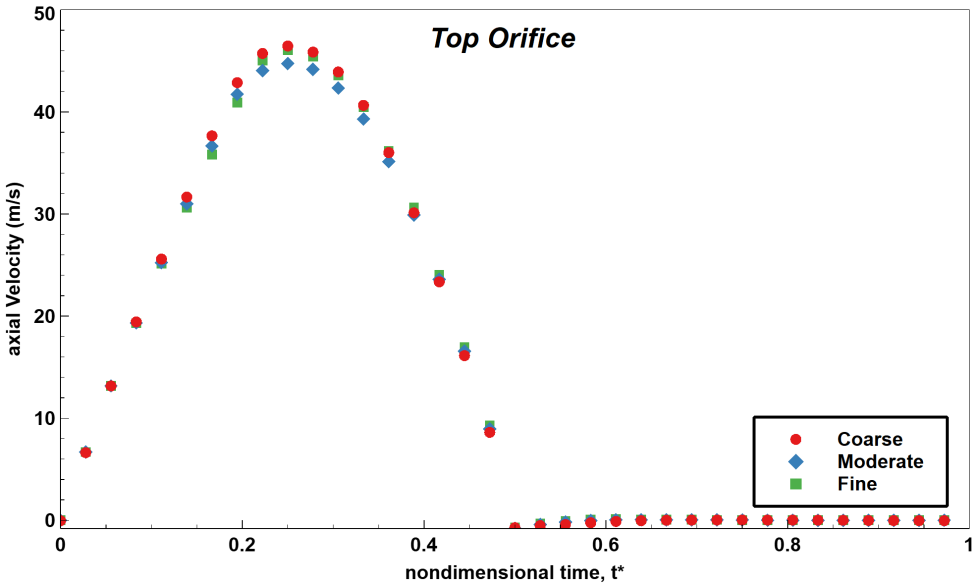

Figure 3.5: Comparison of the mass weighted average axial velocity of air in the top orifice domain with different meshes

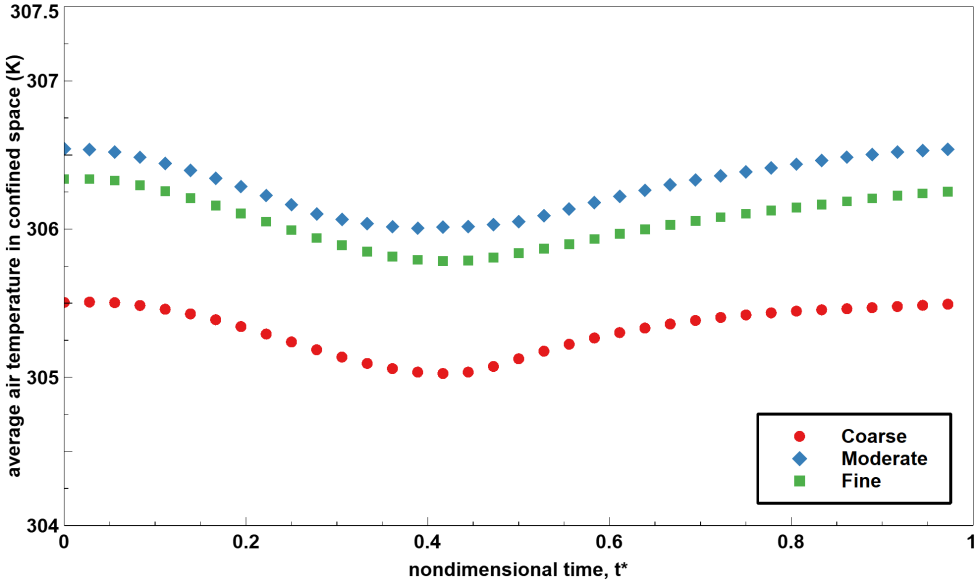

Figure 3.6: Comparison of the area weighted average temperature of air in the confined space domain with different meshes

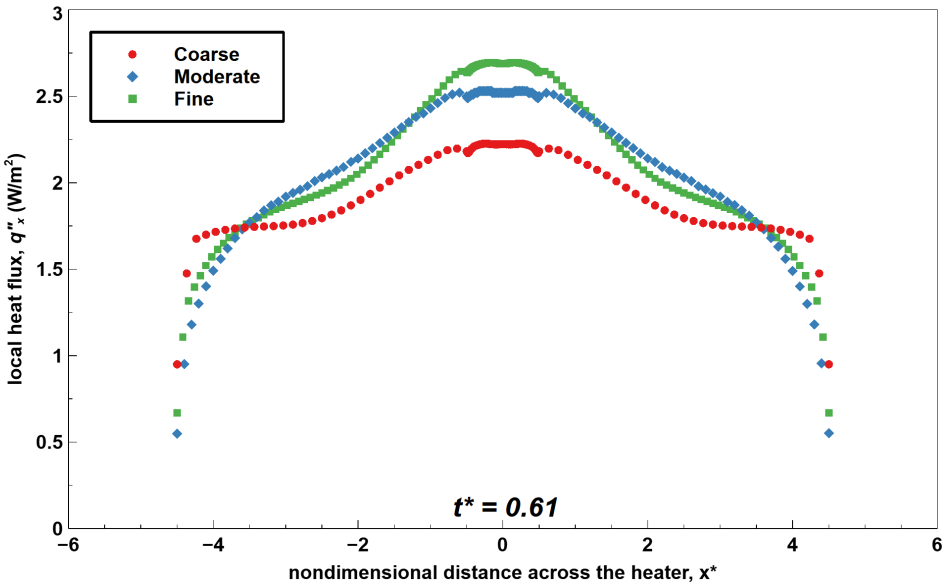

Figure 3.7: Comparison of the local heat flux distribution at the heater at $t^* = 0.61$ with different meshes

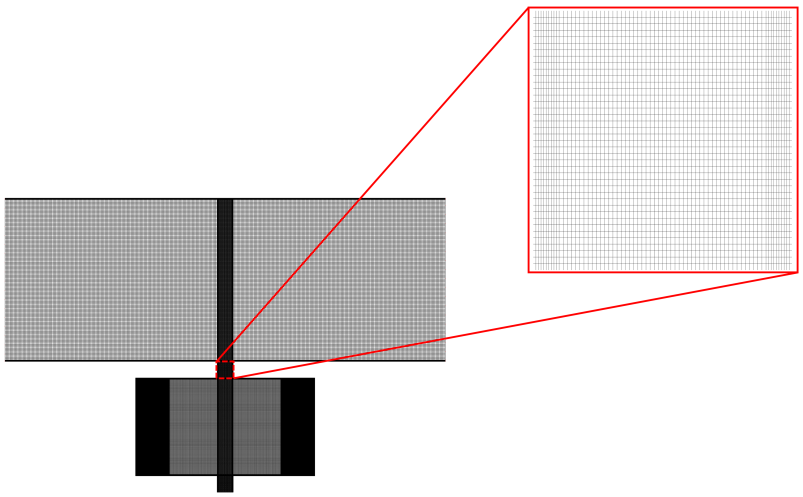

Figure 3.8: The selected mesh: moderate grid and detailed section of the grid in orifices

It is worth noting that a similar mesh configuration to moderate grid is chosen for the other configurations of the proposed design.

3.3 Modified Base Models and Proposed Models Results

The results of the proposed model is discussed with the parameters introduced in section 2.2. The velocity profiles at the exit of the top orifice in different time steps are investigated. These parameters are compared with the base model. Finally, the performance of the proposed model at different blowing rates is presented by comparing it with an equivalent SJ in subsection 3.3.4.

Table 3.2 compares the parameters defined in section 2.2. The proposed model I (PM-I) shows a substantial increase in work per unit length by the moving wall compared to BM. The reason is that the moving wall of the proposed model has a higher sweep area (amount of area swept during a single cycle), resulting in higher ejected mass flow rate through the top orifice in one half cycle. Even though the amplitudes of the diaphragms are kept the same, 1 mm, BM has a 9 mm moving wall, whereas PM-I has a combined 12 mm moving walls. While the difference results in higher L and Re values, it also requires higher work input.

Aside from the different moving wall dimensions, the difference in the flow behaviors at various nondimensional times causes the difference in the work input. The fluid in the cavity of PM-I needs more pressure gradient in the ejection phase since the moving walls of PM-I operate almost against each other colliding the flows created by the moving walls at the middle section of the cavity and creating high pressure within the cavity. On the other hand, the unidirectional flow of PM-I should theoretically reduce the work input. Positive momentum created around the exit of the orifice and in the cavity domain during the ejection phase of BM must be diminished while transitioning to the suction phase. Furthermore, a negative momentum must be created before the suction phase in the confined space and the cavity domain. In the same way, the opposite must take place for the transition from suction to ejection. Further investigations are required to understand these phenomena; therefore, MBMs and PM-II are discussed in subsections 3.3.1 and 3.3.2 to elucidate each modifications leading PM-I. It is worth mentioning that Stokes number is kept as the same for all cases with a value of 13.211.

Table 3.2: The output parameters of models

Case	Re	L	Sr^{-1}	$W'(J/m)$	$\overline{Nu}$	$Q'(J/m)$
BM	692	24.861	3.963	0.0199	18.646	0.216
PM-I*†	820	29.530	4.699	0.0314	18.556	0.242
MBM-I*‡	917	32.998	5.252	0.0423	19.980	0.246
MBM-II†	820	29.530	4.699	0.0301	18.140	0.219
MBM-III*‡	865	31.100	4.955	0.0429	19.604	0.239
PM-II*	835	30.100	4.784	0.0319	18.746	0.249

3.3.1 Discussion of the Models with the Same Mass Flow Rates

In order to evaluate the aforementioned effects of PM-I on the work input, an extra model is built. Modified Base Model-I (MBM-I) has a $12mm$ long diaphragm, ensuring that the ejected mass flow rates in the same periods are the same as in PM-I case. The results shown in Table 3.2 make it clear that the advantages of PM-I overcome the deficiency in the work input. Even though PM-I and MBM-I have the same ejected mass flow rates during the ejection phase, the centerline velocities differ. The collision of the flows in the middle results in a more dispersed velocity profile at the exit of the top orifice in PM-I, as represented in Figure 3.9. As a result, PM-I has a lower peak velocity (centerline velocity) at the orifice, even with the same mass fluxes. As given in Table 3.2, the resulted Stroke length is lower than MBM-I by 11%; on the other hand, the work input is decreased by 26%. In order to distinguish the extent of the advantage of the unidirectional flow in work input of PM-I, MBM-III is built. MBM-III has two moving walls on the side walls, which have the exact dimensions as PM-I. The results show little difference in the work input between MBM-III and MBM-I, proving that the disadvantage of having moving walls on the side walls is almost negligible. Moreover, the comparison between MBM-I and MBM-III suggests that the considerable difference in the stroke length between MBM-I and PM-I is not solely due to the location of the moving wall. Figures 3.10, 3.11 and 3.12 examine

*Same ejected mass flow rates
†Same nondimensional stroke length
‡Different moving wall location

the effect of the impinging phenomenon on the thermal characteristic for the cases with the same ejected mass flow rates. The results show that the recirculated air removes less heat flux from the heater, even though MBM-I and MBM-III have a higher impinging characteristic than PM-I and PM-II. The fundamental heat flux difference between MBMs and PMs are underestimated due to the absence of the far-field for the bottom orifice. The conservative results show 11% and 20% enhancement of the peak value of the heat flux of PM-I and PM-II respectively, during the impingement compared to MBMs. After the impingement, the differences in the peak values slowly changes to 15% and 18% for PM-I and PM-II, respectively, at $t^* = 0.61$ then decrease to 9% and 13% for PM-I and PM-II, respectively, at $t^* = 0.81$. Figure 3.13 compares the heat transfer rate per unit length between MBMs and PMs with the same ejected mass flow rates. Previously created vortexes are dissipating during the first half of the cycle. While suction phases of MBMs cancel out some of the dissipation of the vortexes, PMs, inhaling the air from the bottom orifice, lacks this feature (Figure 3.21). Therefore, a lower heat transfer rate is observed in PMs during the inhaling phase, as seen in Figure 3.13. During the ejection phase, the heat transfer rate of the PMs rapidly increases and compensates for the shortage in the total heat transfer per unit length in a cycle, with a 2% difference when MBM-I and PM-I are compared. The total heat transfer per unit length in a cycle is 0.2464 and 0.2416 for MBM-I and PM-I, respectively.

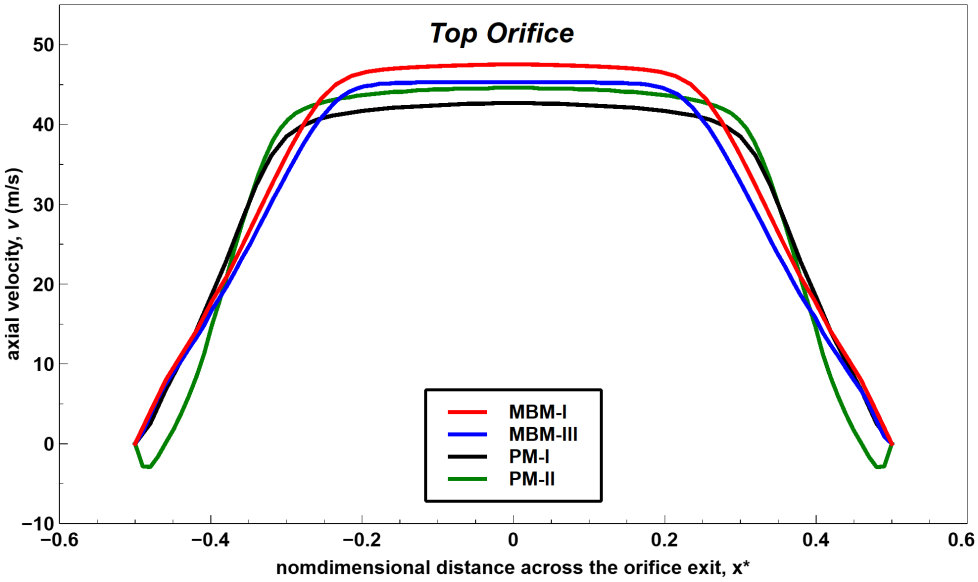

Figure 3.9: Orifice exit axial velocities of the cases with the same ejected mass flow rate at t*=0.33

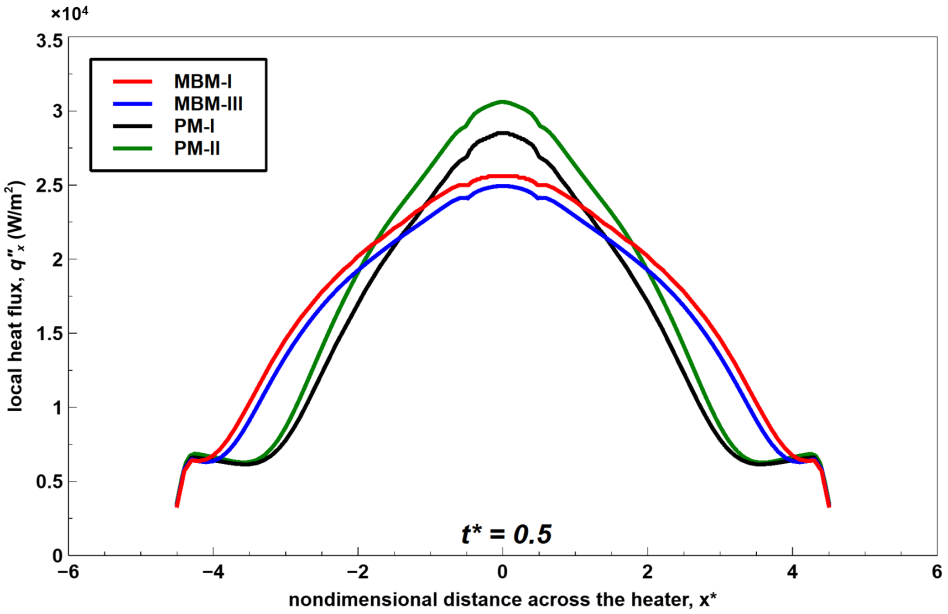

Figure 3.10: Distribution of the heat flux across the heater at $t^* = 0.5$

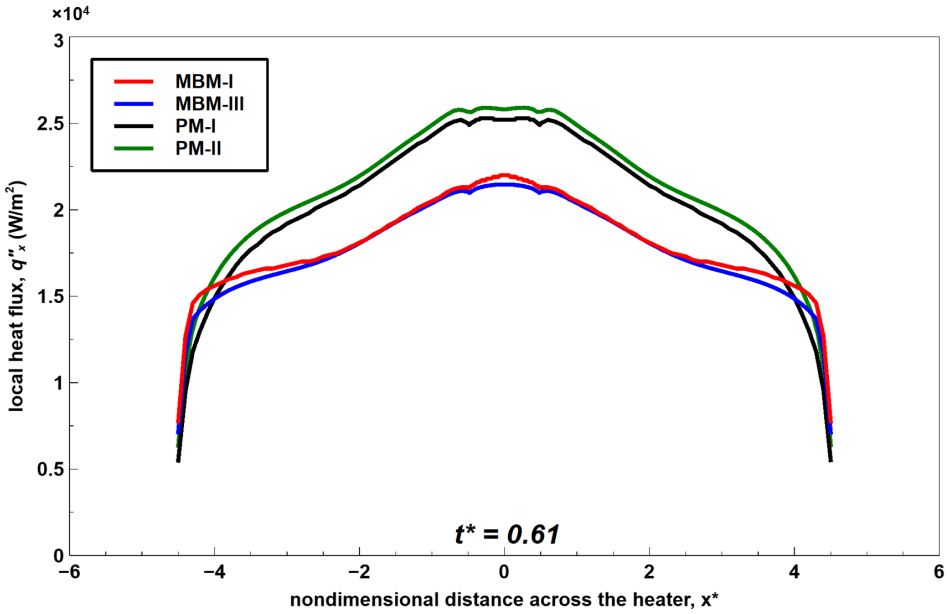

Figure 3.11: Distribution of the heat flux across the heater at $t^* = 0.61$

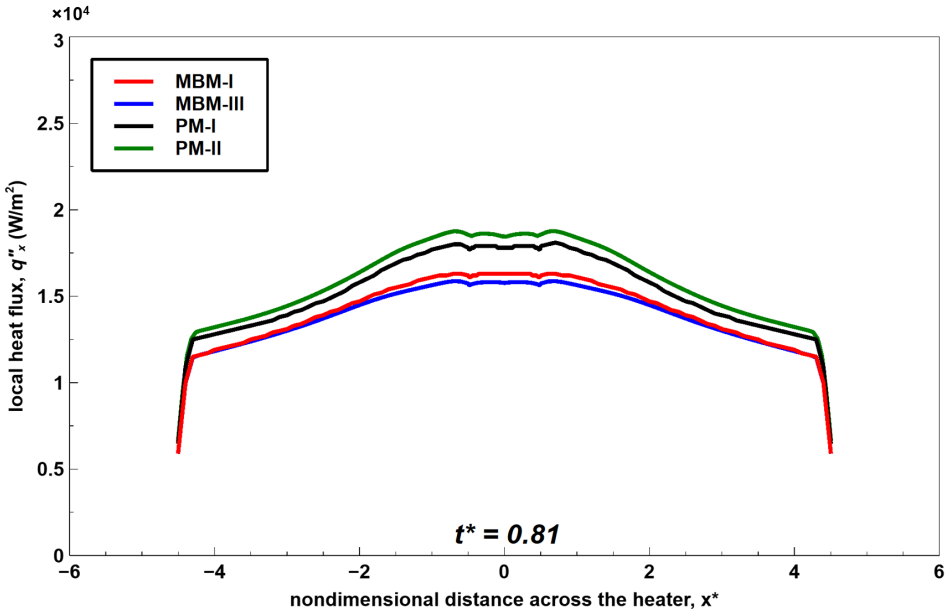

Figure 3.12: Distribution of the heat flux across the heater at $t^* = 0.81$

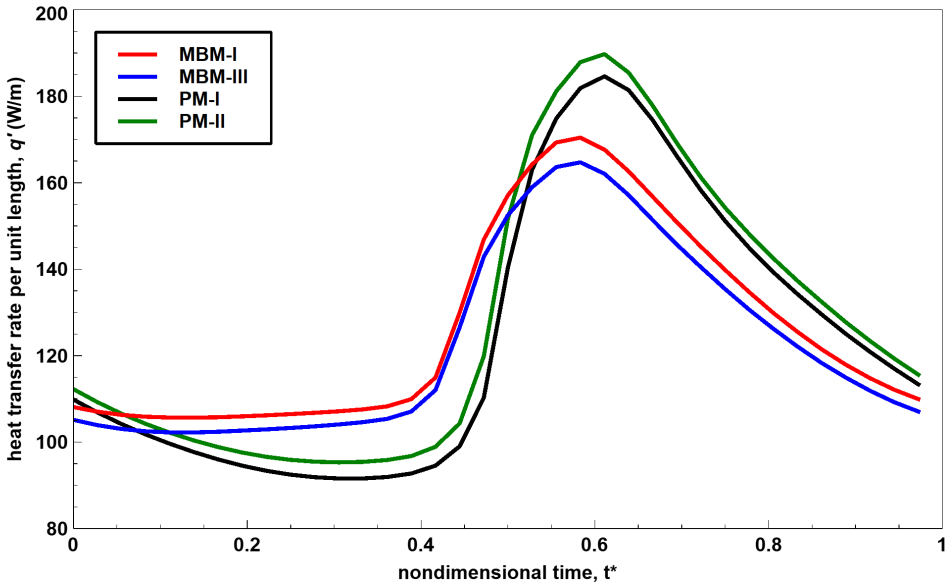

Figure 3.13: Heat transfer rate per unit length of the cases with the same ejected mass flow rate

3.3.2 Discussion of the Models with the Same Nondimensional Stroke Length

MBM-II is built with a 10.67 mm moving wall width to match the stroke length of PM-I. The work input of MBM-II is lower than MBM-I by 29% and lower than PM-I by 4%. In contrast, the ejected mass flow rate of PM-I and MBM-I are 12% larger than MBM-II. The difference in the work input between MBM-I and MBM-II is caused by the difference in the discharge mass flow rates, as seen in Figure 3.14. The result shows the impact of discharge mass flow rates on the work input. Furthermore, the result also reveals that the higher work input of PM-I due to the higher ejected mass flow rate must have been compensated with the aforementioned advantageous characteristic, i.e., the unidirectional flow. Figure 3.18 compares the heat transfer rate per unit length between MBM-II and PM-I, which have the same stroke length. Even though MBM-II features the same characteristics as other MBMs, due to the significant difference in the ejected mass flow rates (compared to PMs), it falls behind PMs in heat removal throughout the cycle. $\overline{Nu}$, defined in equation (2.17), is generally lower for PMs, since the confined space domain has lower temperature distributions. This characteristic further is proven with the help of the comparative temperature contours for MBM-I and PM-I without cross flow given in subsection

3.3.4.

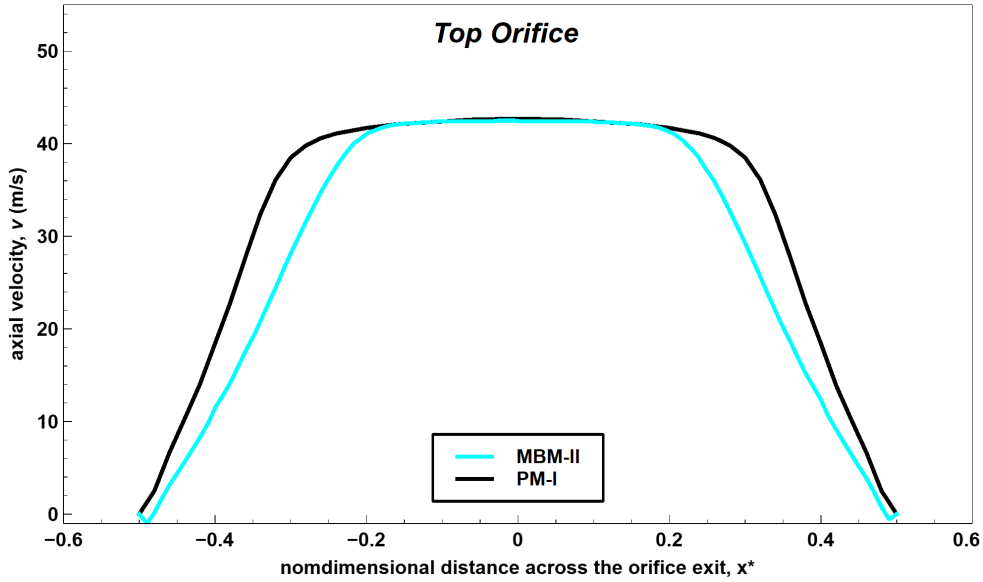

Figure 3.14: Orifice exit axial velocities of the cases with the same nondimensional stroke length at t*=0.33

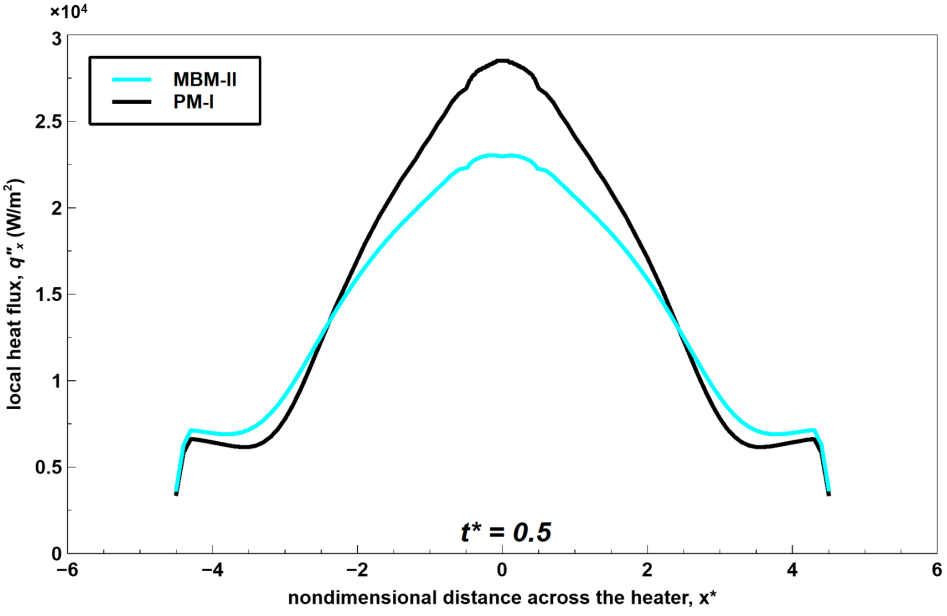

Figure 3.15: Distribution of the heat flux across the heater at $t^* = 0.5$

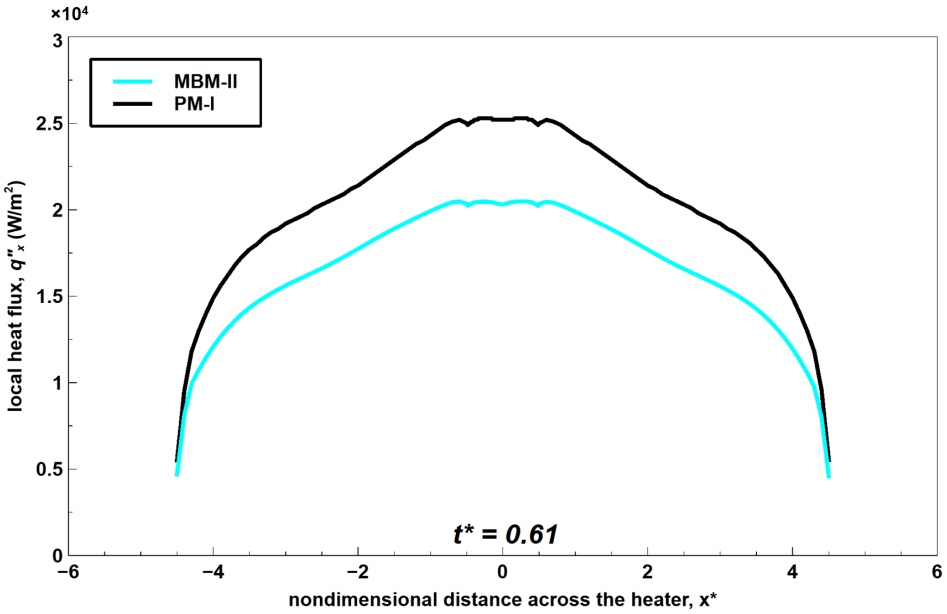

Figure 3.16: Distribution of the heat flux across the heater at $t^* = 0.61$

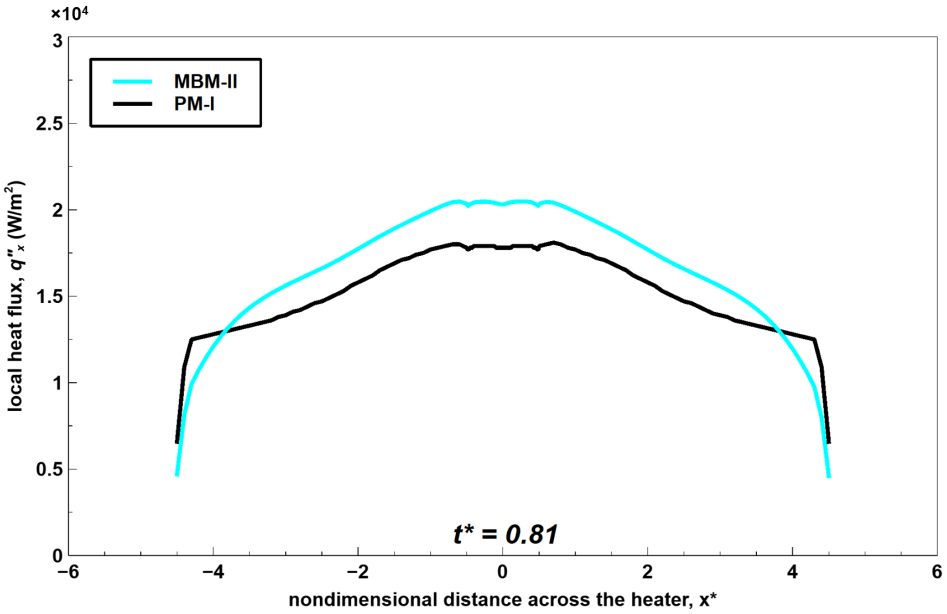

Figure 3.17: Distribution of the heat flux across the heater at $t^* = 0.81$

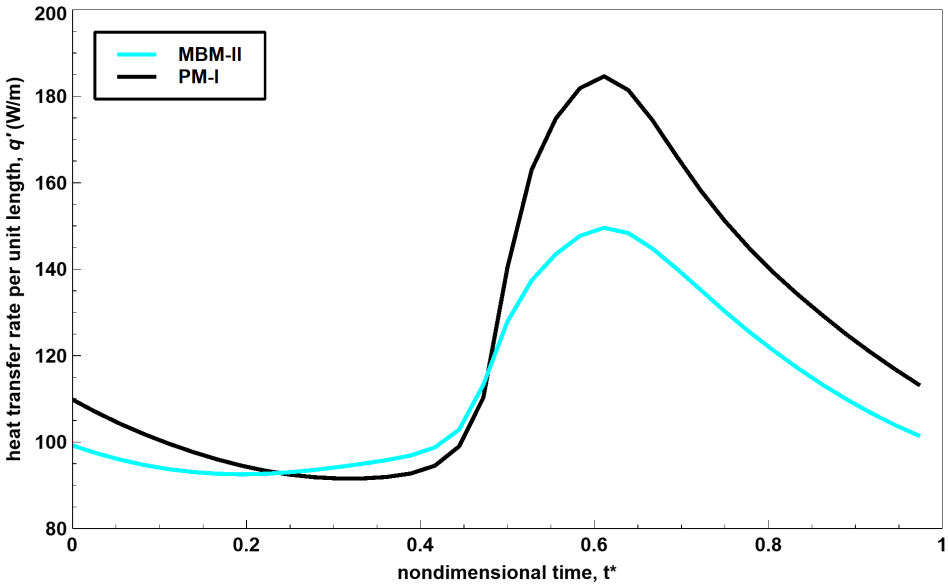

Figure 3.18: Heat transfer rate per unit length of the cases with the same nondimensional stroke length

3.3.3 Further Discussion

A detailed inspection of the axial velocities in the orifices of PM-I, Figure C.2, provides information about the cause of the significant difference in the stroke length. The boundary condition for the opening of the bottom orifice is the pressure inlet, resulting in a dispersed velocity profile at the exit of the top orifice C.2(a) since the flow is still developing. This behavior causes PM-I model to have a lower stroke length since it directly affects the centerline velocity at the exit of the top orifice. For better representation of the flow characterization and the stroke length calculations, a sufficiently large distance between the pressure inlet and the adjacent domain of the bottom must be implemented. While the presence of the far-field would slightly increase the work input, it would also increase the stroke length since the flow would be less dispersed, making the centerline velocity higher. The effect of the far-field is left out as future work. The flow characteristics of PM-I is given in Appendix C in order not to disturb the text flow.

The only parameter that cannot be kept constant is the cavity aspect ratio; therefore, a model with larger bottom wall width, PM-II, is studied. Results show less than 2%

difference compared to PM-I, proving that the cavity aspect ratio's effect is almost negligible.

3.3.4 Modified Base Model and Proposed Model with Cross Flow in a Confined Space

Parametric studies are conducted to observe the cross flow effect of the proposed model in a confined space.

There are six different models presented in the previous sections. Each model has pros and cons. In order to observe the effect of the proposed design, PM-I is selected. During the comparison, discharge mass flow rates are kept the same; therefore, MBM-I is selected as the base model. The cavity ratios of the compared models are not the same, but the effect of the cavity ratios is neglected as it does not affect the parameters more than 2% (between PM-I and PM-II), as seen in Table 3.2. Furthermore, keeping the discharged mass flow rate the same allows the effect of stroke length on distinct blowing ratios to be observed. During the parametric study, the $\bar{v}_{cl}$ remains the same while the cross flow magnitude changes; thus, C_b of MBM-I is 33, 16.5, and 11 whereas C_b of PM-I is 29.5, 14.75, and 9.83.

Figures 3.23 to 3.37 show time-lapsed velocity and temperature contours within the solution domain and shear stress profile at the top wall of the confined space. The operation conditions are; 1 mm diaphragm amplitude, varying microchannel inlet velocity from 0 m/s to 1.5 m/s with 0.5 m/s increments, and diaphragm frequency of 500 Hz. Each case is divided into five-time steps to observe the stagnation phenomena and the effect of the cross flow onto the pulsating jet flow characteristic in a confined space.

Figures 3.19, 3.24, 3.29, and 3.34 examine the discharge phase. Discharged high-velocity fluid jet tries to penetrate the microchannel flow and disturbs the boundary layer on the top wall depending on the blowing ratios. As the blowing ratios decrease, the microchannel's drag pushes the jet flow in the flow direction, and cross flow hinders the boundary layer's penetration, diminishing the advantageous thermal characteristics. At $t^* = 0.33$, the impinging flow for both cases reaches closer to

the confined space's top. This behavior is due to the fact that, in MBM-I case, the velocity profile leaving the orifice is sharper and more parabolic compared to PM-I, which is discussed previously. Figure 3.24(c) presents the wall shear stress along the confined space's top for MBM-I and PM-I. MBM-I has a blowing ratio of 33, while the value is 29.5 for PM-I. It can be observed that the magnitude of wall shear stress is a function of the blowing ratio by comparing Figures from 3.23(c) to 3.37(c). A more considerable wall shear stress means that the velocity gradient at the wall is larger, thus is an implication of better heat transfer due to boundary layer disturbance. Additionally, the stagnation phenomenon is observed between the global minimum and global maximum value of the shear stress by comparing Figures 3.24 (a), (b), and (c). The stagnation region is wider for PM-I, which resembles the wider impingement velocity profile. In PM-I case, the stagnation region nearly encapsulates the heater after $x/d = 0$, which suggests a larger heat transfer area with lower flow temperatures around it. Therefore, a lower average convective heat transfer coefficient at the heater is expected for PM-I, while MBM-I model has larger peaks. The main advantage of the proposed model is the elimination of recirculation flows with high temperatures, thus resulting in lower flow temperatures in the confined space domain.

Figures 3.20, 3.25, 3.30, and 3.35 investigate the end of the discharge phase. At $t^* = 0.5$, the diaphragm reaches the peak displacement. While the jet flow has reached the top wall for MBM-I with $C_b = 33$, MBM-I and PM-I without cross flow. The penetration ability of the jet flow is inhibited for all the other configurations with the cross flow, reducing the local heat transfer coefficient due to the lower boundary layer disturbance. As the cross flow magnitude increases, the peak shear stress of the top confined space wall for MBM-I shifts from $t^* = 0.5$ to later stages. The reason is the fact that the impinging jet and the wall jet effects slowly fade away, and are replaced by shear caused by vortexes as the cross flow gets stronger.

MBM-I design inhales the fluid from the confined space, whereas PM-I draws the uncirculated fluid from the bottom orifice into the cavity. Meanwhile, the vortexes are pushed in the downstream direction by the convection effect of the cross flow at $t^* = 0.67$. MBM-I intake cancel out some of the convection effects of the cross flow, and it decreases the dissipation rate of the vortexes, as observed in Figures 3.21, 3.26, 3.31, and 3.36. This characteristic justifies the difference in the shear stresses on the

wall between PM-I and MBM-I.

Figures 3.22, 3.27, 3.32, and 3.37 compare the ending of the intake phase. In the absence of the cross flow, MBM-I draws a comparably large amount of fluid from the pressure outlets to fill the cavity, whereas the only form of backflow in PM-I is due to the vortexes. The vortexes in PM-I nearly escape from the pressure outlets and create backflows. If the backflow temperature is higher than the confined space domain's temperature, the backflow is unfavorable for heat removal applications. Therefore, PM-I offers a significant decrease in the temperature in the confined space in the absence of the cross flow.

At the beginning of the new cycle, i.e., $t^* = 1$, the diaphragm returns to the most stretched position. Figures 3.23, 3.28, 3.33, and 3.38 reveal that at the end of the cycle, vortexes get closer to the right outlet depending on the strength of the cross flow. This behavior results in lower shear stresses throughout the confined space wall.

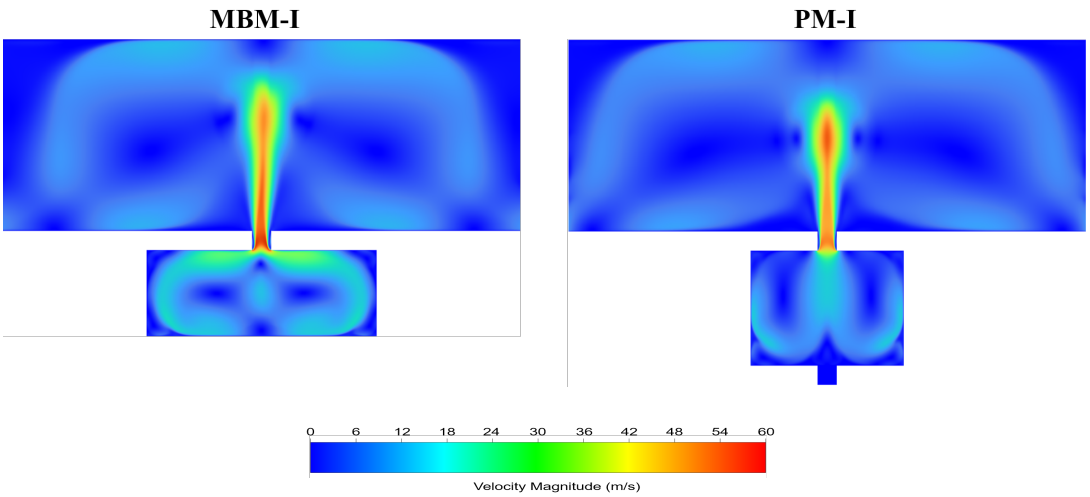

(a) Velocity contours, MBM-I and PM-I

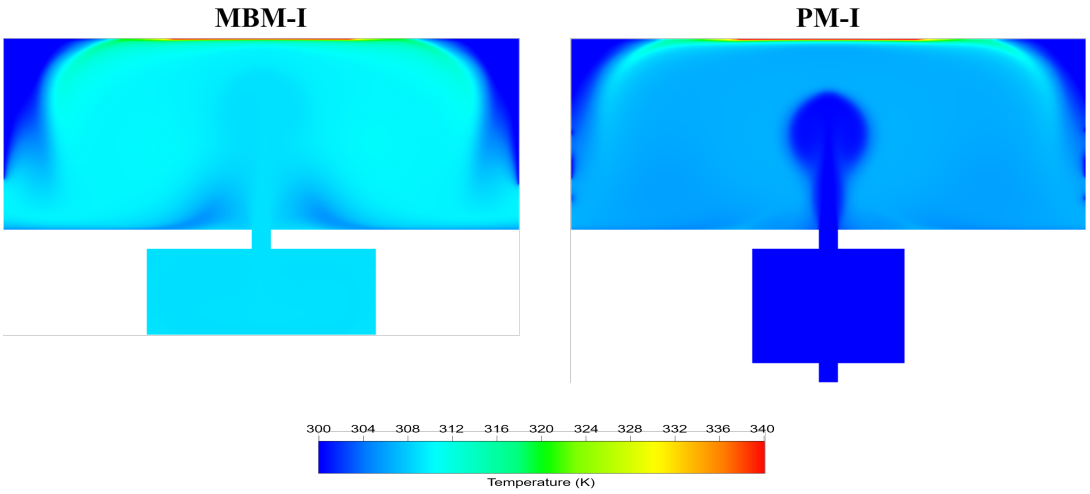

(b) Temperature contours, MBM-I and PM-I

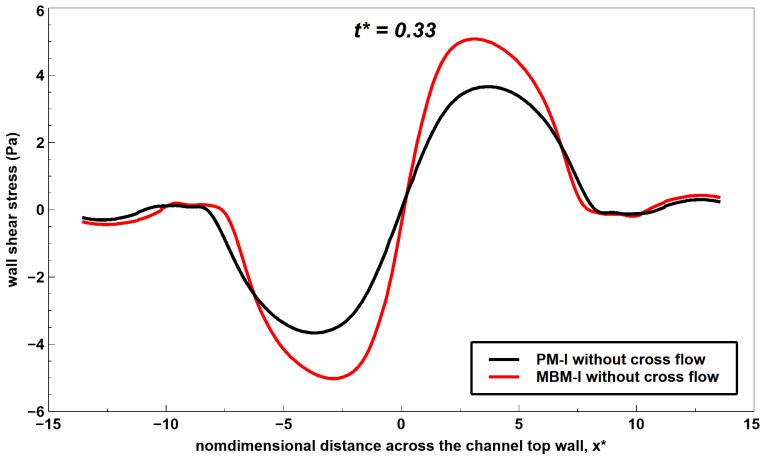

(c) Wall shear stress at the top confined space wall, MBM-I vs PM-I

Figure 3.19: MBM-I vs PM-I without cross flow at $t^* = 0.33$

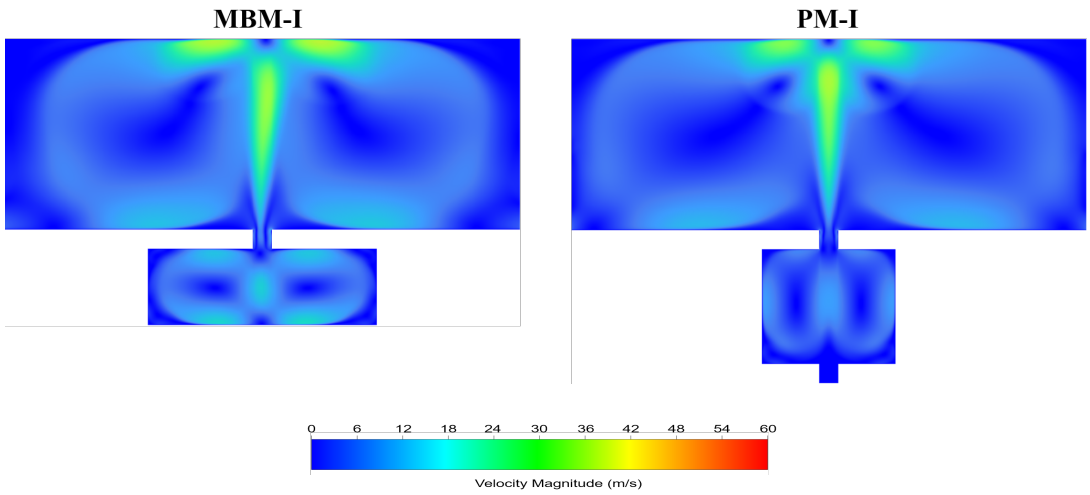

(a) Velocity contours, MBM-I and PM-I

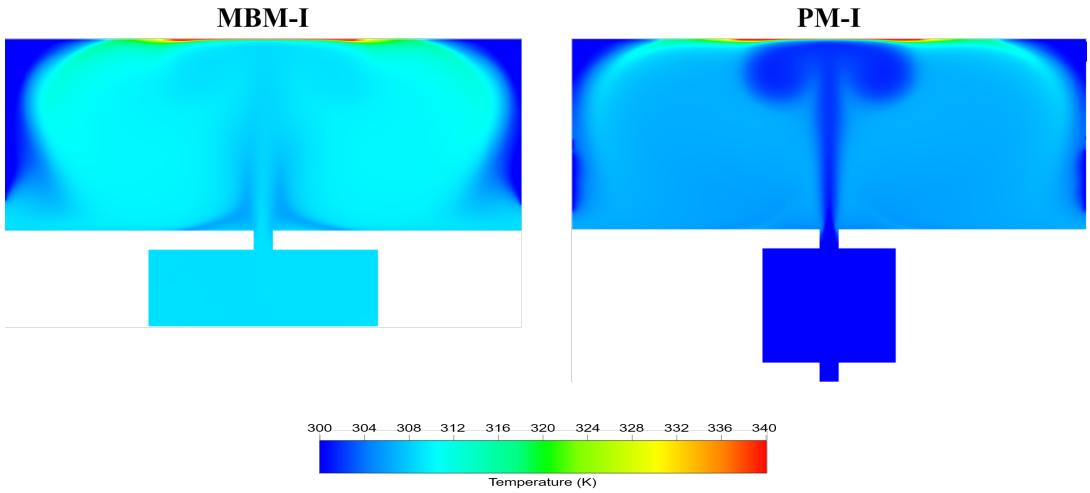

(b) Temperature contours, MBM-I and PM-I

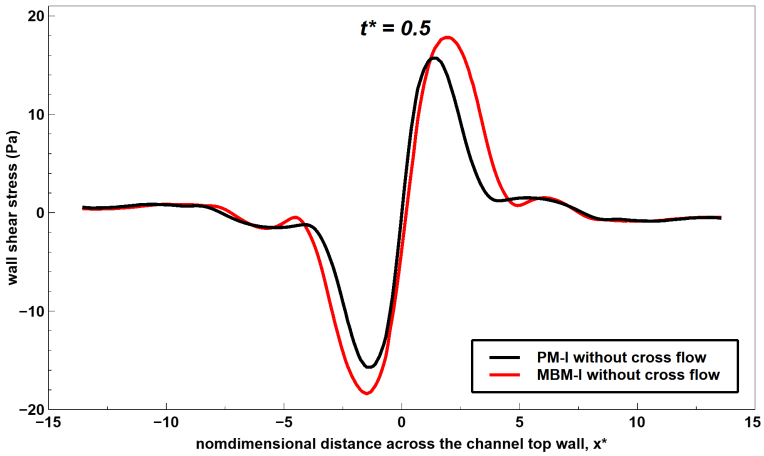

(c) Wall shear stress at the top confined space wall, MBM-I vs PM-I

Figure 3.20: MBM-I vs PM-I without cross flow at $t^* = 0.5$

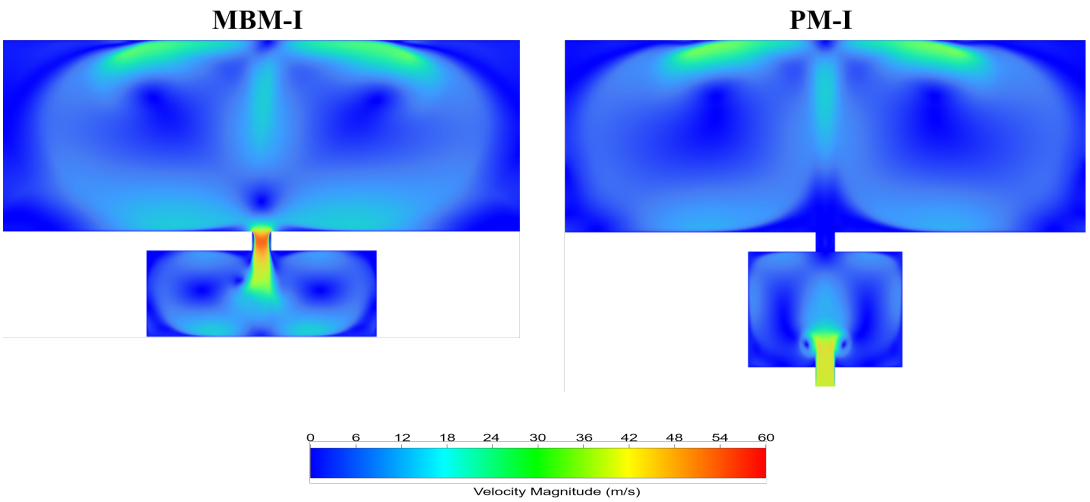

(a) Velocity contours, MBM-I and PM-I

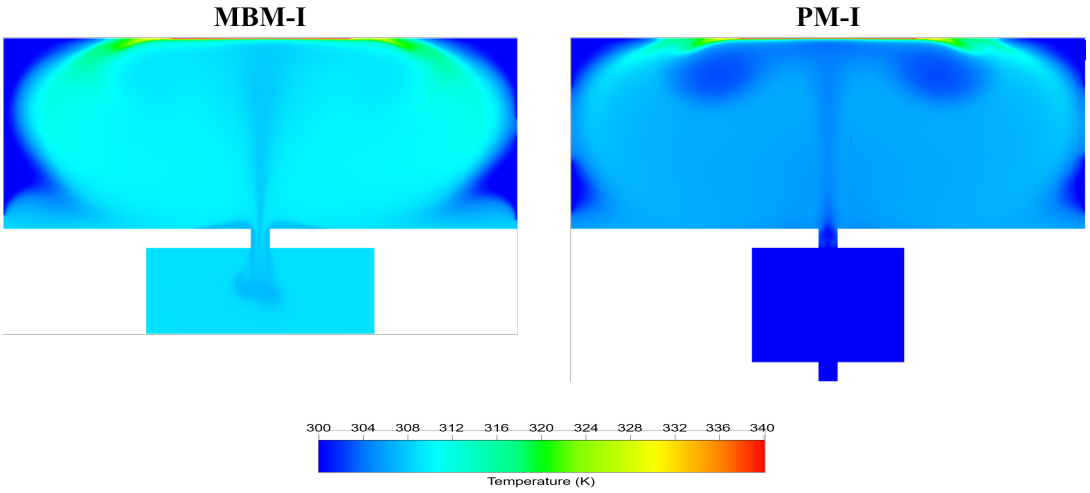

(b) Temperature contours, MBM-I and PM-I

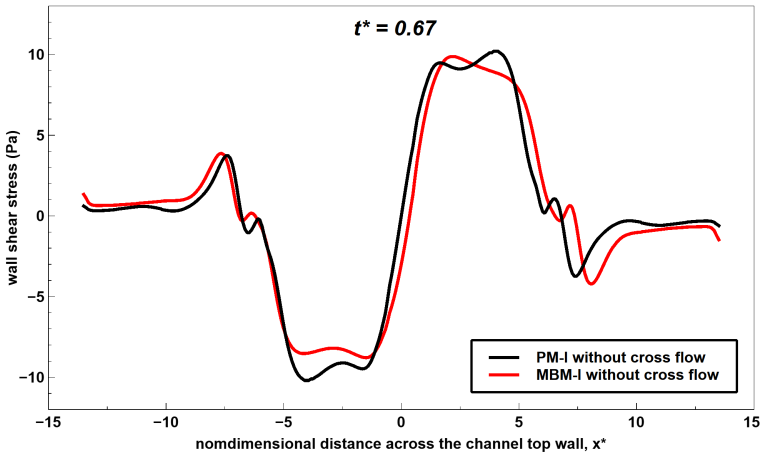

(c) Wall shear stress at the top confined space wall, MBM-I vs PM-I

Figure 3.21: MBM-I vs PM-I without cross flow at $t^* = 0.67$

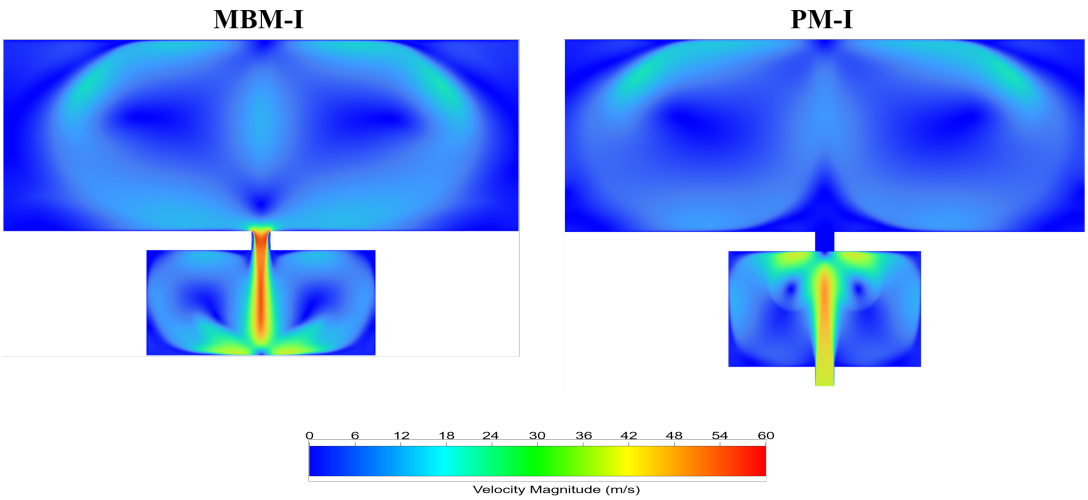

(a) Velocity contours, MBM-I and PM-I

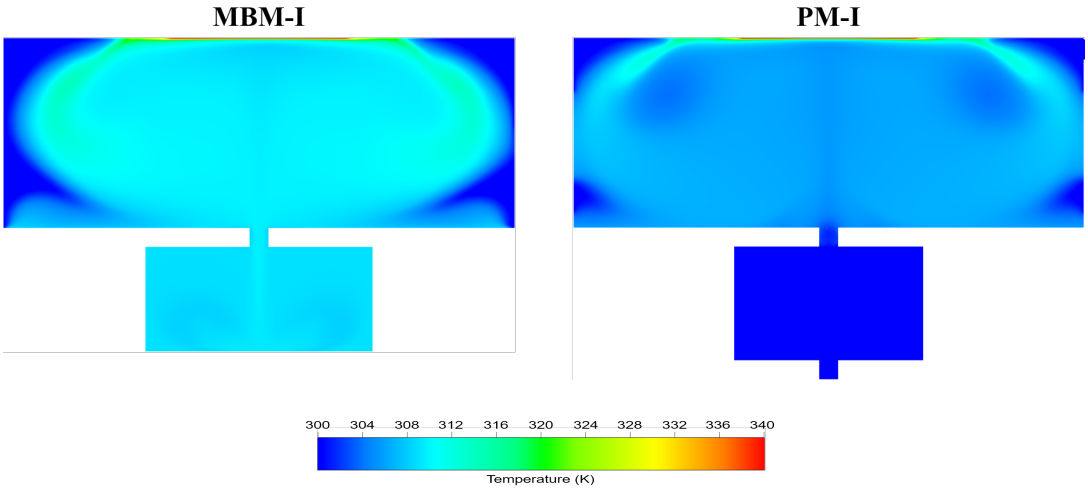

(b) Temperature contours, MBM-I and PM-I

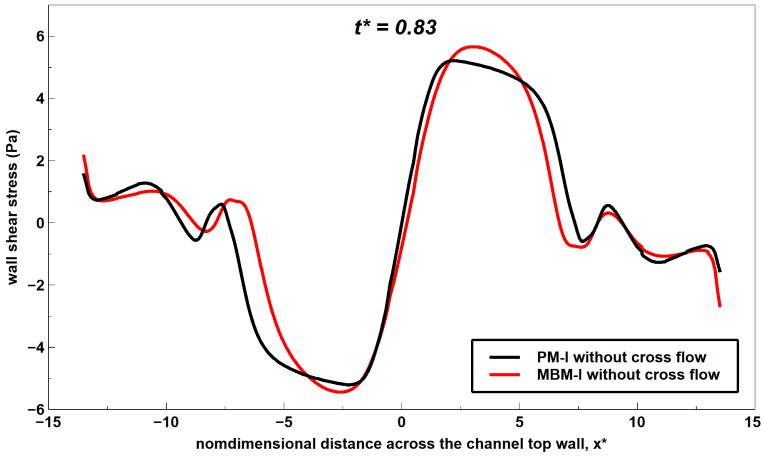

(c) Wall shear stress at the top confined space wall, MBM-I vs PM-I

Figure 3.22: MBM-I vs PM-I without cross flow at $t^* = 0.83$

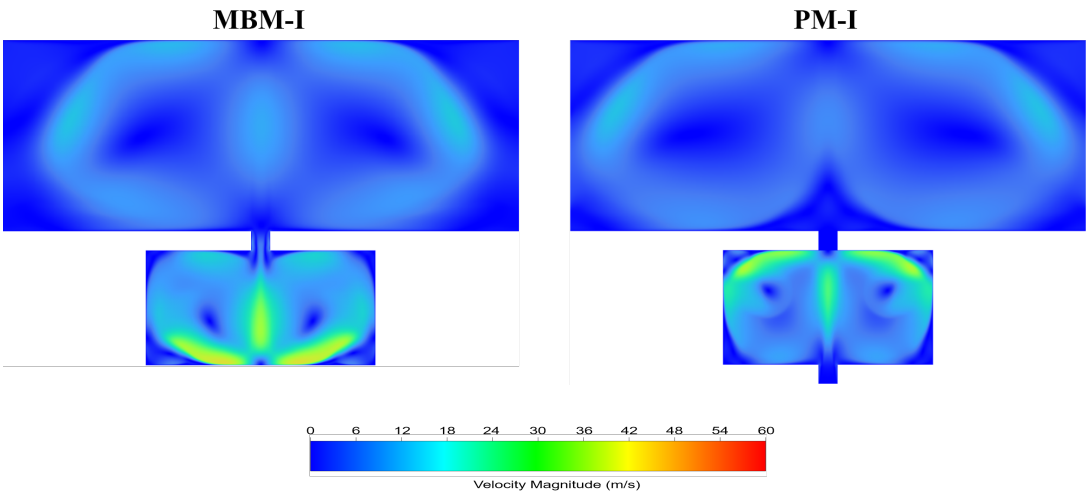

(a) Velocity contours, MBM-I and PM-I

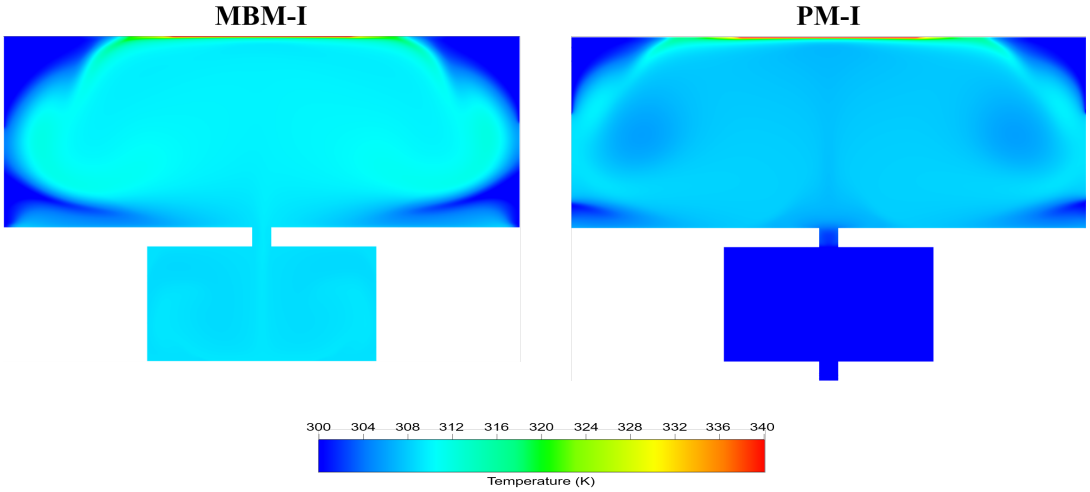

(b) Temperature contours, MBM-I and PM-I

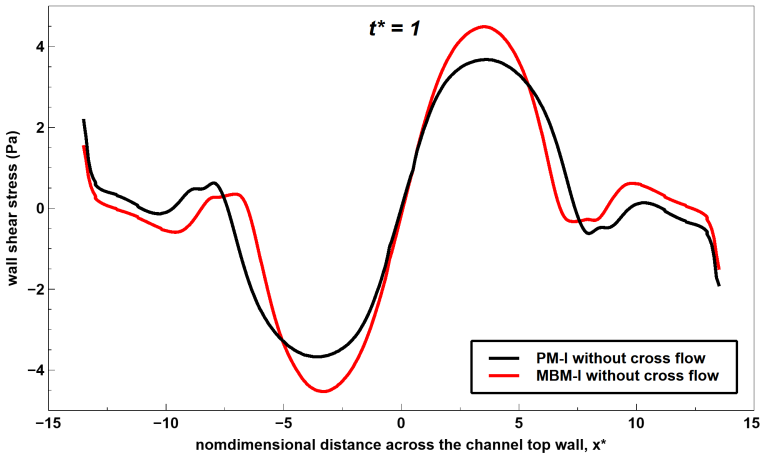

(c) Wall shear stress at the top confined space wall, MBM-I vs PM-I

Figure 3.23: MBM-I vs PM-I without cross flow at $t^* = 1$

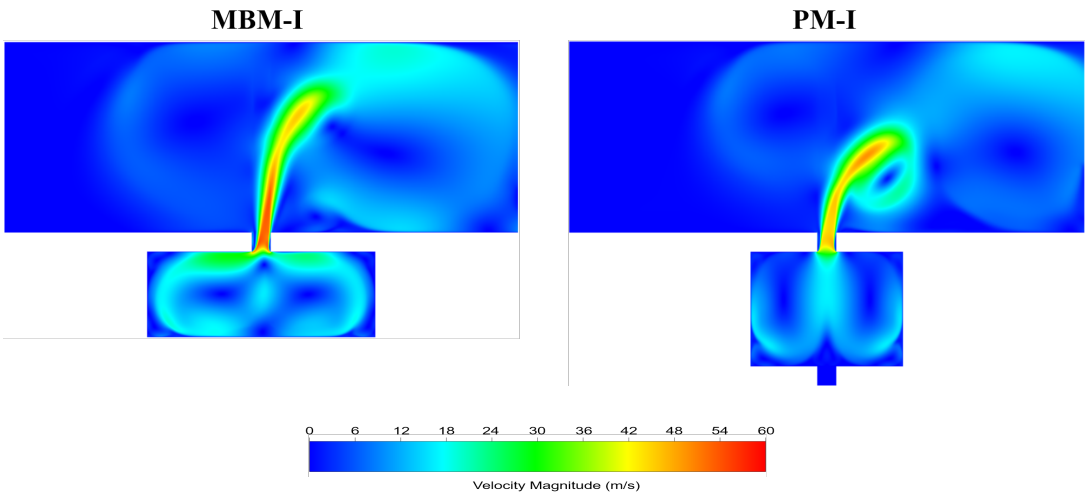

(a) Velocity contours, MBM-I and PM-I

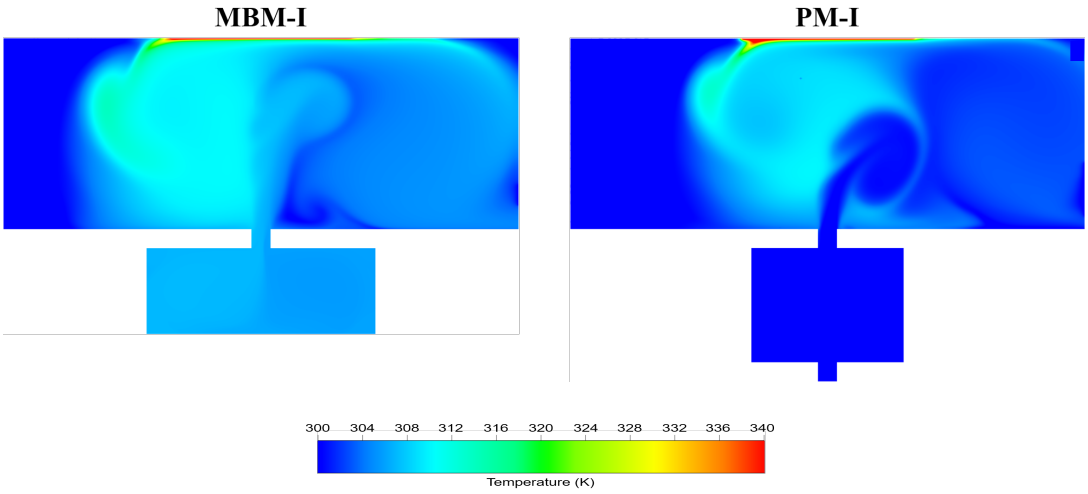

(b) Temperature contours, MBM-I and PM-I

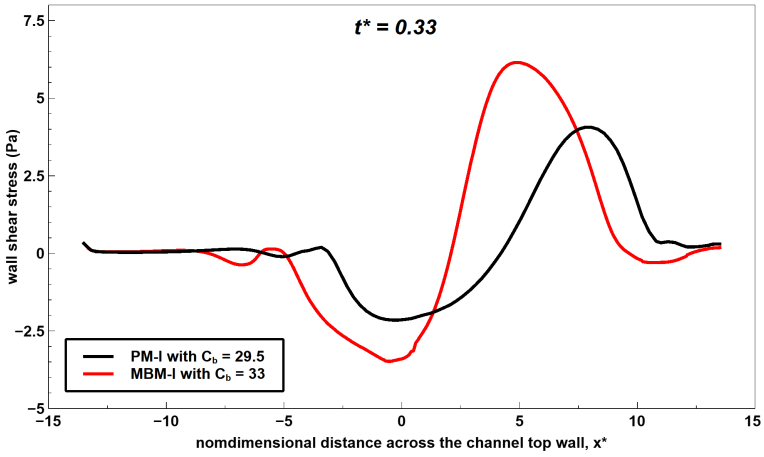

(c) Wall shear stress at the top confined space wall, MBM-I vs PM-I

Figure 3.24: MBM-I with $C_b = 33$ vs PM-I with $C_b = 29.5$ at $t^* = 0.33$

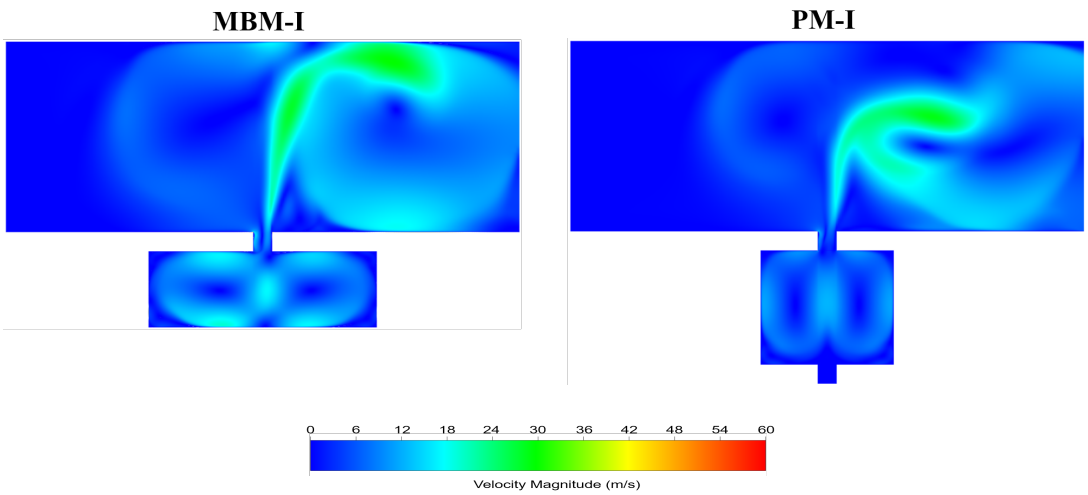

(a) Velocity contours, MBM-I and PM-I

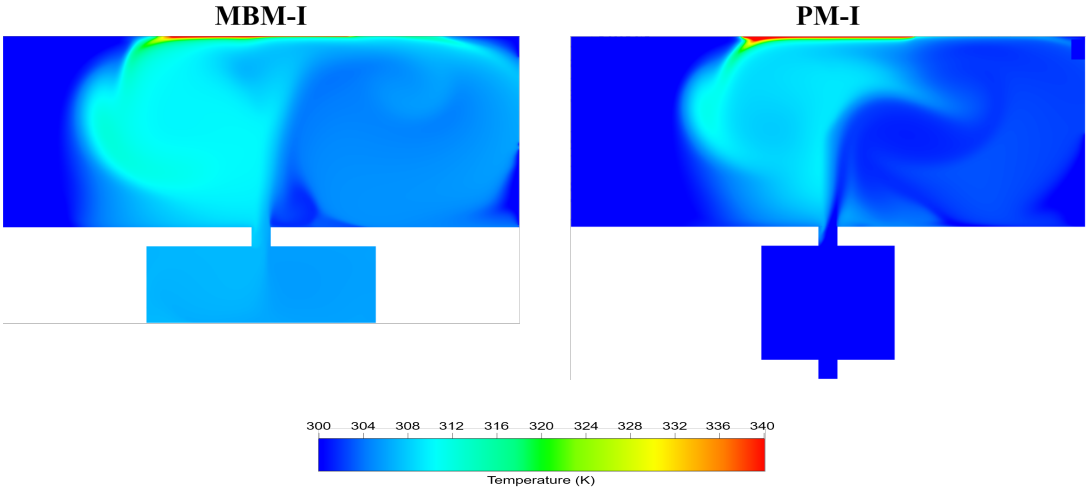

(b) Temperature contours, MBM-I and PM-I

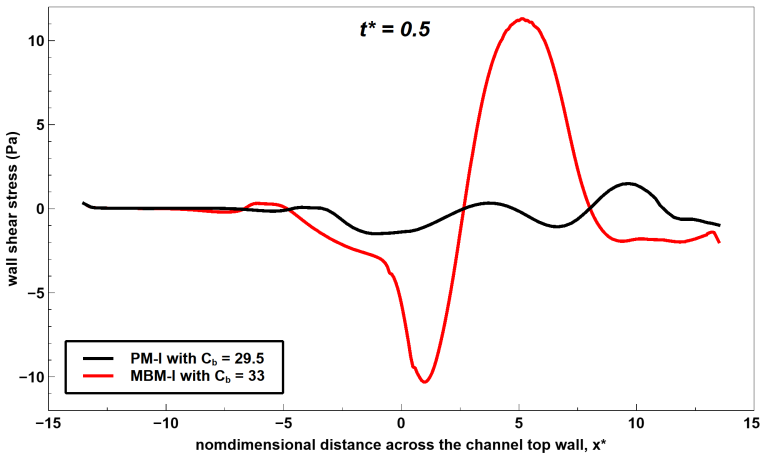

(c) Wall shear stress at the top confined space wall, MBM-I vs PM-I

Figure 3.25: MBM-I with $C_b = 33$ vs PM-I with $C_b = 29.5$ at $t^* = 0.5$

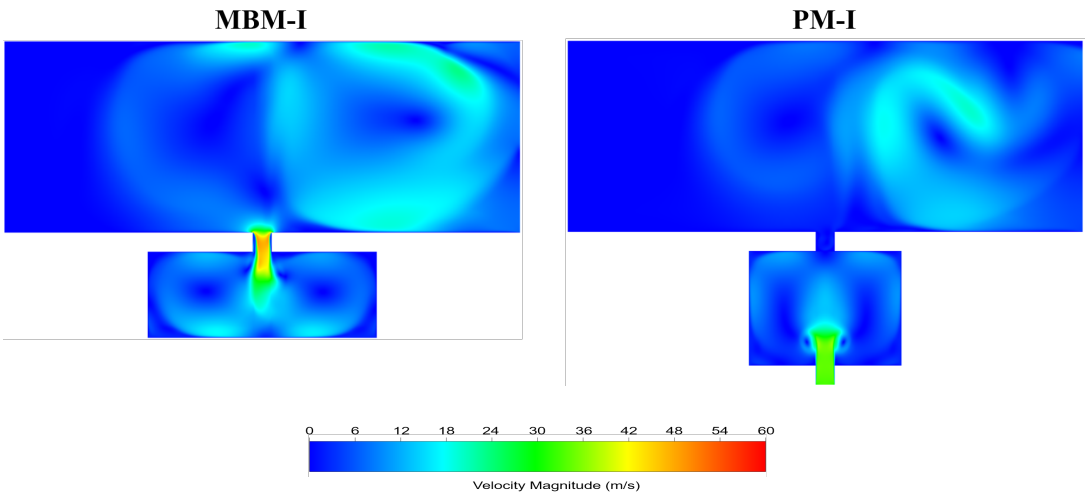

(a) Velocity contours, MBM-I and PM-I

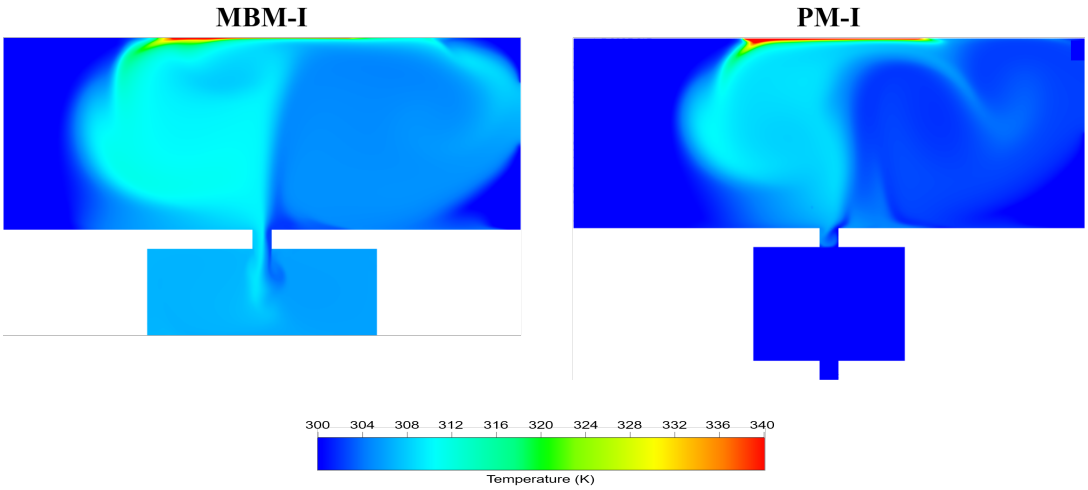

(b) Temperature contours, MBM-I and PM-I

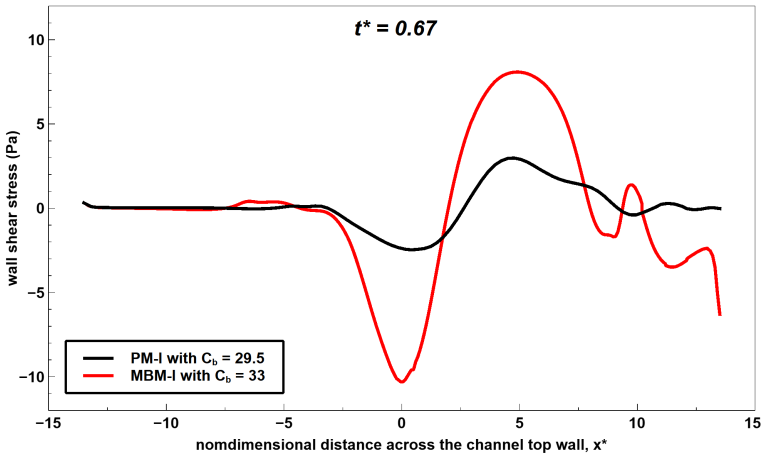

(c) Wall shear stress at the top confined space wall, MBM-I vs PM-I

Figure 3.26: MBM-I with $C_b = 33$ vs PM-I with $C_b = 29.5$ at $t^* = 0.67$

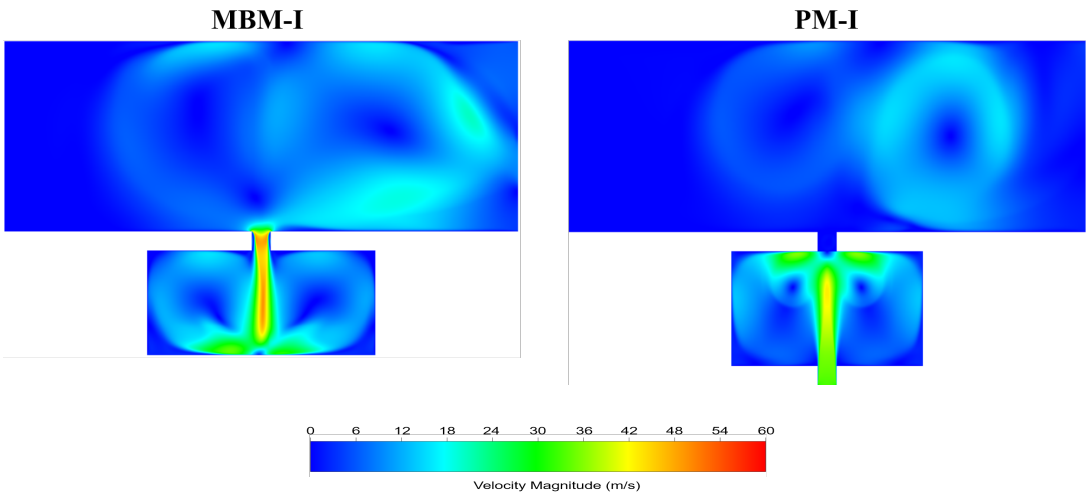

(a) Velocity contours, MBM-I and PM-I

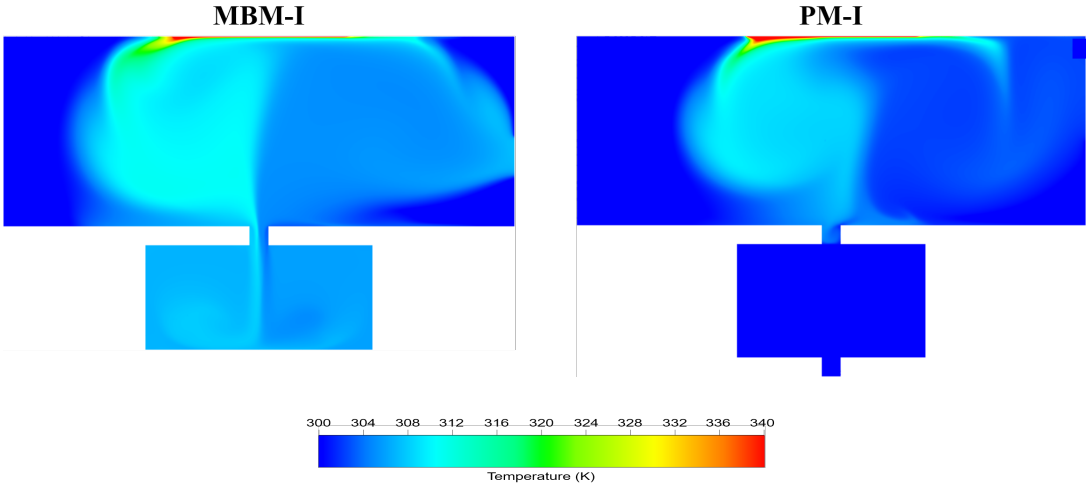

(b) Temperature contours, MBM-I and PM-I

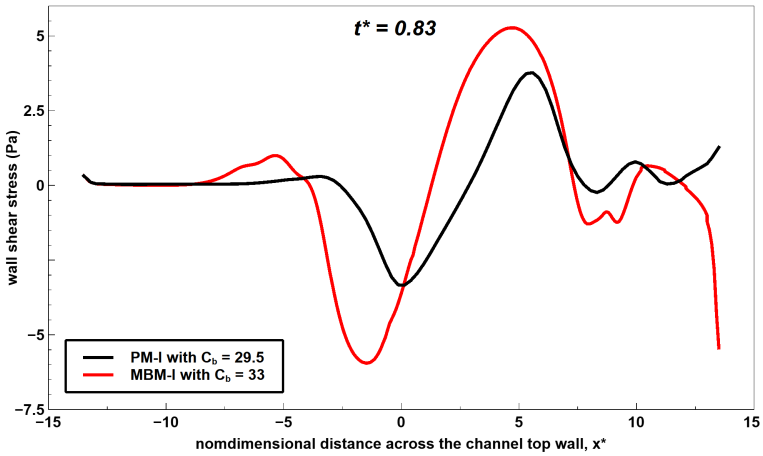

(c) Wall shear stress at the top confined space wall, MBM-I vs PM-I

Figure 3.27: MBM-I with $C_b = 33$ vs PM-I with $C_b = 29.5$ at $t^* = 0.83$

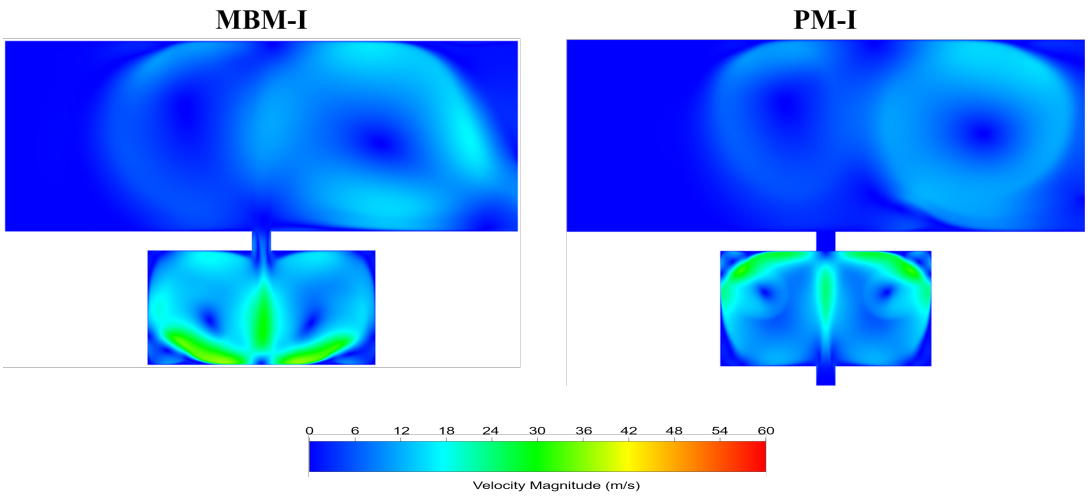

(a) Velocity contours, MBM-I and PM-I

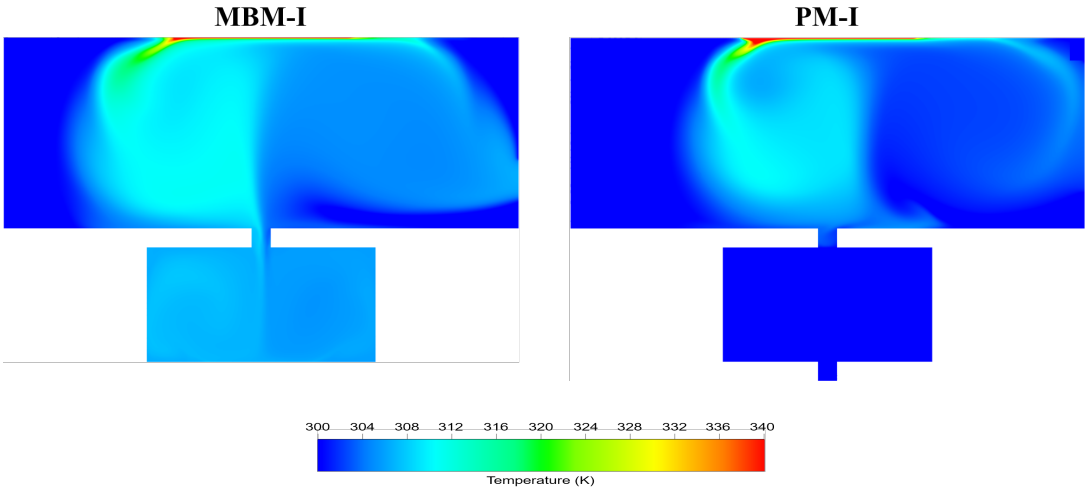

(b) Temperature contours, MBM-I and PM-I

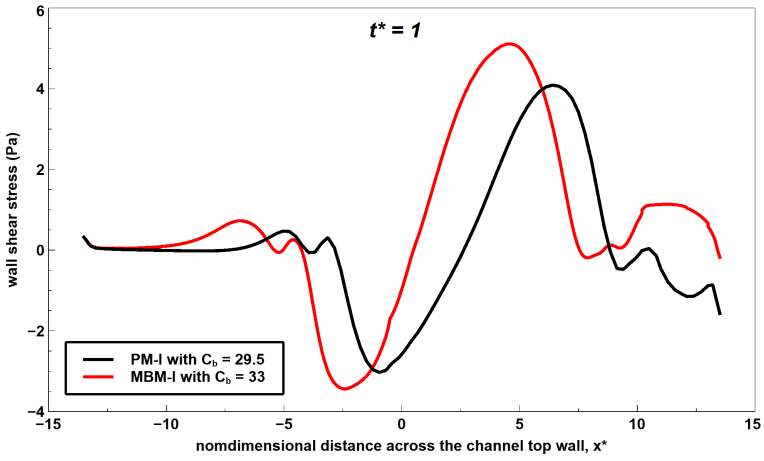

(c) Wall shear stress at the top confined space wall, MBM-I vs PM-I

Figure 3.28: MBM-I with $C_b = 33$ vs PM-I with $C_b = 29.5$ at $t^* = 1$

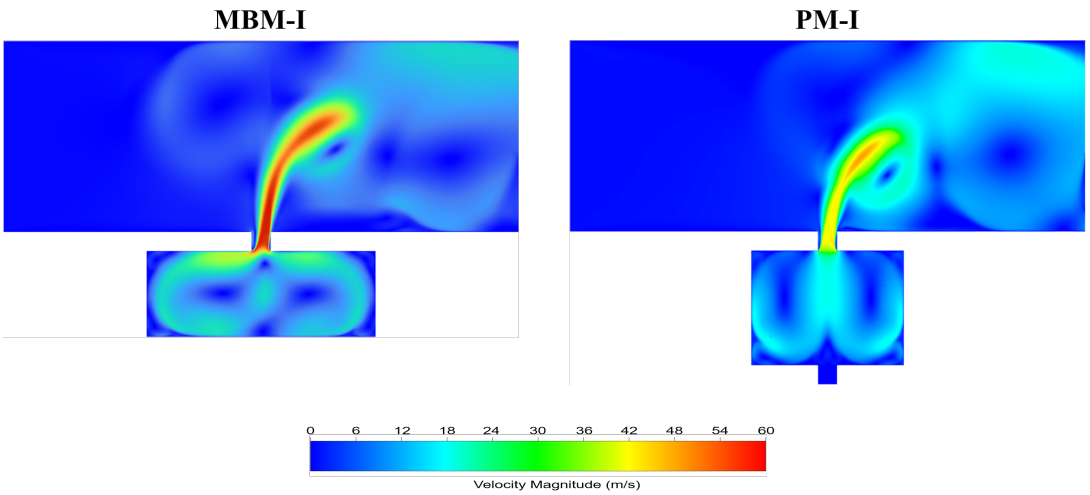

(a) Velocity contours, MBM-I and PM-I

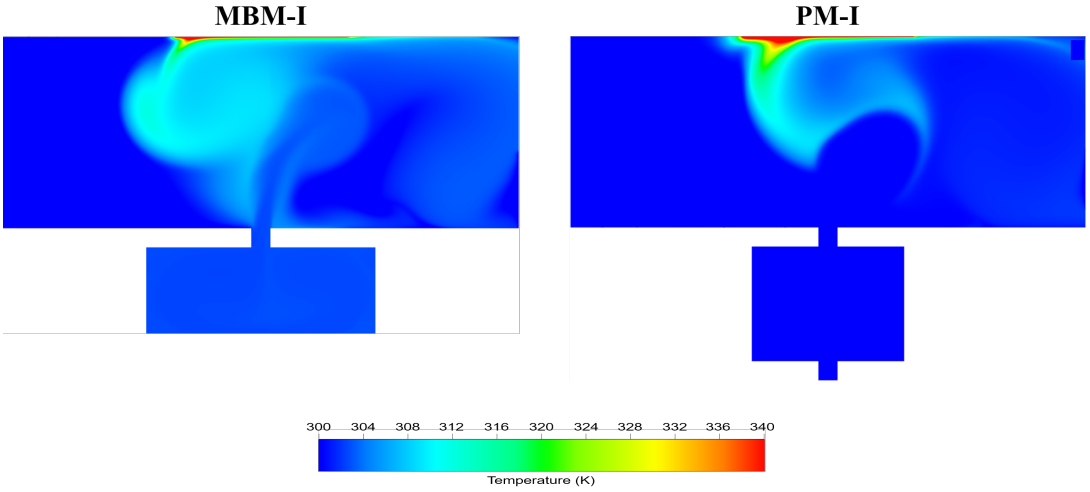

(b) Temperature contours, MBM-I and PM-I

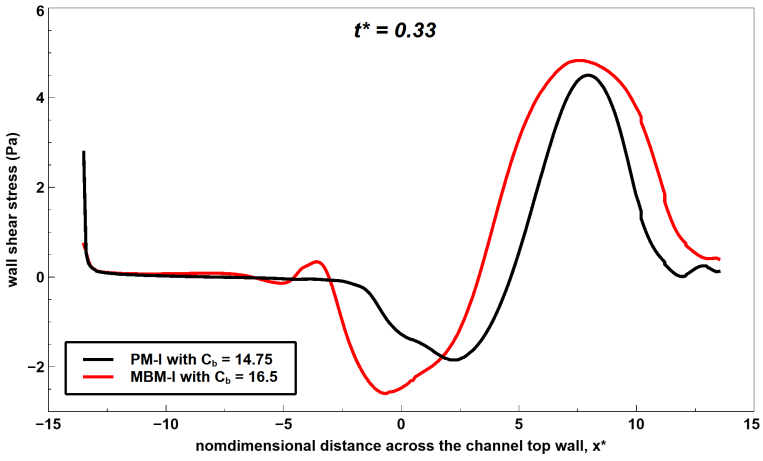

(c) Wall shear stress at the top confined space wall, MBM-I vs PM-I

Figure 3.29: MBM-I with $C_b = 16.5$ vs PM-I with $C_b = 14.75$ at $t^* = 0.33$

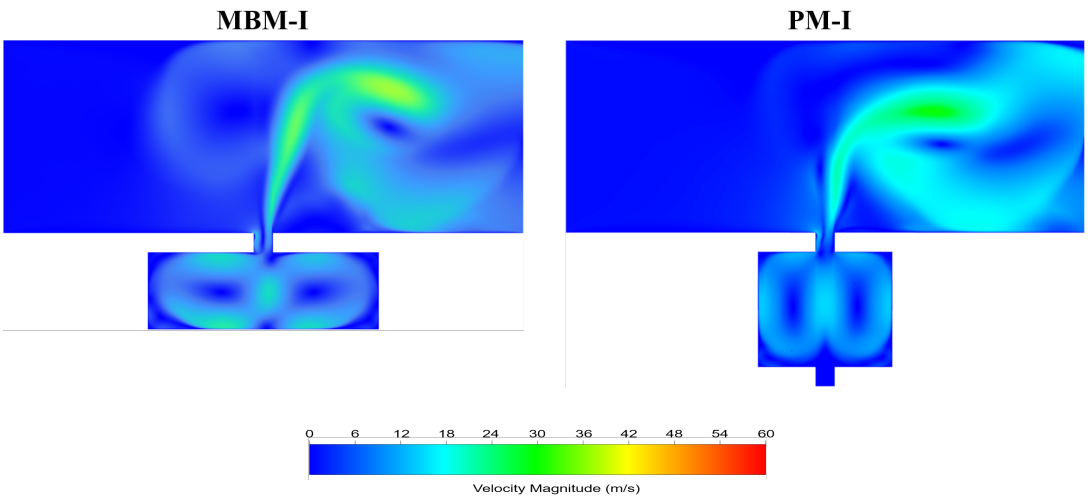

(a) Velocity contours, MBM-I and PM-I

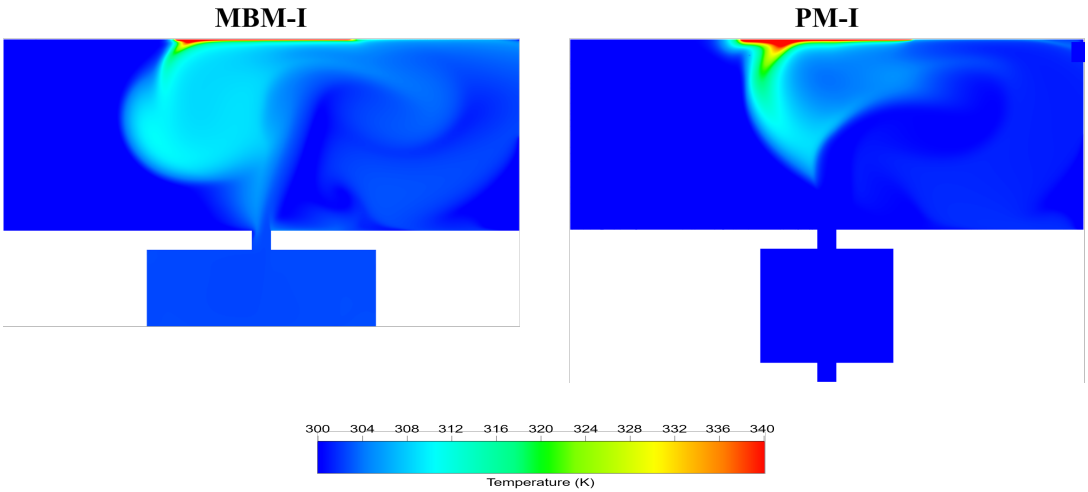

(b) Temperature contours, MBM-I and PM-I

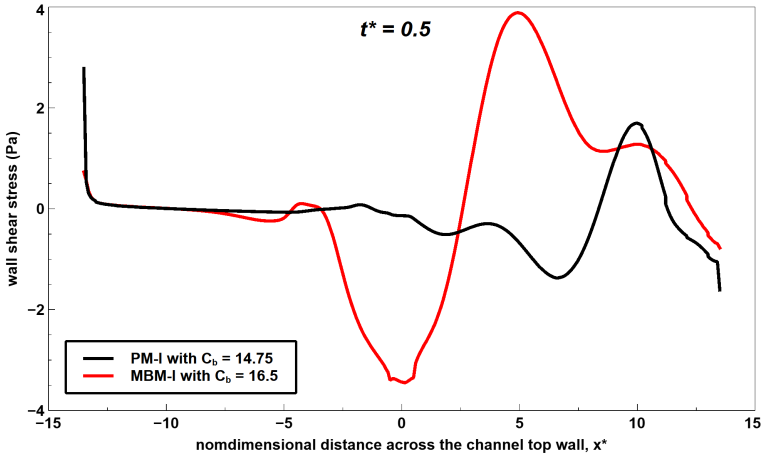

(c) Wall shear stress at the top confined space wall, MBM-I vs PM-I

Figure 3.30: MBM-I with $C_b = 16.5$ vs PM-I with $C_b = 14.75$ at $t^* = 0.5$

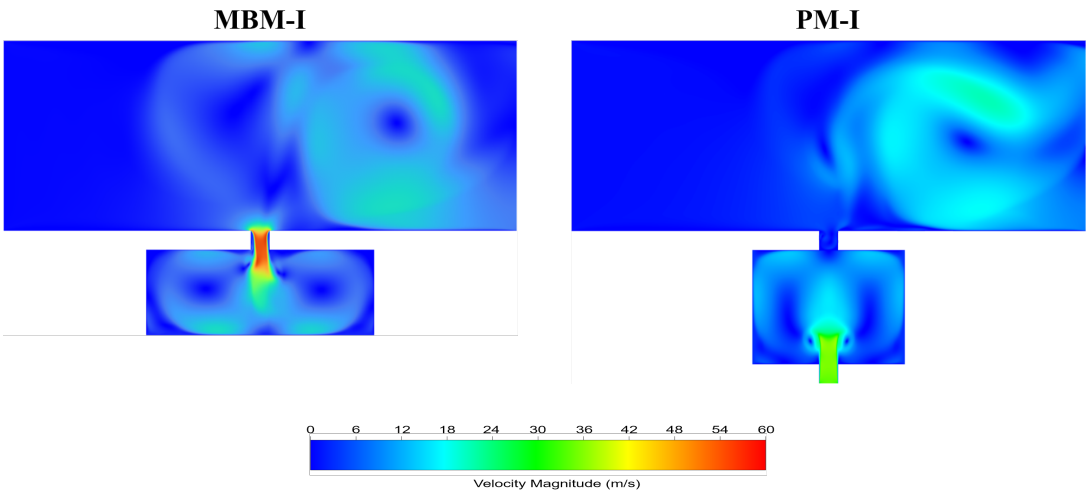

(a) Velocity contours, MBM-I and PM-I

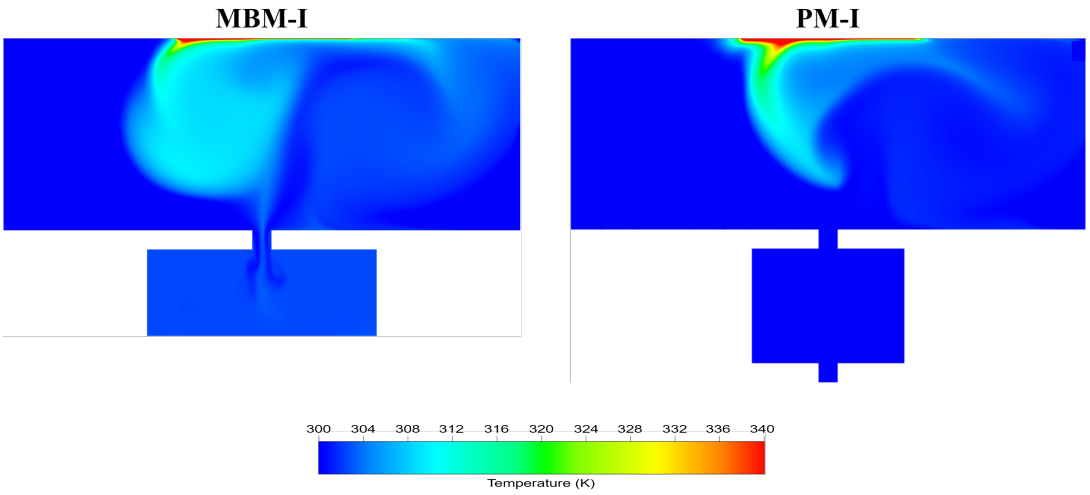

(b) Temperature contours, MBM-I and PM-I

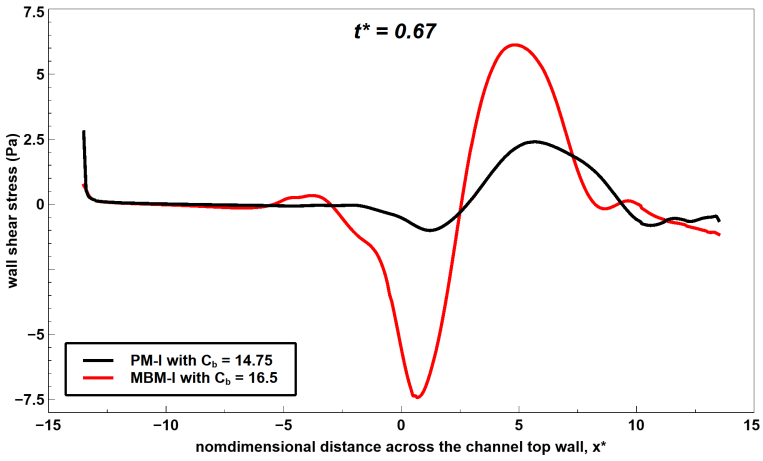

(c) Wall shear stress at the top confined space wall, MBM-I vs PM-I

Figure 3.31: MBM-I with $C_b = 16.5$ vs PM-I with $C_b = 14.75$ at $t^* = 0.67$

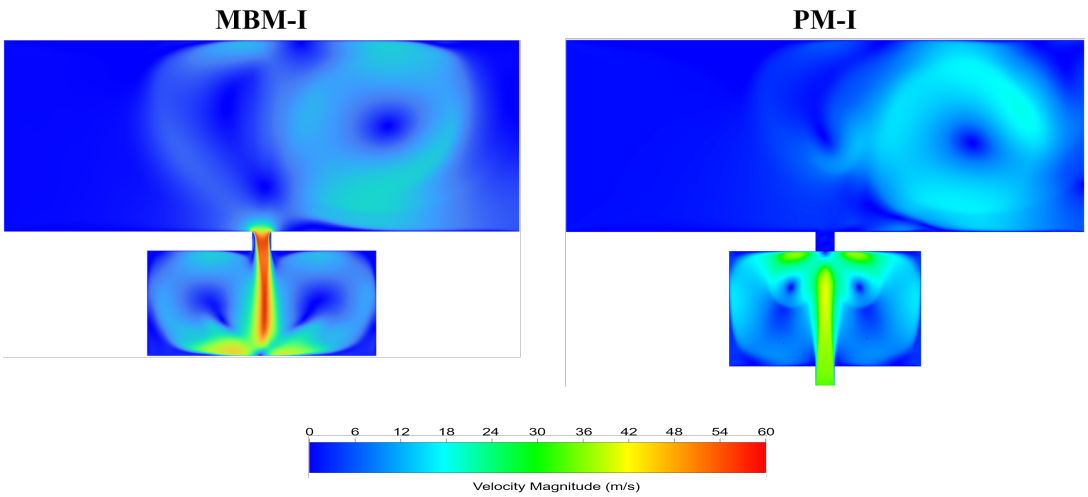

(a) Velocity contours, MBM-I and PM-I

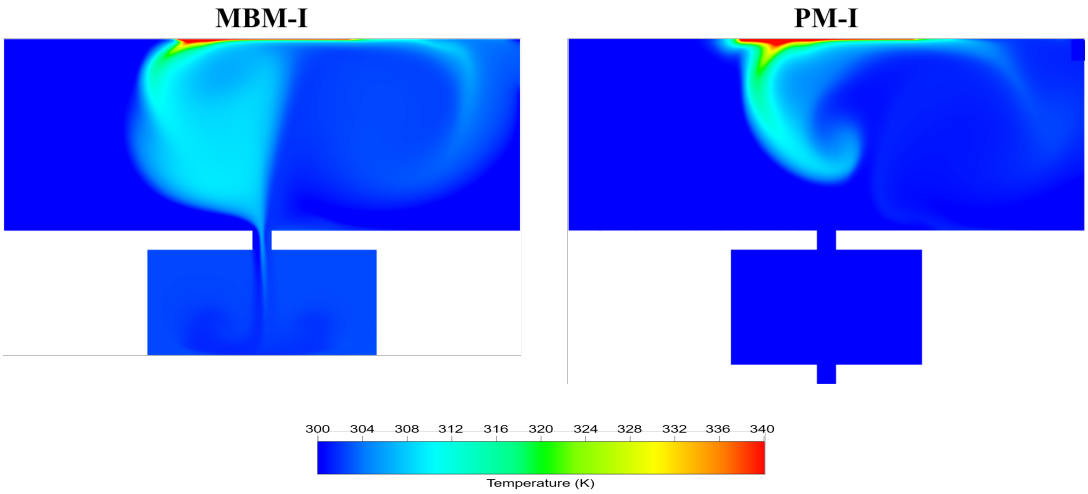

(b) Temperature contours, MBM-I and PM-I

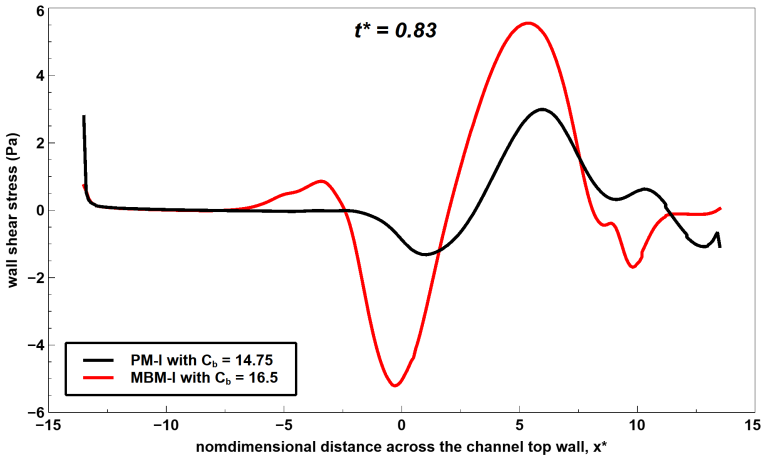

(c) Wall shear stress at the top confined space wall, MBM-I vs PM-I

Figure 3.32: MBM-I with $C_b = 16.5$ vs PM-I with $C_b = 14.75$ at $t^* = 0.83$

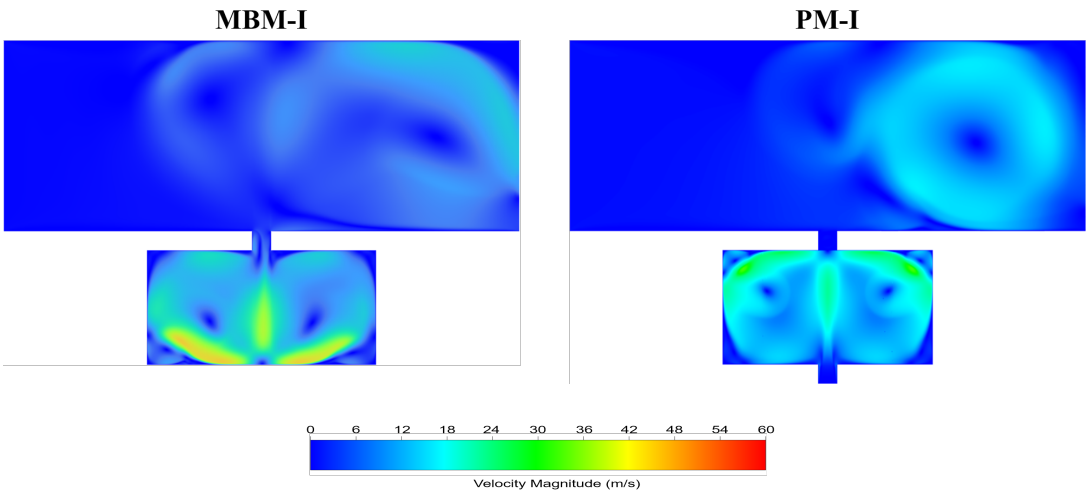

(a) Velocity contours, MBM-I and PM-I

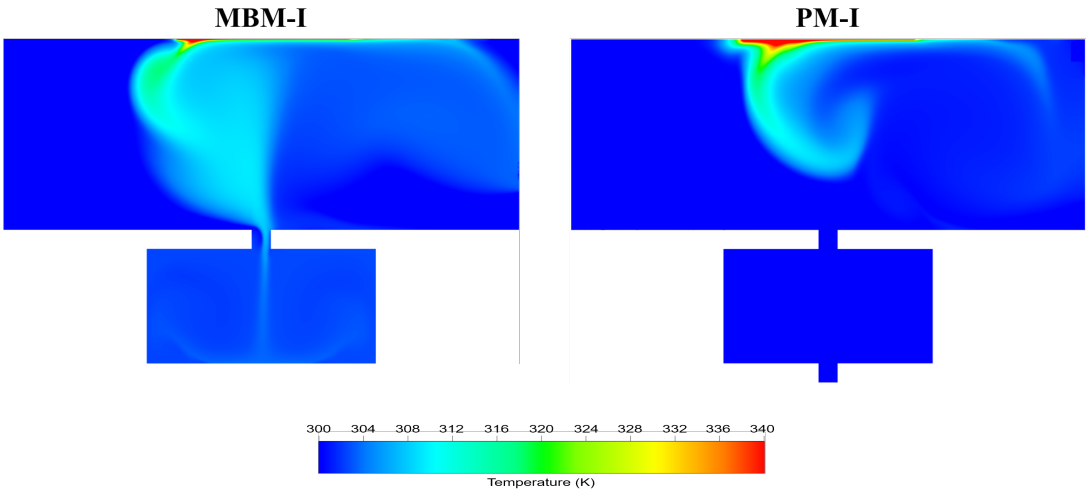

(b) Temperature contours, MBM-I and PM-I

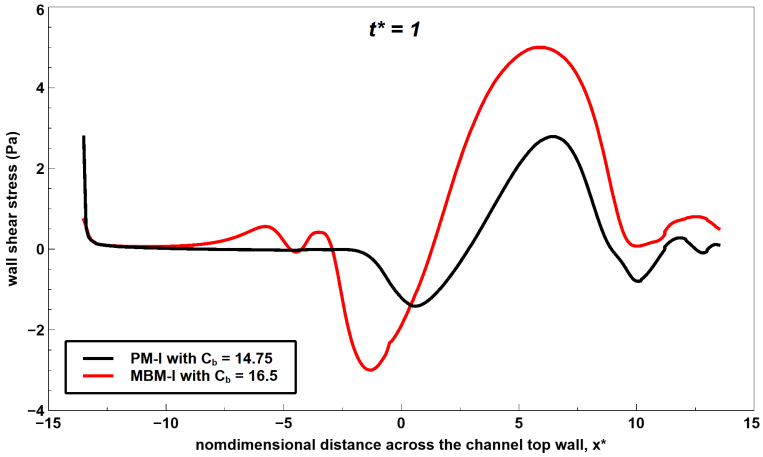

(c) Wall shear stress at the top confined space wall, MBM-I vs PM-I

Figure 3.33: MBM-I with $C_b = 16.5$ vs PM-I with $C_b = 14.75$ at $t^* = 1$

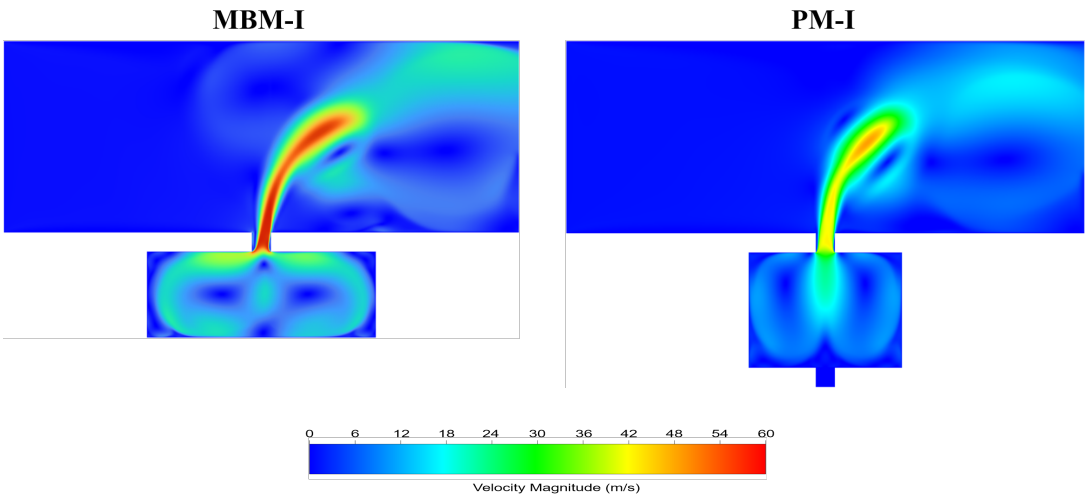

(a) Velocity contours, MBM-I and PM-I

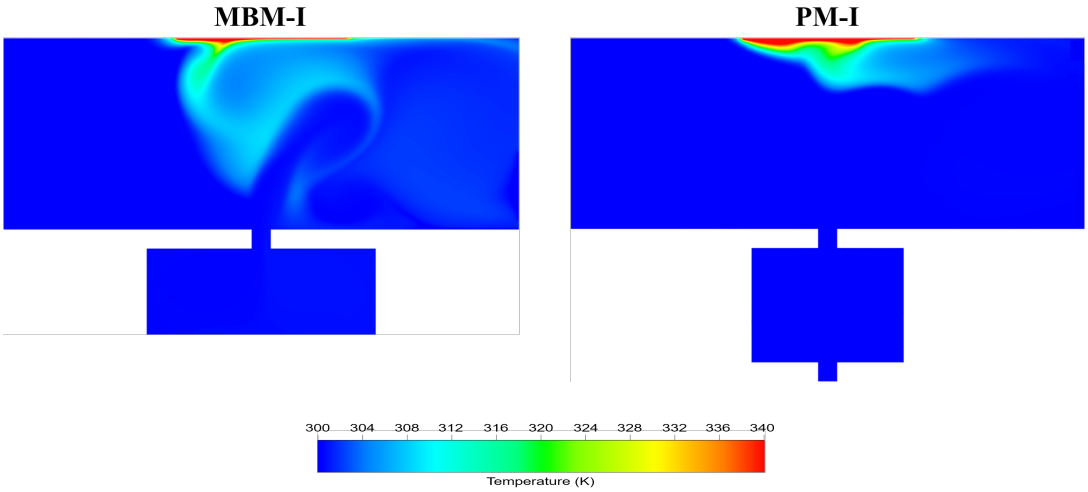

(b) Temperature contours, MBM-I and PM-I

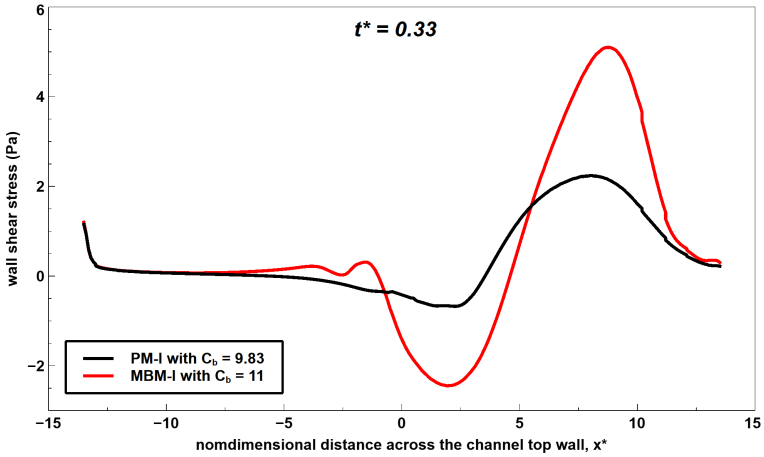

(c) Wall shear stress at the top confined space wall, MBM-I vs PM-I

Figure 3.34: MBM-I with $C_b = 11$ vs PM-I with $C_b = 9.83$ at $t^* = 0.33$

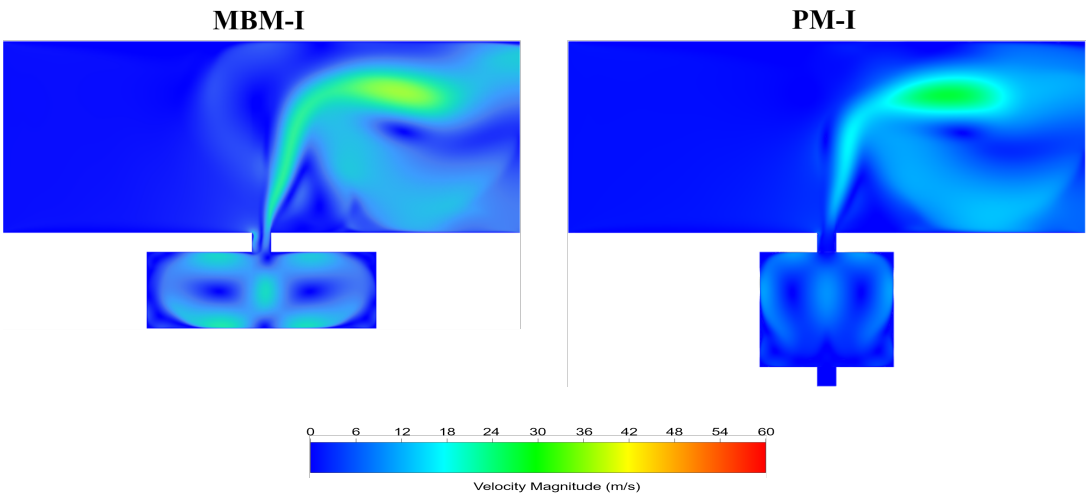

(a) Velocity contours, MBM-I and PM-I

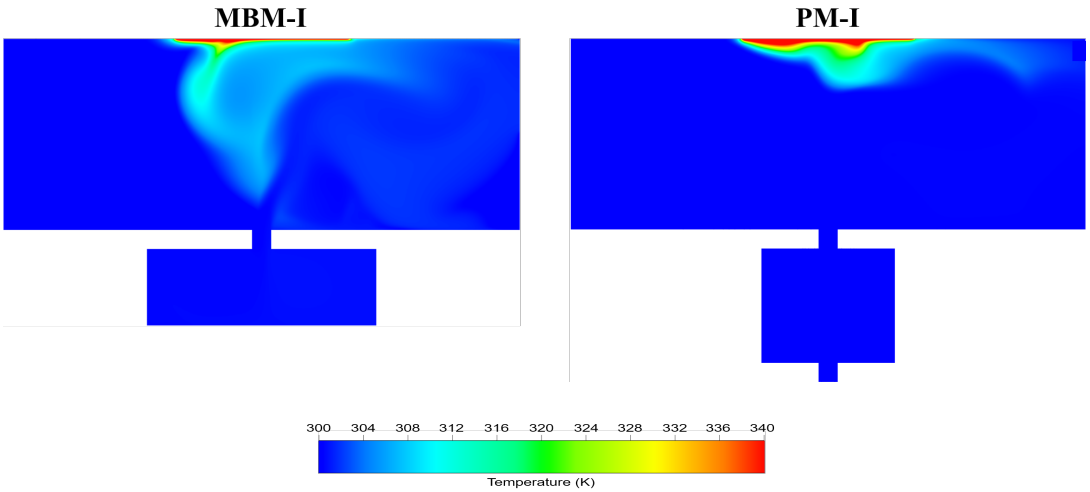

(b) Temperature contours, MBM-I and PM-I

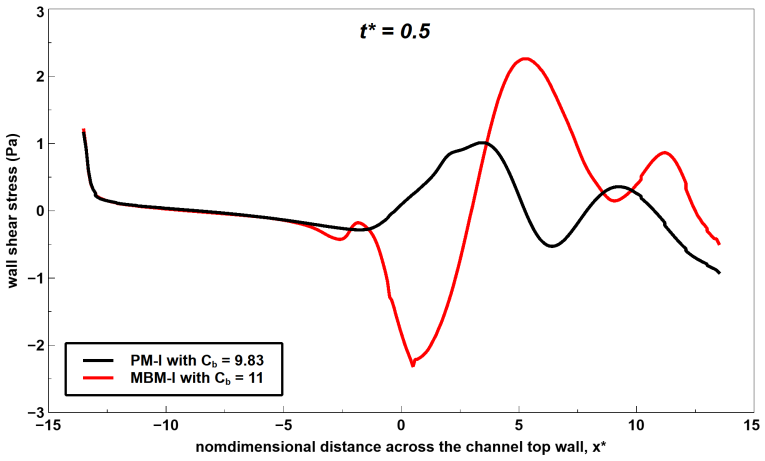

(c) Wall shear stress at the top confined space wall, MBM-I vs PM-I

Figure 3.35: MBM-I with $C_b = 11$ vs PM-I with $C_b = 9.83$ at $t^* = 0.5$

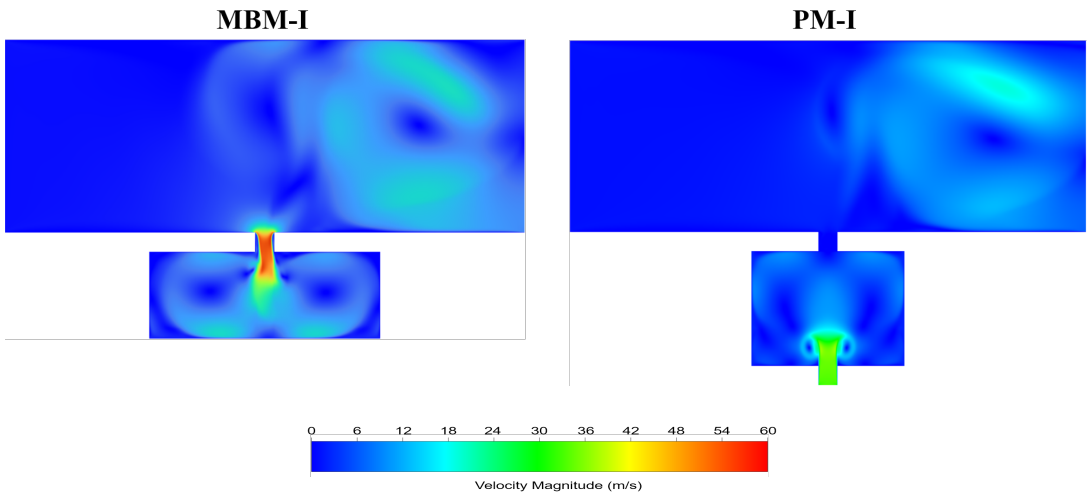

(a) Velocity contours, MBM-I and PM-I

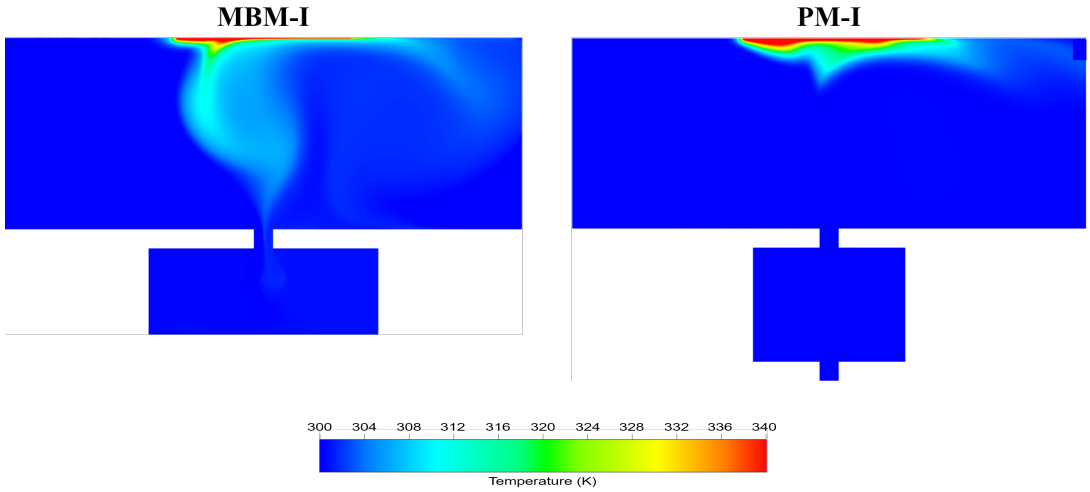

(b) Temperature contours, MBM-I and PM-I

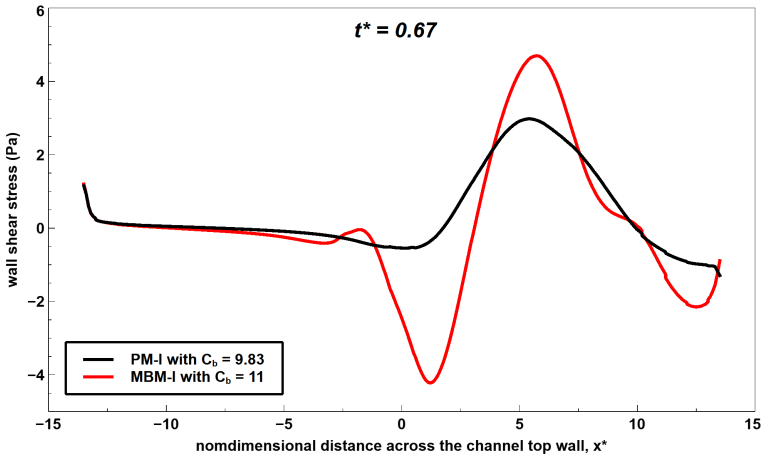

(c) Wall shear stress at the top confined space wall, MBM-I vs PM-I

Figure 3.36: MBM-I with $C_b = 11$ vs PM-I with $C_b = 9.83$ at $t^* = 0.67$

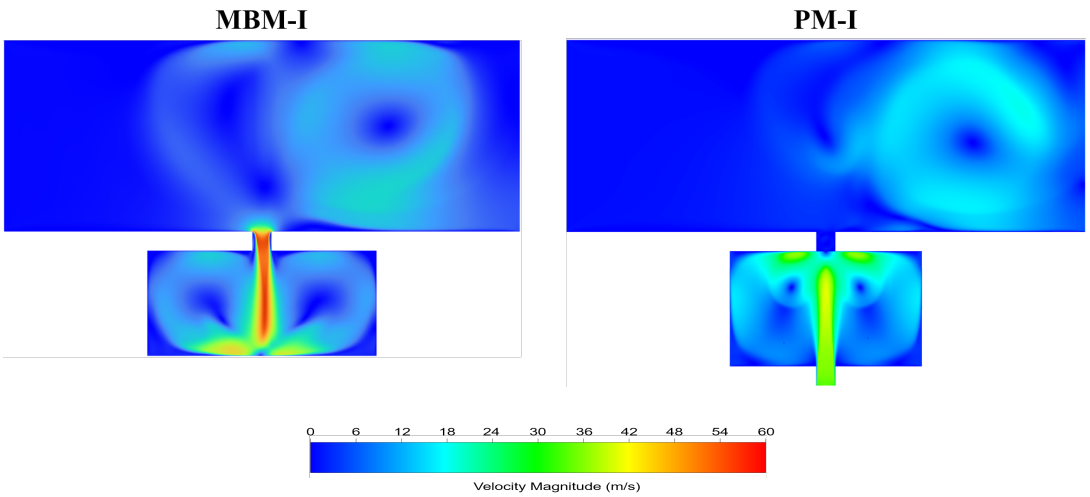

(a) Velocity contours, MBM-I and PM-I

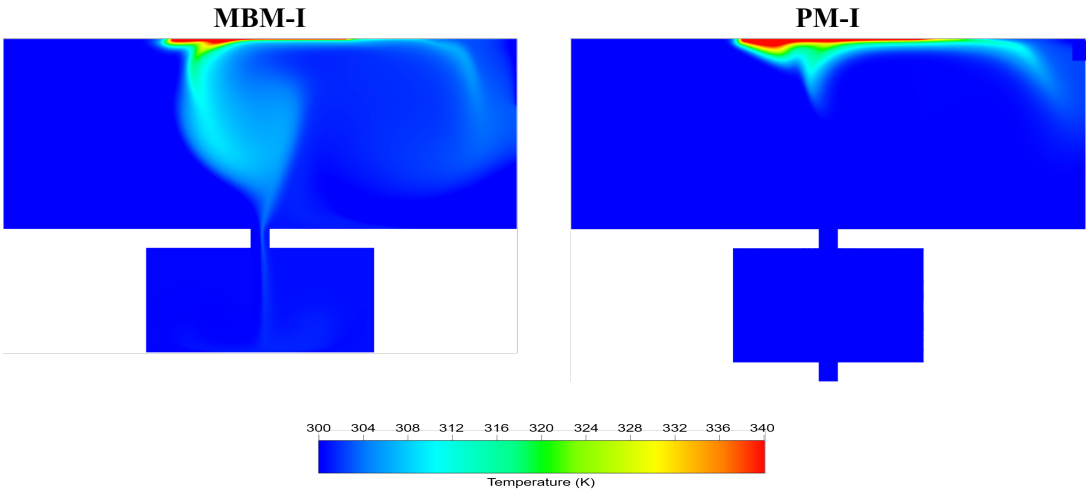

(b) Temperature contours, MBM-I and PM-I

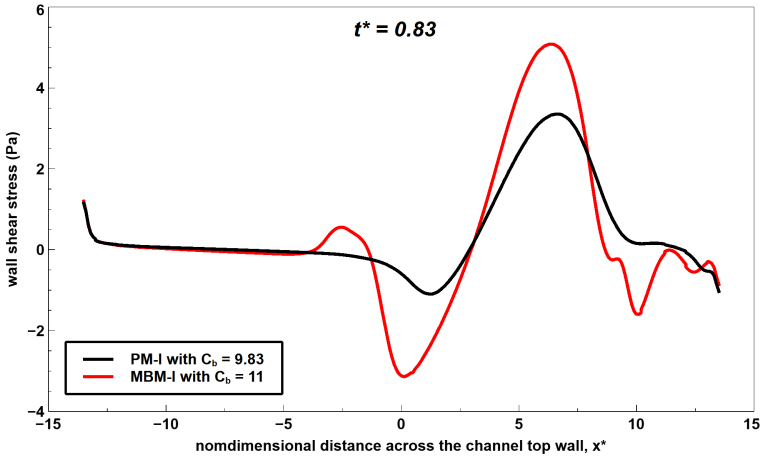

(c) Wall shear stress at the top confined space wall, MBM-I vs PM-I

Figure 3.37: MBM-I with $C_b = 11$ vs PM-I with $C_b = 9.83$ at $t^* = 0.83$

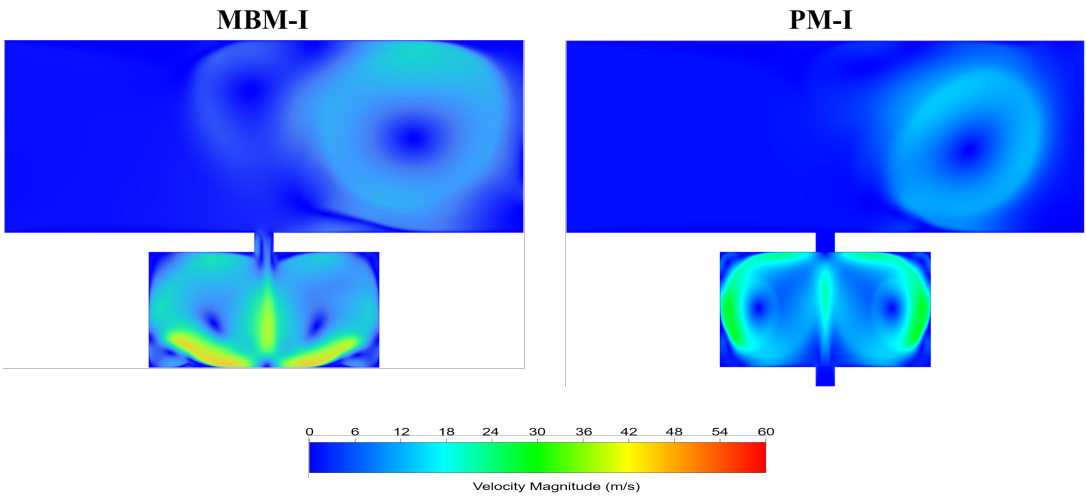

(a) Velocity contours, MBM-I and PM-I

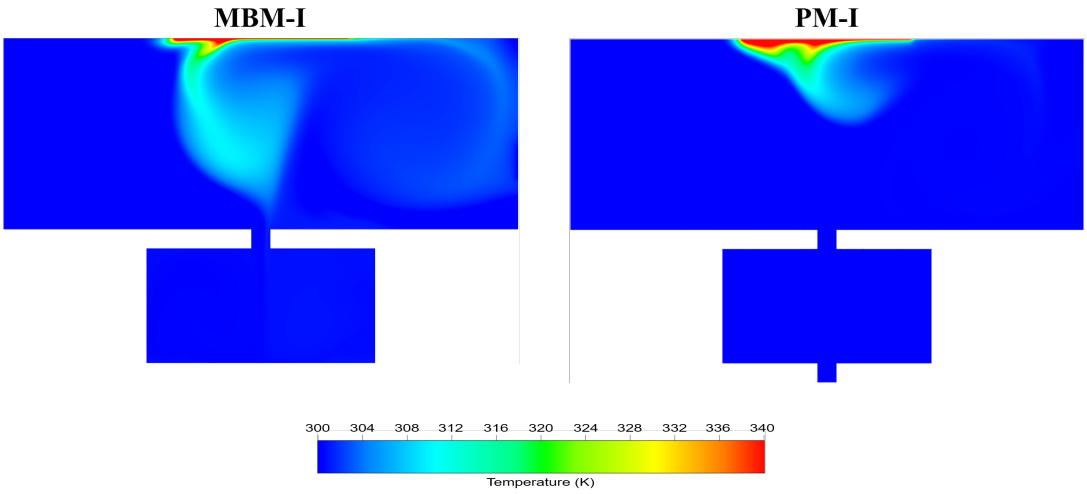

(b) Temperature contours, MBM-I and PM-I

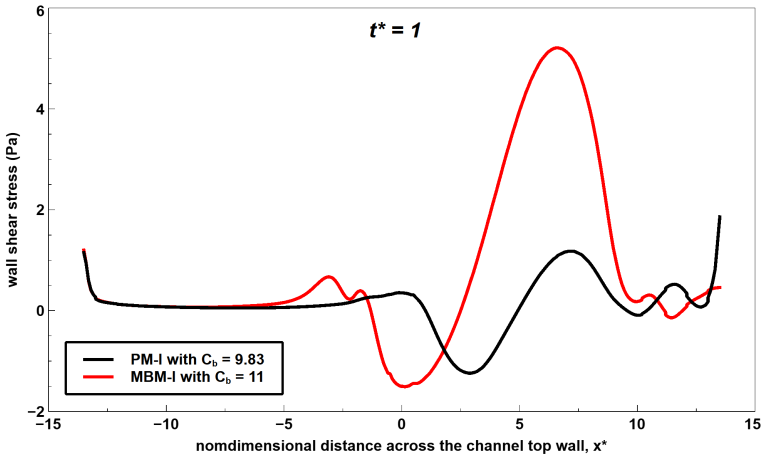

(c) Wall shear stress at the top confined space wall, MBM-I vs PM-I

Figure 3.38: MBM-I with $C_b = 11$ vs PM-I with $C_b = 9.83$ at $t^* = 1$

CHAPTER 4

CONCLUSION

The synthetic jets, zero net mass flux jets, are specific iterations of the continuous jets that produce periodic pulsating flows with several important characteristics, such as strong boundary layer impingement, mixing and hot spot cooling. The applications includes various fields from heat transfer to active flow controllers.

The original name comes from the employment of the same working fluid to the domain of interest. This behavior, inherently, hinders the introduction of the fresh air to the domain; thus, limiting the hydrodynamic and the thermal performance of the SJs. The deficiency is mitigated by the hybrid synthetic jets, which modifies the orifice geometry in order to utilize the surrounding fluid into the working domain. Even though, the literature discusses a reciprocating-liked configuration which could reach 100% fresh air usage, the application of hybrid synthetic jets are limited to basic heat sink designs. For example, they cannot be used in multi-layered heat sinks since they do not allow fluid to pass between two sources unlike the proposed design.

The proposed design consists of an extra orifice that could be used as a passage in the multi layer interconnected microchannel heat exchangers. The direction of the flow in the orifices are controlled via check valves ensuring unidirectional momentum transfer that results in less required work and higher efficiency. The required work input by the moving wall is decreased by 26% and enhancements on the peak heat transfer are achieved as high as 15%. However, the total heat transfer per unit length is observed to decrease about 2%. The decrease in the overall heat transfer could be caused by the absence of the far field modeling at the adjacent zone of the bottom orifice's exit. Further experiments and numerical investigations are required for better understanding of the decrease in the heat transfer.

In the presence of the cross flow, PM-I rapidly loses its advantage over MBM-I, as the magnitude of the cross flow increases. Nevertheless, the proposed model may offer enhancement on the mixing in the multi layer interconnected microchannels. The effect of the proposed model on the multi layer interconnected microchannels is left out as a future work.

REFERENCES

[1] T. T. Chandratilleke, D. Jagannatha, and R. Narayanaswamy, "Performance analysis of a synthetic jet-microchannel hybrid heat sink for electronic cooling," in *2009 11th Electronics Packaging Technology Conference*, pp. 630–635, 2009.

[2] S. Wang, D. Zhou, and Z. Yang, "Design of a cooling system for microchips with high heat-flux density using integrated microchannels," *Heat Transfer Research*, vol. 48, no. 14, pp. 1299–1312, 2017. Funding Information: The work described in this paper is supported by the Importation and Development of High-Caliber Talents Project of the Beijing Municipal Institutions and the Beijing Intelligent Machinery Innovation Design Service Engineering Technology Research Center. Publisher Copyright: © 2017 by Begell House, Inc.

[3] A. Bar-Cohen, M. Arik, and M. Ohadi, "Direct liquid cooling of high flux micro and nano electronic components," *Proceedings of the IEEE*, vol. 94, no. 8, pp. 1549–1570, 2006.

[4] D. Lytle and B. Webb, "Air jet impingement heat transfer at low nozzle-plate spacings," *International Journal of Heat and Mass Transfer*, vol. 37, no. 12, pp. 1687–1697, 1994.

[5] N. Zuckerman and N. Lior, "Jet impingement heat transfer: physics, correlations, and numerical modeling," *Advances in heat transfer*, vol. 39, pp. 565–631, 2006.

[6] K. Jambunathan, E. Lai, M. Moss, and B. Button, "A review of heat transfer data for single circular jet impingement," *International journal of heat and fluid flow*, vol. 13, no. 2, pp. 106–115, 1992.

[7] R. Viskanta, "Heat transfer to impinging isothermal gas and flame jets," *Experimental Thermal and Fluid Science*, vol. 6, no. 2, pp. 111–134, 1993.

[8] J.-Y. San and J.-J. Chen, "Effects of jet-to-jet spacing and jet height on heat transfer characteristics of an impinging jet array," *International journal of heat and mass transfer*, vol. 71, pp. 8–17, 2014.

[9] R. Goldstein and A. Behbahani, "Impingement of a circular jet with and without cross flow," *International Journal of Heat and Mass Transfer*, vol. 25, no. 9, pp. 1377–1382, 1982.

[10] E. M. Sparrow, R. Goldstein, and M. Rouf, "Effect of nozzle—surface separation distance on impingement heat transfer for a jet in a crossflow," 1975.

[11] D. Colucci and R. Viskanta, "Effect of nozzle geometry on local convective heat transfer to a confined impinging air jet," *Experimental Thermal and Fluid Science*, vol. 13, no. 1, pp. 71–80, 1996.

[12] L. A. Brignoni and S. V. Garimella, "Effects of nozzle-inlet chamfering on pressure drop and heat transfer in confined air jet impingement," *International Journal of Heat and Mass Transfer*, vol. 43, no. 7, pp. 1133–1139, 2000.

[13] S. V. Garimella and B. Nenaydykh, "Nozzle-geometry effects in liquid jet impingement heat transfer," *International Journal of Heat and Mass Transfer*, vol. 39, no. 14, pp. 2915–2923, 1996.

[14] B. L. Smith and G. Swift, "A comparison between synthetic jets and continuous jets," *Experiments in fluids*, vol. 34, no. 4, pp. 467–472, 2003.

[15] J. E. Cater and J. Soria, "The evolution of round zero-net-mass-flux jets," *Journal of Fluid Mechanics*, vol. 472, pp. 167–200, 2002.

[16] C. S. Greco, G. Cardone, and J. Soria, "On the behaviour of impinging zero-net-mass-flux jets," *Journal of fluid mechanics*, vol. 810, pp. 25–59, 2017.

[17] R. N. Sharma, "Fluid dynamics-based analytical model for synthetic jet actuation," *AIAA Journal*, vol. 45, no. 8, pp. 1841–1847, 2007.

[18] B. L. Smith and A. Glezer, "The formation and evolution of synthetic jets," *Physics of fluids*, vol. 10, no. 9, pp. 2281–2297, 1998.

[19] M. Schwickert, "Synjet thermal management technology increases led lighting system reliability," *IEEE Reliability Society Annual Technical Report 2009*, 2009.

[20] A. Glezer, "Some aspects of aerodynamic flow control using synthetic-jet actuation," *Philosophical Transactions of the Royal Society A: Mathematical, Physical and Engineering Sciences*, vol. 369, no. 1940, pp. 1476–1494, 2011.

[21] D. N. Grimm, "Advanced synjet cooler design for led light modules," Oct. 30 2012. US Patent 8,299,691.

[22] M. Krieg and K. Mohseni, "Thrust characterization of a bioinspired vortex ring thruster for locomotion of underwater robots," *IEEE Journal of Oceanic Engineering*, vol. 33, no. 2, pp. 123–132, 2008.

[23] J. M. Shuster and D. R. Smith, "Experimental study of the formation and scaling of a round synthetic jet," *Physics of fluids*, vol. 19, no. 4, p. 045109, 2007.

[24] A. Glezer, "The formation of vortex rings," *The Physics of fluids*, vol. 31, no. 12, pp. 3532–3542, 1988.

[25] L. Silva-Llanca, A. Ortega, and I. Rose, "Experimental convective heat transfer in a geometrically large two-dimensional impinging synthetic jet," *International Journal of Thermal Sciences*, vol. 90, pp. 339–350, 2015.

[26] M. Gillespie, W. Black, C. Rinehart, and A. Glezer, "Local convective heat transfer from a constant heat flux flat plate cooled by synthetic air jets," 2006.

[27] M. Jain, B. Puranik, and A. Agrawal, "A numerical investigation of effects of cavity and orifice parameters on the characteristics of a synthetic jet flow," *Sensors and actuators A: Physical*, vol. 165, no. 2, pp. 351–366, 2011.

[28] M. A. Feero, P. Lavoie, and P. E. Sullivan, "Influence of cavity shape on synthetic jet performance," *Sensors and Actuators A: Physical*, vol. 223, pp. 1–10, 2015.

[29] D. S. Kercher, J.-B. Lee, O. Brand, M. G. Allen, and A. Glezer, "Microjet cooling devices for thermal management of electronics," *IEEE Transactions on Components and Packaging Technologies*, vol. 26, no. 2, pp. 359–366, 2003.

[30] C. S. Greco, A. Ianiro, and G. Cardone, "Time and phase average heat transfer in single and twin circular synthetic impinging air jets," *International Journal of Heat and Mass Transfer*, vol. 73, pp. 776–788, 2014.

[31] C. S. Greco, G. Paolillo, A. Ianiro, G. Cardone, and L. De Luca, "Effects of the stroke length and nozzle-to-plate distance on synthetic jet impingement heat transfer," *International Journal of Heat and Mass Transfer*, vol. 117, pp. 1019–1031, 2018.

[32] B. Smith and G. Swift, "Synthetic jets at large reynolds number and comparison to continuous jets," in *15th AIAA computational fluid dynamics conference*, p. 3030, 2001.

[33] R. Mittal, P. Rampunggoon, and H. Udaykumar, "Interaction of a synthetic jet with a flat plate boundary layer," in *15th AIAA computational fluid dynamics conference*, p. 2773, 2001.

[34] R. Holman, Y. Utturkar, R. Mittal, B. L. Smith, and L. Cattafesta, "Formation criterion for synthetic jets," *AIAA journal*, vol. 43, no. 10, pp. 2110–2116, 2005.

[35] M. Arik, R. Sharma, J. Lustbader, and X. He, "Steady and unsteady air impingement heat transfer for electronics cooling applications," *Journal of heat transfer*, vol. 135, no. 11, 2013.

[36] X. He, J. A. Lustbader, M. Arik, and R. Sharma, "Heat transfer characteristics of impinging steady and synthetic jets over vertical flat surface," *International Journal of Heat and Mass Transfer*, vol. 80, pp. 825–834, 2015.

[37] U. S. Bhapkar, A. Srivastava, and A. Agrawal, "Proper cavity shape can mitigate confinement effect in synthetic jet impingement cooling," *Experimental Thermal and Fluid Science*, vol. 68, pp. 392–401, 2015.

[38] F. R. Munas, G. Melroy, C. B. Abeynayake, H. L. Chathuranga, R. Amarasinghe, P. Kumarage, V. T. Dau, and D. V. Dao, "Development of pzt actuated valveless micropump," *Sensors*, vol. 18, no. 5, p. 1302, 2018.

[39] G.-H. Feng and E. S. Kim, "Micropump based on pzt unimorph and one-way parylene valves," *Journal of micromechanics and microengineering*, vol. 14, no. 4, p. 429, 2004.

[40] L. He, X. Wu, D. Zhao, W. Li, G. Cheng, and S. Chen, "Exploration on relationship between flow rate and sound pressure level of piezoelectric pump," *Microsystem Technologies*, vol. 26, no. 2, pp. 609–616, 2020.

[41] M. Carrozza, N. Croce, B. Magnani, and P. Dario, "A piezoelectric-driven stereolithography-fabricated micropump," *Journal of Micromechanics and Microengineering*, vol. 5, no. 2, p. 177, 1995.

[42] D. Accoto, M. Carrozza, and P. Dario, "Modelling of micropumps using unimorph piezoelectric actuator and ball valves," *Journal of Micromechanics and Microengineering*, vol. 10, no. 2, p. 277, 2000.

[43] M. Koch, N. Harris, A. G. Evans, N. M. White, and A. Brunnschweiler, "A novel micromachined pump based on thick-film piezoelectric actuation," *Sensors and Actuators A: Physical*, vol. 70, no. 1-2, pp. 98–103, 1998.

[44] N.-T. Nguyen and T.-Q. Truong, "A fully polymeric micropump with piezoelectric actuator," *Sensors and Actuators B: Chemical*, vol. 97, no. 1, pp. 137–143, 2004.

[45] T.-Q. Truong and N.-T. Nguyen, "A polymeric piezoelectric micropump based on lamination technology," *Journal of Micromechanics and Microengineering*, vol. 14, no. 4, p. 632, 2004.

[46] P. Zeng, L. Li, J. Dong, G. Cheng, J. Kan, and F. Xu, "Structure design and experimental study on single-bimorph double-acting check-valve piezoelectric pump," *Proceedings of the Institution of Mechanical Engineers, Part C: Journal of Mechanical Engineering Science*, vol. 230, no. 14, pp. 2339–2344, 2016.

[47] Y. Luo, M. Lu, and T. Cui, "A polymer-based bidirectional micropump driven by a pzt bimorph," Jan 2011.

[48] H. Li, J. Liu, K. Li, and Y. Liu, "A review of recent studies on piezoelectric pumps and their applications," *Mechanical Systems and Signal Processing*, vol. 151, p. 107393, 2021.

[49] D. G. Lee, S. W. Or, and G. P. Carman, "Design of a piezoelectric-hydraulic pump with active valves," *Journal of intelligent material systems and structures*, vol. 15, no. 2, pp. 107–115, 2004.

[50] T. Lemke, G. Biancuzzi, C. Farhat, B. Vodermayer, O. Ruthmann, T. Schmid, H.-J. Schrag, P. Woias, and F. Goldschmidtboeing, "A high performance bidirectional micropump utilizing advanced low voltage piezo multilayer actuator technology for a novel artificial sphincter system," in *4th European Conference of the International Federation for Medical and Biological Engineering*, pp. 1517–1520, Springer, 2009.

[51] Z. Broučková and Z. Trávníček, "Visualization study of hybrid synthetic jets," *Journal of Visualization*, vol. 18, no. 4, pp. 581–593, 2015.

[52] Z. Trávníček, T. Vít, and V. Tesař, "Hybrid synthetic jets as the nonzero-net-mass-flux synthetic jets," *Physics of Fluids*, vol. 18, no. 8, p. 081701, 2006.

[53] S.-S. Hsu, Z. Travnicek, C.-C. Chou, C.-C. Chen, and A.-B. Wang, "Comparison of double-acting and single-acting synthetic jets," *Sensors and Actuators A: Physical*, vol. 203, pp. 291–299, 2013.

[54] J. Kordík and Z. Trávníček, "Novel fluidic diode for hybrid synthetic jet actuator," *Journal of fluids engineering*, vol. 135, no. 10, 2013.

[55] Z. Trávníček and T. Vít, "Impingement heat/mass transfer to hybrid synthetic jets and other reversible pulsating jets," *International Journal of Heat and Mass Transfer*, vol. 85, pp. 473–487, 2015.

[56] S.-S. Hsu, Y.-J. Chou, Z. Trávníček, C.-F. Lin, A.-B. Wang, and R.-H. Yen, "Numerical study of nozzle design for the hybrid synthetic jet actuator," *Sensors and Actuators A: Physical*, vol. 232, pp. 172–182, 2015.

[57] Q. Yu, Z. Mei, M. Bai, D. Xie, Y. Ding, and Y. Li, "Cooling performance improvement of impingement hybrid synthetic jets in a confined space with the aid of a fluid diode," *Applied Thermal Engineering*, vol. 157, p. 113749, 2019.

[58] D. Jagannatha, R. Narayanaswamy, and T. T. Chandratilleke, "Analysis of a synthetic jet-based electronic cooling module," *Numerical Heat Transfer, Part A: Applications*, vol. 56, no. 3, pp. 211–229, 2009.

[59] R. B. Kotapati, R. Mittal, and L. N. Cattafesta Iii, "Numerical study of a transitional synthetic jet in quiescent external flow," *Journal of Fluid mechanics*, vol. 581, pp. 287–321, 2007.

[60] S. A. Khan, M. Bashir, M. A. A. Baig, and F. A. G. M. Ali, "Comparing the effect of different turbulence models on the cfd predictions of naca0018 airfoil aerodynamics," *CFD Letters*, vol. 12, no. 3, pp. 1–10, 2020.

[61] F. R. Menter, R. B. Langtry, S. Likki, Y. Suzen, P. Huang, and S. Völker, "A correlation-based transition model using local variables—part i: model formulation," 2006.

[62] F. R. Menter, "Two-equation eddy-viscosity turbulence models for engineering applications," *AIAA journal*, vol. 32, no. 8, pp. 1598–1605, 1994.

[63] R. B. Langtry and F. R. Menter, "Correlation-based transition modeling for unstructured parallelized computational fluid dynamics codes," *AIAA journal*, vol. 47, no. 12, pp. 2894–2906, 2009.

APPENDIX A

USER DEFINED FUNCTION

```
#include"udf.h"
DEFINE_CG_MOTION(besyuz,dt,vel,omega,time,dtime)
{
Thread*t;
face_t*f;
/*reset velocities */
NV_S(vel,=,0.0);
NV_S(omega,=,0.0);
if(!Data_Valid_P())
return;
t=DT_THREAD(dt);
/*assign velocity in the y direction */
vel[1] = 1e-3*3141.59*cos(3141.59*time-3.14159265359/2);
}
```

APPENDIX B

SCHEME FILE

```
(define (chabbcsss)
(define flag 0)
(define bctype 0)
(define time (rpgetvar 'flow-time))
(define dt (rpgetvar 'physical-time-step))
(define prtime (* 5 dt))
(define prevtime (- time prtime))
(define con 0.0000590989)
(set! flag 0)
(define mult (* prevtime 3141.5))
(define subs (- mult 1.570796))
(define cosi (cos subs))
(if (>= cosi con)
(set! flag 1) )
(if (< cosi con)
(set! flag 2) )
(if (= flag 1)
(ti-menu-load-string "define/boundary-conditions/zone-type 9 wall"))
(if (= flag 1)
(ti-menu-load-string "define/boundary-conditions/zone-type 10 interior"))
(if (= flag 2)
(ti-menu-load-string "define/boundary-conditions/zone-type 10 wall"))
(if (= flag 2)
(ti-menu-load-string "define/boundary-conditions/zone-type 9 interior")))
```

APPENDIX C

FLOW CHARACTERISTIC FOR PM-I

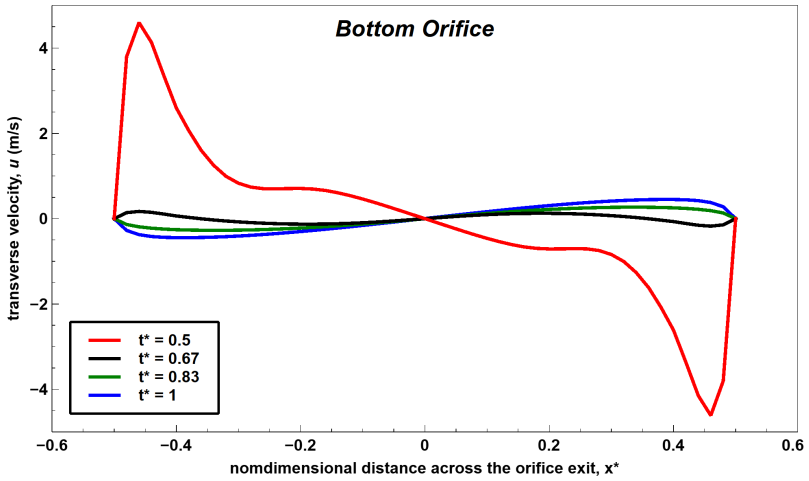

(a) Transverse velocity for bottom orifice

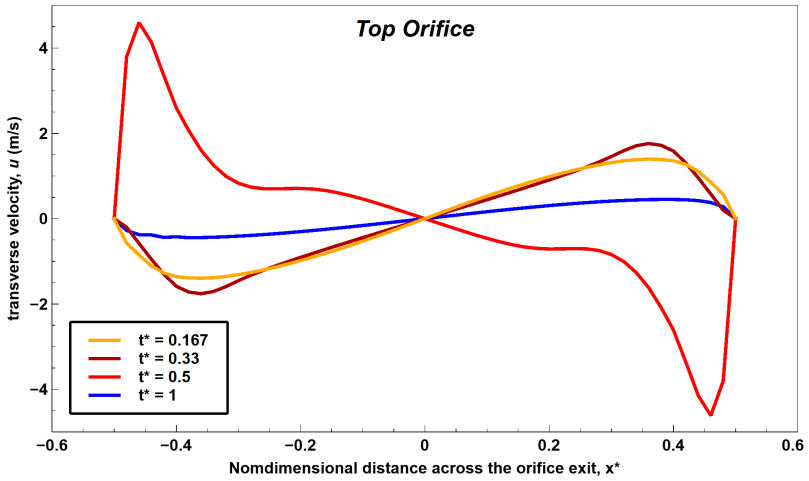

(b) Transverse velocity for top orifice

Figure C.1: Transverse velocities for various nondimensional times of PM-I

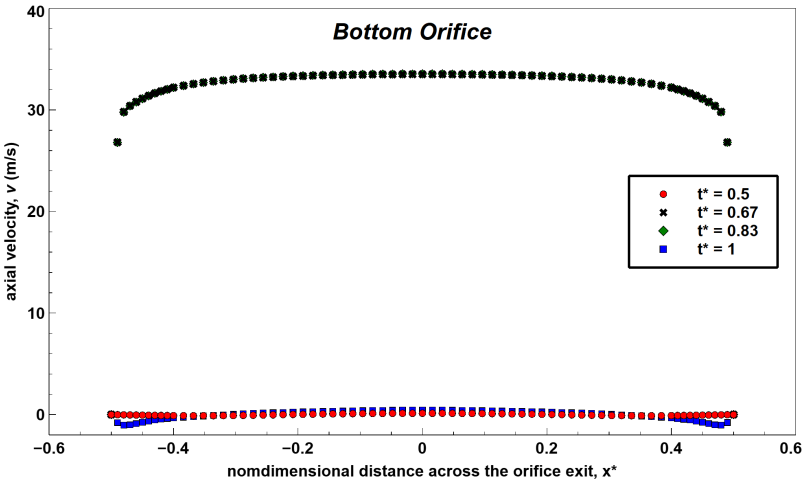

(a) Axial velocity profile at the bottom orifice

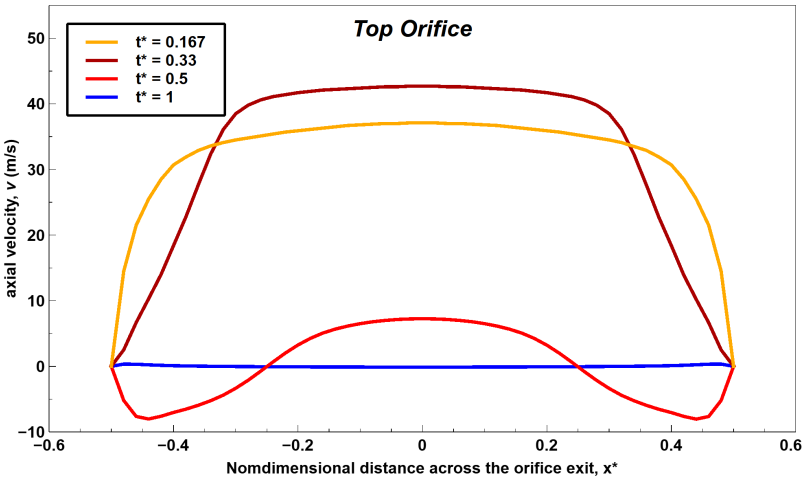

(b) Axial velocity profile at the top orifice

Figure C.2: Axial velocities for various nondimensional times of PM-I

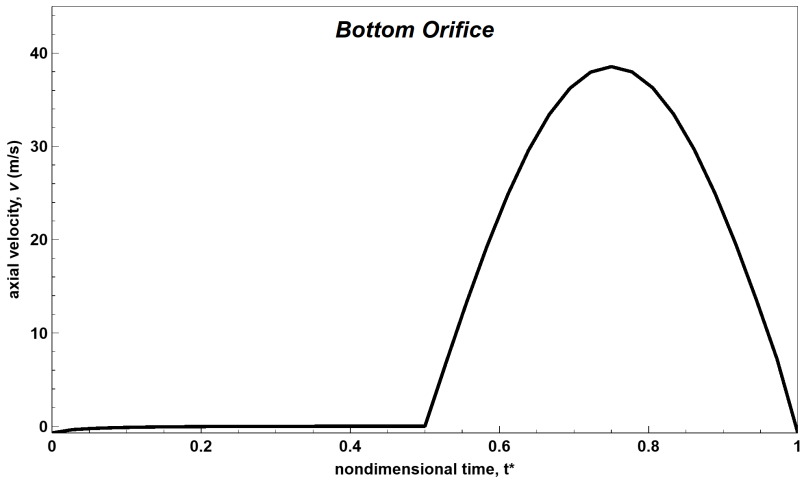

(a) Bottom orifice

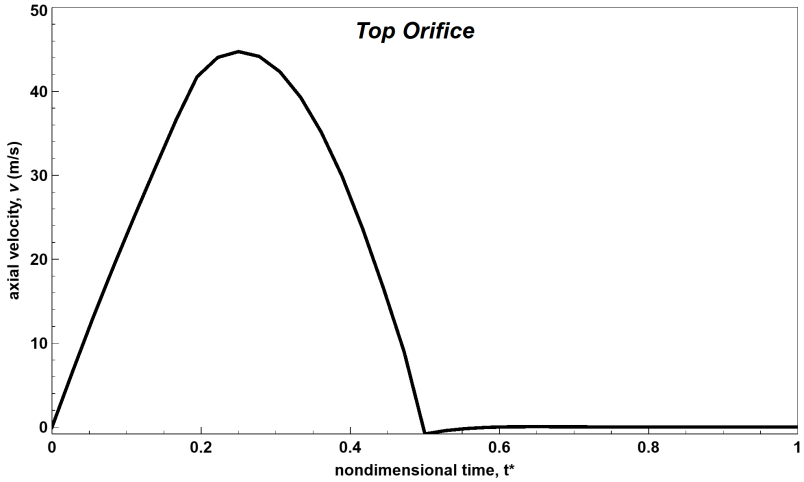

(b) Top orifice

Figure C.3: Mass weighted average axial velocity in the orifice domain of PM-I